General Purpose PDF Solution Algorithm for Reactive Flow Simulations in OpenFOAM

Michael Andreas Wild

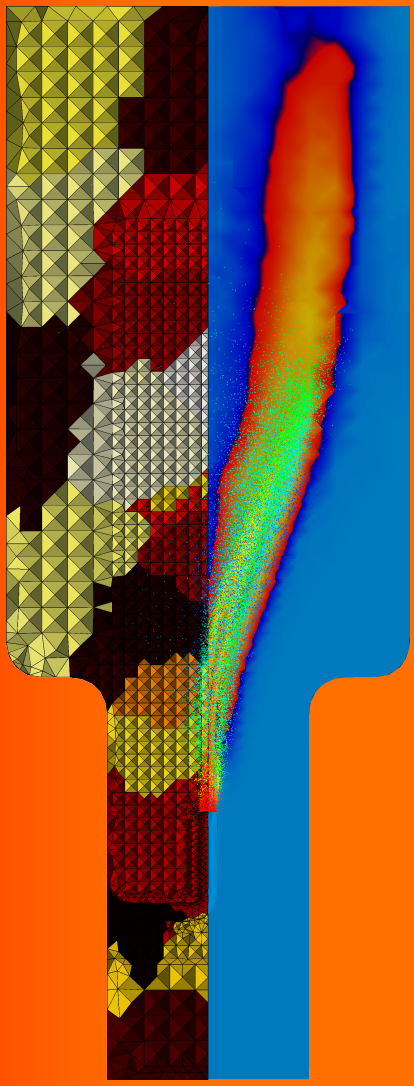

Dissertation
ETH No. 20915

Visualisation of an auto-ignition flame simulation in complex 3D geometry. The left-hand side presents a cross-section through the computational mesh, where the colours indicate the processor domains of the parallel decomposition. On the right-hand side the flame is visualised, where the transition from cold (blue) to hot (red to yellow) colours is at 1400 K. The dots represent computational particles that have been injected through the fuel nozzle, where the colour is indicates the mixture fraction.

A digital version of this thesis can be downloaded from the ETH e-collection:
http://dx.doi.org/10.3929/ethz-a-009775134

This thesis was typeset using XeLaTeX.

DISS. ETH NO. 20915

General Purpose PDF Solution Algorithm for Reactive Flow Simulations in OpenFOAM

A dissertation submitted to

ETH ZÜRICH

for the degree of

Doctor of Sciences

presented by
MICHAEL ANDREAS WILD

Dipl. Masch.-Ing. ETH

born on December 17, 1979

citizen of Klingnau AG (Switzerland)

accepted on the recommendation of

Prof. Dr. Patrick Jenny
Prof. Dr. Ulrich Maas

2013

Abstract

Turbulent combustion is at the heart of many of today's primary energy conversion technologies – be it internal combustion engines for cars, trucks or large container ships, turbines for aeroplanes or the production of electricity, heating devices or industrial furnaces. Today, it is more important than ever to improve the efficiency and reduce the production of pollutants. For this, accurate and computationally efficient simulation tools are indispensable.

For configurations that are relevant for practical applications, direct numerical simulation (DNS) is computationally not tractable. Traditional Reynolds averaged or large eddy simulation methodologies, however, pose significant modelling challenges, especially for the unclosed mean or filtered turbulence transport and chemical source terms. Methods based on the transport equation for the joint probability function (JPDF) offer a significant advantage: here, these terms appear in closed form. Conventional Eulerian methods, such as finite volume, finite element or finite difference methods being unsuitable due to the high dimensionality of the JPDF transport equation, stochastic Monte-Carlo methods are commonly used.

In this work, a hybrid solution algorithm for steady state turbulent reactive flows is presented that attempts to combine the advantages of both, Reynolds averaged simulation and transported JPDF methods. The Reynolds averaged equations are solved using a conventional finite volume method, while the JPDF transport equation is solved using a transported Monte-Carlo particle method. In the first part of this work, the theoretical foundations are presented. The second part describes the hybrid algorithm and its implementation in the context of a powerful open-source simulation code. In the third and last part of this work, validation results for increasingly complex problems are presented: A simple non-reacting round jet in co-flow; a piloted methane-air jet flame, a non-reacting bluff-body flow with recirculation, and finally a bluff-body stabilised methane-hydrogen-air flame. For the latter, grid and bias convergence studies are presented. Internal consistency is shown and despite using the simplest possible models for the chemical source terms and the molecular mixing, good agreement with the experimental data is achieved for all of the validation cases. The applicability to complex geometries without quantitative comparison is demonstrated with an auto-ignition stabilised burner, similar to what is used in sequential combustion configurations.

Zusammenfassung

Seien es Verbrennungsmotoren für Autos, Lastwagen oder grosse Container-Schiffe, Turbinen für Flugzeuge oder zur Stromgewinnung, Heizungen oder Industrieöfen – turbulente Verbrennung ist zentral für viele Technologien der Energie-Umwandlung. Heute ist es wichtiger denn je, den Wirkungsgrad dieser Prozesse zu verbessern und die Emissionen zu reduzieren. Um dies zu erreichen sind effiziente und genaue Simulations-Werkzeuge unabdingbar.

Für praktisch relevante Konfigurationen ist die direkte numerische Simulation (DNS) aufgrund der riesigen Spanne von zeitlichen und räumlichen Skalen nicht anwendbar. Herkömmliche Reynolds-Mittelungs und Large-Eddy Simulationen stellen aber grosse Herausforderungen an die Modellierung, insbesondere für die ungeschlossenen mittleren oder gefilterten Terme für den turbulenten Transport und die chemischen Quellterme. Methoden, die den Transport der Verbund-Wahrscheinlichkeitsdichtefunktion (JPDF) simulieren, haben einen grossen Vorteil, da diese Terme hier in geschlossener Form vorliegen. Konventionelle Eulersche Verfahren, wie finite Volumen, finite Elemente oder finite Differenzen Methoden sind aufgrund der grossen Anzahl Dimensionen in der sich die JPDF entwickelt, nicht geeignet. Stattdessen werden oft stochastische Monte-Carlo Verfahren eingesetzt.

In dieser Arbeit wird ein hybrider Algorithmus zur Simulation stationärer, turbulenter reaktiver Strömungen vorgestellt, der die Vorteile von Reynolds-gemittelter Simulation und transportierten JPDF Methoden kombinieren soll. Die Reynolds-gemittelten Gleichungen werden mittels einem herkömmlichen finite Volumen Verfahren gelöst, und für die Lösung der JPDF Transportgleichung wird ein Lagranges Monte-Carlo Partikel Verfahren eingesetzt. Im ersten Teil der Arbeit werden die theoretischen Grundlagen erarbeitet. Der zweite Teil beschreibt den Algorithmus und dessen Umsetzung in einer leistungsfähigen open-source Simulations-Plattform. Im dritten und letzten Teil dieser Arbeit werden Validierungs-Resultate für zunehmend komplexe Probleme präsentiert: ein inerter, runder Freistrahl in langsamer Umgebungsströmung, eine pilotierte Methan-Luft Freistrahl-Flamme, eine nicht-reaktive Umströmung eines stumpfen Körpers mit Rezirkulationszone, und eine Methan-Wasserstoff-Luft Flamme, die durch einen stumpfen Körper stabilisiert wird. Hier werden auch Konvergenz-Studien zur Gitterauflösung und zum systematischen Fehler präsentiert. Die interne Konsistenz des Algorithmus wird gezeigt, und obwohl nur einfachste physikalische Modelle verwendet werden, stimmen die Simulationen mit den verfügbaren experimentellen Daten für alle der gezeigten Validierungsfälle gut überein. Die Anwendbarkeit für komplexe Geometrien, allerdings ohne quantitativen Vergleich, wird schlussendlich anhand eines durch Selbstzündung stabilisierten Brenners demonstriert.

Acknowledgements

My gratitude goes to Prof Dr Patrick Jenny for providing me with the opportunity to pursue my doctoral studies under his supervision at the Institute of Fluid Dynamics. His guidance and our very constructive discussions were fundamental for me to successfully complete this very challenging and multifaceted project. To Prof Dr Ulrich Maas I would like to extend many thanks for agreeing to being my co-examiner and for reviewing my thesis on an impossibly tight time schedule. Many of my fellow students at ETH Zürich, too numerous to name them all, became dear friends to me. Without their support and friendship it would have been impossible for me to make it through the tough parts of the project that every doctoral student knows all too well. I am particularly indebted to Dr Heng Xiao, Dr Daniel Meyer and Benjamin Zoller for their invaluable support and many fruitful discussions, both on scientific and personal topics. Special thanks belong to the administrative staff at the institute, namely Bianca Maspero, Sonia Atkinson and Hans Peter Caprez, for providing and maintaining a great working environment and for guiding me through the many administrative hurdles.

My brother is deserving of an award for being such a great reviewer and relentless critic of this work, sacrificing many hours of his precious time to provide invaluable feedback.

Above all, however, my eternal gratitude goes to my wife, Barbara. It was her unconditional love and reassurance that provided me with the security I required to keep me going. My son Max takes a special place in my heart – with his endearing, cheerful personality he is my personal fountain of joy.

This work was financially supported by ETH Zürich.

Bern, April 2013 Michael Andreas Wild

Contents

List of Figures

List of Tables

Nomenclature

In this work it is attempted to employ a consistent notation throughout the text. Vectors are typeset in bold, oblique script (e.g. $\boldsymbol{u}$) and tensors are generally typeset as bold and upright (e.g. $\mathbf{A}$). In displayed equations index notation is used everywhere; the vector $\boldsymbol{u}$ will be represented by u_i and the tensor $\mathbf{A}$ by A_{ij} where the indices run over their full range. For roman script indices (i, j, k etc.) the Einstein summation convention is employed – if an index appears two or more times in a single *term*, summation over its full range is implied. As an example, the scalar (inner) product of vectors $\boldsymbol{u}$ and $\boldsymbol{v}$ would be denoted as $u_i v_i$. This convention does not apply to Greek indices (e.g. α, β) which are specifically used in cases where the implied summation would not be natural or wrong.

Lower-Case Greek Symbols

$\delta(x)$	Dirac delta functional, eq. (3.2), page 15
δ_{ij}	Kronecker delta (1 if $i = j$, 0 otherwise), page 22
η	Local time-stepping parameter, eq. (10.8), page 88
λ	Temperature conductivity coefficient, page 26
μ	Dynamic viscosity, page 23
μ_T	Turbulent/Eddy viscosity, page 38
ν	Kinematic viscosity (μ/ρ), page 24
ν_T	Kinematic turbulent/eddy viscosity ($\nu_T = \mu_T/\langle\rho\rangle$), page 40
ρ	Fluid density, eq. (2.2), page 8
ρ_α	Density of species α in the mixture, page 9

σ_k Turbulent Prandtl number, page 39

σ_X Standard deviation of random variable X, eq. (3.3), page 15

$\boldsymbol{\sigma}$ Internal stress tensor, page 22

τ_{avg} Averaging time scale, page 80

τ_k Correction-drift time scale for the turbulent kinetic energy, page 84

τ_U Correction-drift time scale for the mean velocity, page 83

$\boldsymbol{\tau}$ Shear stress tensor $(\sigma_{ij} + p\delta_{ij})$, page 22

$\upsilon^f_{\alpha,i}$ Stoichiometric coefficient of species α in forward-reaction i, page 27

$\upsilon^r_{\alpha,i}$ Stoichiometric coefficient of species α in reverse-reaction i, page 27

ϕ Fuel equivalence ratio, page 52

$\boldsymbol{\phi}$ Vector of all scalars, e.g. mass fractions and temperature, page 28

χ Scalar dissipation rate of z, eq. (8.5), page 57

$\widetilde{\chi}_\alpha$ Dissipation rate of scalar α, eq. (7.1), page 43

$\dot{\omega}_\alpha$ Chemical source term of species α, eq. (5.2), page 27

ω^* Particle turbulence frequency, page 68

Upper-Case Greek Symbols

Γ_α Diffusivity of species α into the mixture, page 25

$\Gamma_{\alpha\beta}$ Binary mass diffusion coefficient of species α into species β, page 25

$\boldsymbol{\Lambda}$ Element matrix, page 28

$\boldsymbol{\Upsilon}$ Reaction coefficient matrix $\left(\upsilon^r_{\alpha,i} - \upsilon^f_{\alpha,i}\right)$, page 27

Ω Arbitrary control volume, page 19

Lower-Case Roman Symbols

c_p Specific heat capacity at constant pressure, eq. (2.19), page 11

$c_{p,\alpha}$ Specific heat capacity at constant pressure for species α, page 9

$c^m_{p,\alpha}$ Molar heat capacity at constant pressure for species α, page 10

c_v Specific heat capacity at constant volume, eq. (2.19), page 11

$c_{v,\alpha}$ Specific heat capacity at constant volume for species α, page 9

$c^m_{v,\alpha}$ Molar heat capacity at constant volume for species α, page 10

e Inner energy of the gas mixture, eq. (2.21), page 11

e_α Inner energy of species α, eq. (2.16), page 11

e_s Sensible inner energy of the gas mixture, eq. (2.23), page 12

$e_{s,\alpha}$ Sensible inner energy of species α, eq. (2.16), page 11

e_t Total energy of the gas mixture, eq. (2.25), page 12

f_X Probability density function of random variable X, eq. (3.2), page 14

$\boldsymbol{f}^e$ External force acting on the fluid, page 22

$\boldsymbol{f}^i$ Internal force acting on the fluid, page 22

h Enthalpy of the gas mixture, eq. (2.21), page 11

h_α Enthalpy of species α, eq. (2.16), page 11

h_s Sensible enthalpy of the gas mixture, eq. (2.23), page 12

$h_{s,\alpha}$ Sensible enthalpy of species α, eq. (2.16), page 11

$h^m_{s,\alpha}$ Molecular sensible enthalpy of species α, page 11

h_t Total enthalpy of the gas mixture, eq. (2.25), page 12

$\Delta h^0_{f,\alpha}$ Standard heat of formation of species α at T_0, page 10

$\Delta h^0_{s,\alpha}$ Enthalpy of species α at T_0, page 10

k Turbulent kinetic energy $\left(\widetilde{u_i'' u_i''}\right)$, eq. (6.18), page 38

k_i^f Forward rate constant of reaction i, eq. (5.5), page 28

k_i^r Reverse rate constant of reaction i, eq. (5.6), page 28

$\boldsymbol{n}$ Normal vector, page 22

p Fluid pressure, eq. (2.6), page 9

p_α Partial pressure of species α in the mixture, eq. (2.8), page 9

q Particle mass density, page 69

s Mass-stoichiometric ratio, eq. (8.1), page 52

$\boldsymbol{w}$ Coefficient vector, page 30

z Bilger Mixture fraction, eq. (8.3), page 55

Upper-Case Roman Symbols

C_α Molar concentration of species α, eq. (2.5), page 9

C_{diff} Coefficient in the particle distribution correction scheme, page 84

C_{max} Upper threshold coefficient for the particle number control, page 86

C_{min} Lower threshold coefficient for the particle number control, page 86

C_ϕ IEM mixing model constant, page 49

C_χ Coefficient in the scalar dissipation rate model, page 78

D Diffusion coefficient, page 21

$\frac{\mathrm{D}}{\mathrm{D}t}$ Convective or material derivative $\left(\frac{\partial}{\partial t} + \frac{\partial U_i}{\partial x_i}\right)$, page 23

$\mathbf{D}$ Diffusion coefficient tensor, page 21

E Total non-chemical energy of the gas mixture, eq. (2.27), page 12

F_X CDF of random variable X, eq. (3.1), page 13

$\boldsymbol{F}$ Flux vector of a conserved scalar quantity, page 19

$\mathbf{F}$ Flux tensor of a conserved vector quantity, page 21

H Total non-chemical enthalpy of the gas mixture, eq. (2.27), page 12

K Time-averaging parameter, page 80

Le_α Lewis number of scalar α, eq. (8.4), page 57

$\mathcal{M}_\alpha$ Chemical symbol for species α, page 27

N_c Number of conserved scalars, page 29

N_e Number of elements in the chemical system, page 28

N_{FV} Number of sub-iterations the RANS solver performs, page 75

N_{in} Number of inflow streams, page 30

N_{MC} Number of sub-iterations the JPDF solver performs, page 75

N_r Number of chemical reactions, page 27

N_s Number of species in the mixture, page 9

N_Υ Rank of the reaction coefficient matrix $\boldsymbol{\Upsilon}$, page 29

$\dot{Q}$ Energy source term, page 26

Q^V Volume source of a conserved scalar quantity, page 19

$\boldsymbol{Q}^S$ Surface source vector of a conserved scalar quantity, page 19

$\boldsymbol{Q}^V$ Volume source vector of a conserved vector quantity, page 21

$\mathbf{Q}^S$ Surface source tensor of a conserved vector quantity, page 21

R Specific gas constant, eq. (2.7), page 9

R_u Universal gas constant, page 9

$\boldsymbol{R}$ Reaction rate vector, eq. (5.3), page 28

$\boldsymbol{S}$ Outwards-oriented surface of control volume Ω, page 19

$\mathbf{S}$ Strain rate tensor, page 23

T Fluid temperature, page 9

T_0 Reference temperature (298.15 K), page 10

$\mathcal{U}$ Conserved scalar quantity, page 19

$\boldsymbol{\mathcal{U}}$ Conserved vector quantity, page 21

$\boldsymbol{U}$ Fluid velocity vector, page 20

W Mean molecular weight of mixture, eq. (2.4), page 9

W_α Molecular mass of species α, page 9

X_α Mole fraction of species α, eq. (2.3), page 9

Y_α Mass fraction of species α, eq. (2.1), page 8

Abbreviations

CDF Cumulative distribution function, page 13

DNS Direct numerical simulation, page 2

FV Finite volumes discretisation method, page 61

GLM Generalised Langevin model, page 47

IEM Interaction by exchange with the mean mixing model, page 49

JPDF Joint probability density function, page 16

LDV Laser Doppler velocimetry, page 111

MC Monte-Carlo method, page 61

MDF Mass-density function ($\rho(\boldsymbol{\psi})f(\boldsymbol{V}, \boldsymbol{\psi}; x, t)$), page 46

PDF Probability density function, page 14

RMS Root-mean-square, page 37

SDE Stochastic differential equation, page 61

SLM Simplified Langevin model, page 47

SVD Singular value decomposition, page 29

TKE Turbulent kinetic energy k, page 38

Preface

In today's industrialised, highly mobile world, combustion for energy conversion plays a very important role. Thanks to the high energy density of the solid, liquid and gaseous fuels that are in common use, combustion devices, like no other technology, are very compact. Despite the sinister prospect of peak oil[1] being reached soon and the dreary consequences of human-made global warming, fossil fuels will remain essential to transportation and energy production in the foreseeable future. While electric cars for individual transportation, alternative energies and CO_2 sequestration for electricity production potentially offer at least partial remedy to these problems, no new technology is in sight for cargo ships and air planes, both of which the globalised economy heavily relies on. Further, the global reserves in coal and natural gas are vastly larger than those in oil, making it unlikely that energy production will depend less heavily on fossil fuels any time soon. This has become even more pronounced since the catastrophe in Fukushima, after which the general acceptance of nuclear energy has dropped sharply. Hence, for economical and ecological reasons, it is important that combustion devices continue to be improved; efficiency needs to be increased and the emission of pollutants must be further reduced.

The high costs and long iteration cycles of experimental investigations make efficient and accurate simulation tools a crucial component in the continued development of combustion devices. While numerical simulation tools for structural analysis are both mature and broadly applied in the industry, the simulation of fluids, especially of highly turbulent flows, has become commonplace only in recent years and is still considered to be a very challenging problem, requiring great experience in order to obtain meaningful and accurate results. The strong interaction of turbulence with chemical reactions, a large research field of its own, makes the simulation

[1] The point in time where the maximum rate of crude oil production is reached, after which it enters a terminal decline. The concept was first presented by Hubbert [29].

of combustion devices a formidable problem indeed. While the governing equations are known and sophisticated chemical mechanisms are available, the time and length scales involved in the chemical processes can be orders of magnitudes smaller than those of the turbulent flow problem, rendering direct numerical simulation (DNS) intractable for anything but the most simplified scenarios. This fact necessitates the development of appropriate models and algorithms for the solution of turbulent reactive flow problems.

Over the last decades, several approaches to the modelling of turbulent combustion have been devised, many of which rely on spatial or temporal homogenisation or filtering and ensemble averaging in order to make the simulation computationally feasible. The major challenge lies now in the physical and mathematical modelling of the effects that have fallen victim to these simplifications. Of particular importance to turbulent combustion are the effects of diffusion due to the unresolved gradients, requiring the development of so called *mixing models* that try to emulate the molecular diffusion based on large scale quantities. Another major issue is the appearance of unclosed correlation terms in the governing equations due to the averaging and filtering operations. Lastly, the chemical source terms which are highly non-linear and strongly dependent on the molecular composition proved to be particularly difficult to model.

The method of transported joint probability functions has been one of the most successful approaches for the simulation of turbulent reactive flows. As will be shown in this work, this method provides second order closures for the unclosed correlations and the chemical source term is even fully closed, not requiring any difficult to justify assumptions. These methods solve for a function defined in a high dimensional space, barring the use of conventional solution techniques for partial differential equations, such as finite differences, finite elements or finite volumes, for which the computational cost scales approximately with the power of the number of dimensions.

In the past, special stochastic particle and field algorithms using Monte-Carlo simulation concepts have been developed for this kind of probability density function method specifically. The stochastic nature of the method, however, introduces new and unique algorithmic challenges; consistency criteria must be fulfilled, stochastic and systematic bias errors need to be controlled and computational efficiency should be guaranteed. In order to reduce the stochastic and bias errors and improve convergence properties, hybrid schemes have been proposed, combining the robustness of conventional techniques with the advantages of the transported joint probability density function methods. This work presents a novel method of this hy-

brid type, implemented in a powerful open-source framework, offering great geometric flexibility and unparalleled extensibility.

In the first part, the reader is introduced to the physical and mathematical foundations of turbulent combustion and the simulation method. Sections 2 and 3 lay out the thermo-chemical relations and the probability theory that are essential to the understanding of the subsequent text. The basic flow equations are derived and presented in Section 4 and the treatment of the reaction chemistry is touched upon in Section 5. After having described the physical model, the reader is given an overview of the relevant turbulence modelling approaches in Section 6, the transported joint probability density function method is presented in Section 7 and popular models for the modelling of the turbulent combustion are very briefly discussed in Section 8.

The solution algorithm is presented in the second part of this work. After introducing the stochastic method in Section 9, the novel hybrid algorithm is presented in Section 10 and Section 11 gives a brief overview of the implementation of the previously described algorithm. The third part is concerned with the validation and numerical properties of the algorithm. Simulation results and convergence studies using four different flow cases are presented.

Part I
Physical Model

1 Introduction

This part is dedicated to establishing the mathematical model describing all relevant physical processes. First the most relevant thermochemical relations and basic probability theory are presented, then the concept of conservation laws is briefly introduced, followed by the derivation of the fundamental equations of fluid dynamics, the Navier-Stokes equations. This set of equations describes the evolution of the conserved quantities – mass, momentum, energy and species mass.

Subsequently the fundamentals of chemistry will be introduced. Reaction kinetics will be touched upon, followed by a brief exposé on the nature of turbulent combustion. Simple chemistry modelling approaches will be introduced thereafter, together with the presentation of the concepts and a simple model for molecular mixing, completing the description of the physical model.

2 Thermochemical Relations

This section will establish often used thermochemical relations that are of great importance in later sections, in particular when deriving the species mass conservation equation in Section 4.6 and when introducing chemical reactions in Section 5. The detailed discussion of the chemical properties of a fluid and the chemical reactions will be postponed to said section.

When simulating reactive flows the fluid is composed of many different kinds of molecules which through chemical reactions are consumed and re-formed into many new species. Even apparently simple cases, such as methane-air combustion, can involve a surprisingly large number of chemical species – e.g. the GRI-3.0 mechanism [76] contains 53 species. It is therefore necessary to derive equations and relations governing the species composition.

The composition can be described in terms of mass fractions, mole fractions or molar concentrations, Y_α, X_α and C_α, respectively. The former is defined as the fraction of the mass of species α with respect to the total mass in any given volume$\|\Omega\|$ of infinitesimal size:

$$Y_\alpha \equiv \frac{m_\alpha}{m} \quad , \tag{2.1}$$

where m_α is the mass of species α and m is the total mass in volume Ω. Being the fraction of two masses, this is a dimensionless quantity. The fluid density ρ is then given by

$$\rho \equiv \frac{m}{\|\Omega\|} \tag{2.2}$$

and has the dimension $^{\mathrm{kg}}/_{\mathrm{m}^3}$. The mole (volume) fraction X_α is related to the mass fraction Y_α through

$$X_\alpha = \frac{W}{W_\alpha} Y_\alpha \tag{2.3}$$

and is, as the mass fraction, dimensionless. Here, W is the mean molecular mass defined as

$$W \equiv \left(\sum_{\alpha=1}^{N_s} \frac{Y_\alpha}{W_\alpha} \right)^{-1} = \sum_{\alpha=1}^{N_s} X_\alpha W_\alpha \quad . \tag{2.4}$$

W_α is the molecular mass of species α. Up to the mass-defect due to the binding-energy, which for the purposes of this work is negligible, it is the sum over the atomic masses of the elements comprising the molecule of species α. N_s is the number of species in the mixture. Lastly, the molar concentration is related to the mass and mole fractions through

$$C_\alpha = \rho \frac{Y_\alpha}{W_\alpha} = \rho \frac{X_\alpha}{W} \tag{2.5}$$

and expresses the amount of matter per unit volume ($^{\mathrm{mol}}/_{\mathrm{m}^3}$, also $^{\mathrm{mol}}/_{\mathrm{L}}$).

For a mixture of ideal gases, the constitutive relation is

$$p = \rho R T \quad , \tag{2.6}$$

where p is the pressure (measured in $\mathrm{Pa} = {}^{\mathrm{kg}}/_{\mathrm{m\,s}^2}$), R the specific gas constant for the mixture with dimensions $^{\mathrm{J}}/_{\mathrm{kg\,K}}$ and T is the temperature, specified in K. This is also known as the *ideal gas law*. The specific gas constant of the mixture is related to the universal gas constant $R_u = 8.3144621\ {}^{\mathrm{J}}/_{\mathrm{mol\,K}}$ through

$$R = \frac{R_u}{W} \quad , \tag{2.7}$$

The partial pressure of species α is

$$p_\alpha = \rho_\alpha \frac{R_u}{W_\alpha} T \quad , \tag{2.8}$$

where $\rho_\alpha = Y_\alpha \rho$ is the density of species α. The total pressure p is the sum over all partial pressures p_α

$$p = \sum_{\alpha=1}^{N_s} p_\alpha = R_u T \sum_{\alpha=1}^{N_s} \frac{\rho_\alpha}{W_\alpha} = \rho R_u T \sum_{\alpha=1}^{N_s} \frac{Y_\alpha}{W_\alpha} = \rho \frac{R_u}{W} T \quad . \tag{2.9}$$

Introducing $c_{p,\alpha}$ and $c_{v,\alpha}$ as the specific heat capacities of species α at constant pressure and constant volume, respectively, Mayer's relation states that

$$\frac{R_u}{W_\alpha} = R_\alpha = c_{p,\alpha} - c_{v,\alpha} \quad . \tag{2.10}$$

Both express the amount of energy required to heat one kilogram of species α by one Kelvin and have the dimension $^{\mathrm{J}}/_{\mathrm{kg\,K}}$ – the former does so for an isobaric (constant pressure) process, the latter for an isochoric (constant volume) process. They are related to the corresponding molar quantities with the dimension $^{\mathrm{J}}/_{\mathrm{mol\,K}}$ through

$$\begin{aligned} c_{p,\alpha}^{m} &= W_\alpha c_{p,\alpha} \quad \text{and} \\ c_{v,\alpha}^{m} &= W_\alpha c_{v,\alpha} \quad . \end{aligned} \tag{2.11}$$

Note that $c_{p,\alpha}$, for most gases, is strongly temperature dependent and is usually computed from polynomial fits, such as provided by the NIST JANAF thermochemical database [11].

In combustion theory, many different definitions of energy are commonly in use and are equally important as they express different concepts. It is assumed that the enthalpy h_α of species α is given by

$$h_\alpha = \int_{T_0}^{T} c_{p,\alpha} \mathrm{d}T + \Delta h_{f,\alpha}^{0} + h_{s,\alpha}^{0} \quad . \tag{2.12}$$

Here, the standard heat of formation of species α at an arbitrarily chosen reference temperature T_0 is denoted by $\Delta h_{f,\alpha}^{0}$. It is conventional to choose $T_0 = 298.15\,\mathrm{K}$ as, in contrast to the perhaps more obvious choice of $0\,\mathrm{K}$, this temperature is easily accessible experimentally. Note that the second term in (2.12) is the chemical energy contained in species α. Defining the enthalpy at the reference temperature T_0 as $h_{s,\alpha}^{0}$, it follows that the sensible enthalpy $h_{s,\alpha}$ must be defined by the first and third term of (2.12).

The sensible inner energy $e_{s,\alpha}$ is defined to satisfy $h_{s,\alpha} = e_{s,\alpha} + {}^{p_\alpha}/_{\rho_\alpha}$. The sensible inner energy $e_{s,\alpha}$, sensible enthalpy $h_{s,\alpha}$, the inner energy e_α and the enthalpy h_α are summarised by

$$h_{s,\alpha} = \int_{T_0}^{T} c_{p,\alpha} \mathrm{d}T + h_{s,\alpha}^{0} \quad , \tag{2.13}$$

$$h_\alpha = h_{s,\alpha} + \Delta h_{f,\alpha}^{0} \quad , \tag{2.14}$$

$$e_{s,\alpha} = \int_{T_0}^{T} c_{v,\alpha} \mathrm{d}T - R_\alpha T_0 + h_{s,\alpha}^{0} \tag{2.15}$$

and

$$e_\alpha = e_{s,\alpha} + \Delta h_{f,\alpha}^{0} \quad . \tag{2.16}$$

It is important to understand that the sensible enthalpy and the sensible inner energy represent the non-chemical forms of energy.

The corresponding molecular quantities can be obtained by multiplication with the molecular mass, e.g. the molecular sensible enthalpy is given by

$$h^m_{s,\alpha} = W_\alpha h_{s,\alpha} \quad . \tag{2.17}$$

The heat capacities for a mixture of N_s species at constant pressure (c_p) and constant volume (c_v) are obtained through

$$c_p = \sum_{\alpha=1}^{N_s} c_{p,\alpha} Y_\alpha = \sum_{\alpha=1}^{N_s} c^m_{p,\alpha} \frac{Y_\alpha}{W_\alpha} \quad \text{and} \tag{2.18}$$

$$c_v = \sum_{\alpha=1}^{N_s} c_{v,\alpha} Y_\alpha = \sum_{\alpha=1}^{N_s} c^m_{v,\alpha} \frac{Y_\alpha}{W_\alpha} \quad . \tag{2.19}$$

The inner energy and enthalpy of the mixture are given by the mass-fraction weighted sum of the corresponding quantity of the individual species:

$$\begin{aligned} h &= \sum_{\alpha=1}^{N_s} Y_\alpha h_\alpha = \sum_{\alpha=1}^{N_s} Y_\alpha \left(\int_{T_0}^{T} c_{p,\alpha} \mathrm{d}T + \Delta h^0_{f,\alpha} + h^0_{s,\alpha} \right) \\ &= \int_{T_0}^{T} c_p \mathrm{d}T + \sum_{\alpha=1}^{N_s} Y_\alpha \left(\Delta h^0_{f,\alpha} + h^0_{s,\alpha} \right) \quad , \end{aligned} \tag{2.20}$$

$$\begin{aligned} e &= \sum_{\alpha=1}^{N_s} Y_\alpha \left(\int_{T_0}^{T} c_{v,\alpha} \mathrm{d}T - R_\alpha T_0 + \Delta h^0_{f,\alpha} + h^0_{s,\alpha} \right) \\ &= \int_{T_0}^{T} c_v \mathrm{d}T - R T_0 + \sum_{\alpha=1}^{N_s} Y_\alpha \left(\Delta h^0_{f,\alpha} + h^0_{s,\alpha} \right) = \sum_{\alpha=1}^{N_s} Y_\alpha e_\alpha \quad . \end{aligned} \tag{2.21}$$

The sensible enthalpy and inner energy consequently are

$$h_s = \int_{T_0}^{T} c_p \mathrm{d}T + h^0_s \quad \text{and} \tag{2.22}$$

$$e_s = \int_{T_0}^{T} c_v \mathrm{d}T - R T_0 + h^0_s \quad . \tag{2.23}$$

Total energies and enthalpies are defined by inclusion of the kinetic energy. The total enthalpy and energy (including chemical energy or enthalpy, respectively) are defined by

$$h_t = h + \frac{U_i U_i}{2} \quad \text{and} \tag{2.24}$$

$$e_t = e + \frac{U_i U_i}{2} \quad . \tag{2.25}$$

The total non-chemical energy and enthalpy follow as

$$H = h_s + \frac{U_i U_i}{2} \quad \text{and} \tag{2.26}$$

$$E = e_s + \frac{U_i U_i}{2} \quad . \tag{2.27}$$

3 Probability Theory

Here, a short review and introduction to probability theory is given. It is by no means complete, the only intention is to familiarise the reader with the concepts relevant to this work.

3.1 Random Variables and Probability

A *random variable* X is, like any variable, defined for a certain range of allowable values, here called Ω. The distinguishing feature of random variables, however, is that their value is uncertain and associated to a probability. Ω is consequently called a *probability space* or *sample space*.

A specific value that X can take is referred to as the *sample space* variable, and is denoted with the lower-case symbol x here. In contrast to the random variable X, x is an independent variable.

The probability of the event $A \equiv x_1 \leqslant X < x_2$ is given by $P(x_1 \leqslant X < x_2)$, or using a short-hand notation, $P(A)$. A probability is always in the range $[0, 1]$, where 0 indicates that the event is impossible and 1 asserts absolute certainty. For non-overlapping events A and B, probabilities are additive, i.e. $P(A \cup B) = P(A) + P(B)$.

3.2 Probability Density and Distribution Functions

The probability of events having an upper bound only is defined by the cumulative distribution function (CDF)

$$F_X(x) = P(X < x) \quad . \tag{3.1}$$

It must be monotonically increasing with x. This can be seen for $x_2 > x_1$:

$$F_X(x_2) = P(X < x_2) = \underbrace{P(X < x_1)}_{=F_X(x_1)} + \underbrace{P(x_1 \leqslant X < x_2)}_{\geqslant 0}$$

By definition, for $X \in \Omega = (-\infty, \infty)$, $F_X(-\infty) = 0$ and $F_X(\infty) = 1$.

The CDF can be expressed as the limit of an infinite number of independent measurements x_i for $i = 1 \ldots n$:

$$F_X(x) = \lim_{n\to\infty} \frac{1}{n} \sum_{i=1}^{n} H(x - x_i) = \lim_{n\to\infty} \frac{m(x)}{n} \quad .$$

Here, $H(x)$ is the Heaviside step function

$$H(x) = \begin{cases} 0 & \text{for } x < 0 \\ 1 & \text{for } x \geqslant 0 \end{cases}$$

and $m(x)$ is the number of measurements where $x_i < x$.

For the event that $x \leqslant X < x + \Delta x$

$$P(x \leqslant X < x + \Delta x) = F_X(x + \Delta x) - F_X(x)$$

is obtained. Dividing by Δx and taking the limit $\Delta x \to 0$ provides the definition of the probability density function (PDF)

$$f_X(x) \equiv \lim_{\Delta x\to 0} \frac{F_X(x + \Delta x) - F_X(x)}{\Delta x} = \frac{\mathrm{d}F_X(x)}{\mathrm{d}x} \quad . \tag{3.2}$$

Since the CDF is monotonically increasing, $f_X(x) \geqslant 0$. From above definition it follows that

$$P(x_1 \leqslant X < x_2) = \int_{x_1}^{x_2} f_X(x)\mathrm{d}x$$

and since X must be within Ω

$$\int_{\Omega} f_X(x)\mathrm{d}x = 1 \quad .$$

Using the frequency definition of the CDF from above, we obtain

$$f_X(x) = \frac{\mathrm{d}F_X(x)}{\mathrm{d}x} = \lim_{n\to\infty} \frac{1}{n} \sum_{i=1}^{n} \frac{\mathrm{d}H(x - x_i)}{\mathrm{d}x} = \lim_{n\to\infty} \frac{1}{n} \sum_{i=1}^{n} \delta(x - x_i)$$

where $\delta(x)$ is the Dirac delta functional with the somewhat peculiar properties

$$\begin{aligned} \delta(x) &= 0 \quad \text{for } x \neq 0 \quad , \\ \delta(x) &\neq 0 \quad \text{for } x = 0 \quad \text{and} \\ \int_{-\infty}^{\infty} \delta(x)\mathrm{d}x &\equiv 1 \quad . \end{aligned}$$

Sometimes, $\delta(x)$ is also referred to as the *fine-grained PDF*, giving the probability of $X = x$. A very important property of the fine-grained PDF is the so called *sifting property*

$$\int_{-\infty}^{+\infty} g(x')\delta(x' - x)\mathrm{d}x' = g(x) \int_{-\infty}^{+\infty} \delta(x' - x)\mathrm{d}x' = g(x)$$

3.3 Statistical Moments

The first moment of X is defined as

$$E(X) = \mu_X = \langle X \rangle \equiv \int_{\Omega} x f_X(x)\mathrm{d}x \quad ,$$

which is also called the *mean* or *expectation* of X. Often, μ_X is used when referring to the value of the mean. $\langle \cdot \rangle$ is a shorthand notation for the mean operator, often used for convenience. The mean is a linear operator, i.e.

$$\begin{aligned} \langle a g(X) \rangle &= a \langle g(X) \rangle \quad \text{and} \\ \langle g(X) + h(X) \rangle &= \langle g(X) \rangle + \langle h(X) \rangle \end{aligned}$$

for arbitrary functions $g(x)$ and $h(x)$ and constant a.

Expectations of the form $\langle (X - \langle X \rangle)^m \rangle$ with $m \in \{1, 2, \ldots\}$ are called *central moments*, and the particular choice

$$\mathrm{Var}(X) = \sigma_X^2 = \left\langle (X - \langle X \rangle)^2 \right\rangle \tag{3.3}$$

is the *variance*. By taking the square-root of the variance, the *standard deviation* is obtained, often denoted as σ_X. It is a measure for the uncertainty that is associated with the estimate given by the expectation. The central moments with $m = 3$ and $m = 4$ are called the *skewness* and *kurtosis*, respectively.

By expanding the definition of the variance, one sees that it is linked to the second moment and the mean through

$$\left\langle (X - \langle X \rangle)^2 \right\rangle = \left\langle X^2 \right\rangle - \langle X \rangle^2 \quad .$$

An important property of any even PDF (i.e. for which $f_X(x) = f_X(-x)$) is that the skewness and all higher odd-numbered central moments are zero.

Bringing together the definition of the mean and the fine-grained PDF, the following, very important property is found

$$\langle \delta(X - x) \rangle = \int_{\Omega} \delta(x' - x) f_X(x') \mathrm{d}x' = f(x) \quad .$$

3.4 Multiple Random Variables

When multiple random variables are relevant and their functional dependence is not known, joint density functions are required to describe the probabilities. The event that two random variables X and Y simultaneously fulfil $A = \{X < x, Y < y\}$ is given by the *joint CDF* $F_{XY}(x, y)$. From the previous definitions for a single random variable, it follows that

$$\begin{aligned} P(x \leqslant X < x + \Delta x, y \leqslant Y < y + \Delta y) = \\ F_{XY}(x + \Delta x, y + \Delta y) - F_{XY}(x, y + \Delta y) \\ - F_{XY}(x + \Delta x, y) + F_{XY}(x, y) \end{aligned}$$

Following the same procedure as for the univariate case, the joint PDF (JPDF) is obtained through division by Δx and Δy and taking the limit, resulting in

$$f_{XY}(x, y) = \frac{\partial^2 F_{XY}(x, y)}{\partial x \partial y} \quad .$$

For more random variables, it is convenient to collect them in a random vector $\boldsymbol{X} = [X_1, X_2, \ldots]^T$.

Note that the variance of the random vector $\boldsymbol{X}$ in the multivariate case is a tensor, the *covariance matrix* $\mathbf{C}$:

$$\begin{aligned} C_{ij} &\equiv \langle (X_i - \langle X_i \rangle)(X_j - \langle X_j \rangle) \rangle \\ &= \int_{\mathbb{R}^2} (x_i - \langle X_i \rangle)(x_j - \langle X_j \rangle) f_{ij}(x_i, x_j) \mathrm{d}x_i \mathrm{d}x_j \quad , \end{aligned}$$

where the marginal joint PDF of X_i and X_j is given by

$$f_{ij}(x_i, x_j) = \int_{\mathbb{R}^{n-2}} f_{\boldsymbol{X}}(\boldsymbol{x}) \prod_{\substack{k=1 \\ k\neq i \\ k\neq j}}^{n} \mathrm{d}x_k \quad ,$$

n being the size of the random vector $\boldsymbol{X}$. Notice that the diagonal entries are the variances of the individual random variables and that the covariance matrix is symmetric by definition.

Normalising the covariance matrix with the standard deviations leads to the correlation coefficient matrix

$$\varrho_{ij} = \frac{C_{ij}}{\sigma_i \sigma_j} \quad ,$$

where the *Cauchy-Schwarz inequality* requires that

$$-1 \leqslant \varrho_{ij} \leqslant 1 \quad .$$

As for the univariate case, the JPDF can be defined in terms of the fine grained PDF:

$$f_{\boldsymbol{X}}(\boldsymbol{x}) = \langle \delta(X_1 - x_1)\delta(X_2 - x_2)\cdots\delta(X_n - x_n)\rangle \quad .$$

Given $F_{XY}(x, y)$ for two random variables X and Y, the probability distribution of X regardless of a second random variable Y is given by the *marginal* joint CDF $F_X(x) = F_{XY}(x, \infty)$. The corresponding marginal joint PDF follows as

$$f_X(x) = \int_{\mathbb{R}} f_{XY}(x, y)\mathrm{d}y \quad .$$

The probability density of a random variable X *given* that $Y = y$ is determined by the *conditional PDF* defined through

$$f_{X|Y}(x|y) = \frac{f_{XY}(x, y)}{f_Y(y)} \quad ,$$

which is an essential ingredient for this work. For the special case where $f_{X|Y}(x) = f_X(x)$ it follows that

$$f_{XY}(x, y) = f_X(x) f_Y(y)$$

and the random variables X and Y are said to be *statistically independent*.

The conditional mean of any arbitrary function $g(x, y)$ is defined through the conditional PDF as

$$\langle g(X,Y)|Y=y\rangle = \int_{\Omega} g(x,y) f_{X|Y}(x|y)\mathrm{d}x \quad .$$

The short-hand notation commonly used is $\langle g(X,Y)|y\rangle$.

3.5 Central Limit Theorem

The summation of a large but finite number n of statistically independent, identically distributed random variables X_i with mean $\langle X\rangle$ and standard deviation σ_X is, due to n being finite, itself a random number. Estimating the mean as

$$Y = \langle X\rangle_n = \frac{1}{n}\sum_{i=1}^{n} X_i \quad ,$$

the *central limit theorem* postulates that the PDF of this estimator Y is

$$f_Y(y) = \frac{1}{\sqrt{2\pi}\sigma_X/\sqrt{N}} \exp\left(-\frac{(y-\langle X\rangle)^2}{2\sigma_X^2/N}\right) \quad .$$

Notice, that the mean of the random variable Y is $\langle X\rangle$ and the standard deviation is $\sigma_Y = \sigma_X/\sqrt{N}$. In the limit of $N \to \infty$, the mean estimator is non-random and converges to $\langle X\rangle$. At the same time, $\sigma_X = 0$ and $f_Y(y) \to \delta(y - \langle X\rangle)$. The important result of the central limit theorem is, that in order to reduce the uncertainty σ_Y by a factor of m, m^2 times as many samples are required.

4 Conservation Laws

This section is dedicated to establishing the governing flow equations. Starting from the general concept of a conservation law, the convective-diffusive type of equation is derived, from which the transport equations for mass, momentum, species mass and energy are established.

4.1 The General Form of a Scalar Conservation Law

The evolution of any conserved scalar $\mathcal{U}$ can be described by considering a balance equation over an arbitrary control volume Ω with outwards-oriented surface $\boldsymbol{S}$

$$\frac{\partial}{\partial t}\int\limits_{\Omega}\mathcal{U}\mathrm{d}\Omega+\oint\limits_{S}F_i\,\mathrm{d}S_i=\int\limits_{\Omega}Q^V\mathrm{d}\Omega+\oint\limits_{S}Q_i^S\mathrm{d}S_i \tag{4.1}$$

where $\boldsymbol{F}$ represents the flux of $\mathcal{U}$ per unit surface and unit time and Q^V and $\boldsymbol{Q}^S$ are the volume and surface sources of $\mathcal{U}$, respectively (Hirsch [28]).

Equations of this form are said to be in *integral conservation form* and are valid for any arbitrary volume Ω with surface S. They even hold in the presence of shocks, i.e. discontinuities in the fluxes, as the flux function does not appear under any differential operator. Lastly, the internal variations of the conserved scalar $\mathcal{U}$, in the absence of a volume source (Q^V), depends only on the flux and source contributions through the surfaces, not the fluxes in the interior of Ω.

By applying Gauss' theorem to the surface integrals, a differential form of (4.1) can be obtained. The theorem states that the volume integral of the divergence of a flux field is equal to the surface integral of the same flux field:

$$\int\limits_{\Omega}\frac{\partial F_i}{\partial x_i}\mathrm{d}\Omega=\oint\limits_{S}F_i\,\mathrm{d}S_i\quad . \tag{4.2}$$

Applying (4.2) to the surface integrals in (4.1) it follows that

$$\frac{\partial}{\partial t}\int_{\Omega}\mathcal{U}\mathrm{d}\Omega+\int_{\Omega}\frac{\partial F_i}{\partial x_i}\mathrm{d}\Omega=\int_{\Omega}Q^V\mathrm{d}\Omega+\int_{\Omega}\frac{\partial Q_i^S}{\partial x_i}\mathrm{d}\Omega \quad .$$

Since above equation must be valid for any control volume Ω it must hold locally for any given point, resulting in the *differential form of the conservation law*

$$\frac{\partial \mathcal{U}}{\partial t}+\frac{\partial}{\partial x_i}\left(F_i-Q_i^S\right)=Q^V \quad , \tag{4.3}$$

where the surface source has been grouped together with the flux vector. It is of great importance to note that this differential form is only valid for continuous flux functions and surface sources, i.e. it does not hold in the presence of shocks.

4.2 Convective-Diffusive Conservation Laws

So far the nature of the flux function $\boldsymbol{F}$ has not been considered. This is where the physics of a given problem is introduced, describing the spatial transport of the conserved quantity $\mathcal{U}$. In fluid dynamics there are generally two possible causes for a flux – convection and molecular diffusion. The former is due to convective transport, i.e. the property is transported by the flow not unlike a small silt particle is carried away in a river. Diffusive fluxes, however, even occur in a fluid at rest since the molecular diffusion is due to thermal movements of the molecules.

The convective flux $\boldsymbol{F}^C$ describes how the conserved quantity $\mathcal{U}$ is carried away by the fluid velocity $\boldsymbol{U}$. It must be present for any conserved quantity and is given by

$$F_i^C=U_i\mathcal{U} \quad . \tag{4.4}$$

The second flux contribution, the diffusive flux $\boldsymbol{F}^D$, on the other hand, is independent of the fluid velocity. It captures the continuum effects caused by the Brownian motion of the individual molecules and describes the tendency of any fluid for homogenisation. In contrast to the convective flux, not all conserved quantities are subject to diffusion; e.g. density is not diffused since that would imply macroscopic displacement of fluid parcels. A good example is heat diffusion – consider a cold cube of steel being placed in a hot oven. The heat will slowly spread from the surface of the cube towards the interior until the oven temperature is reached everywhere. All of this happens without any macroscopic movement, just by vibrational energy

transfer inside the lattice. Consequently the diffusive flux must be proportional to the gradients of the conserved quantity and hence vanishes once equilibrium has been reached. These observations lead to the law of Fick

$$F_i^D = -\rho D_{ij} \frac{\partial \mathcal{U}/\rho}{\partial x_j} \quad , \tag{4.5}$$

where $\mathbf{D}$ is the diffusion coefficient with units m^2/s. In the general case of anisotropic diffusion, it is a tensor, but decays to a scalar D for isotropic diffusion. Substituting $\boldsymbol{F} = \boldsymbol{F}^C + \boldsymbol{F}^D$ into (4.3) results in a *convection diffusion equation*

$$\frac{\partial \mathcal{U}}{\partial t} + \frac{\partial U_i \mathcal{U}}{\partial x_i} = \frac{\partial}{\partial x_i} \left(\rho D_{ij} \frac{\partial \mathcal{U}/\rho}{\partial x_j} \right) + Q^V + \frac{\partial Q_i^S}{\partial x_i} \quad . \tag{4.6}$$

4.3 Vector Conservation Laws

If the conserved quantity is a vector $\boldsymbol{\mathcal{U}}$, the flux and surface source become tensors, i.e. $\mathbf{F}$ and $\mathbf{Q}^S$, respectively, and the volume source $\boldsymbol{Q}^V$ is now a vector

$$\frac{\partial}{\partial t} \int_\Omega \mathcal{U}_i \, \mathrm{d}\Omega + \oint_S F_{ij} \, \mathrm{d}S_j = \int_\Omega Q_i^V \mathrm{d}\Omega + \oint_S Q_{ij}^S \, \mathrm{d}S_j \quad . \tag{4.7}$$

Again, applying Gauss' theorem and using some re-grouping it is straight forward to obtain the differential form

$$\frac{\partial \mathcal{U}_i}{\partial t} + \frac{\partial}{\partial x_j} \left(F_{ij} - Q_{ij}^S \right) = Q_i^V \quad , \tag{4.8}$$

and inserting the flux definitions for convective-diffusive conservation laws, (4.4) and (4.5), leads to

$$\frac{\partial \mathcal{U}_i}{\partial t} + \frac{\partial U_j \mathcal{U}_i}{\partial x_j} = \frac{\partial}{\partial x_j} \left(\rho D_{jk} \frac{\partial \mathcal{U}_i/\rho}{\partial x_k} \right) + Q_i^V + \frac{\partial Q_{ij}^S}{\partial x_j} \quad . \tag{4.9}$$

4.4 Mass Conservation

The mass conservation equation describes the empirical fact that mass in a non-relativistic setting can neither be generated nor destroyed. Also, as already noted in 4.2, mass is not subject to diffusion. Here, the conserved quantity $\mathcal{U}$ is the density ρ. Substituting $\mathcal{U} = \rho$ in (4.6), it follows that the

mass conservation equation – commonly called the *continuity equation* – in differential form reads

$$\frac{\partial \rho}{\partial t} + \frac{\partial \rho U_i}{\partial x_i} = \frac{\partial}{\partial x_j}\left(\rho D_{ij} \frac{\partial \rho/\rho}{\partial x_i}\right) = 0 \quad . \tag{4.10}$$

For steady-state cases the temporal variation of the density vanishes and the continuity equation reduces to the compatibility condition

$$\frac{\partial \rho U_i}{\partial x_i} = 0 \tag{4.11}$$

and for constant density flows the spatial variation of the density also disappears, further simplifying the continuity equation to

$$\frac{\partial U_i}{\partial x_i} = 0 \quad , \tag{4.12}$$

requiring that the velocity field $\boldsymbol{U}$ is divergence free.

4.5 Momentum Conservation

The momentum conservation equation, momentum being the product of mass and velocity, is a vector equation of the form given by (4.9). Again, as for the mass conservation equation, it is assumed that there can be no diffusion of momentum in a fluid at rest, resulting in a vanishing diffusive flux contribution.

From Newton's law it is known that all variations of momentum in a system are due to forces acting on that system. Hence, determining the contribution of the sources requires the inspection of the forces acting on the volume Ω. These forces can be separated into internal and external forces (e.g. gravitation), $\rho \boldsymbol{f}^i$ and $\rho \boldsymbol{f}^e$, respectively. The internal force $\boldsymbol{f}^i$ must be due to the internal stress tensor $\boldsymbol{\sigma}$ acting on the surface element $\mathrm{d}\boldsymbol{S}$ with normal vector $\boldsymbol{n}$ as $\boldsymbol{f}^i = \boldsymbol{\sigma}\boldsymbol{n}$. Identifying the pressure as $p = -1/3\, \sigma_{ii}$ the stress tensor can further be decomposed into normal and shear stresses as

$$\sigma_{ij} = -p\delta_{ij} + \tau_{ij} \quad , \tag{4.13}$$

where δ_{ij} is the Kronecker delta defined to be 1 if $i = j$ and 0 otherwise and $\boldsymbol{\tau}$ is the shear stress tensor. For Newtonian fluids[2] in thermodynamic

[2] A fluid with an isotropic linear stress to strain-rate relationship that passes through the origin

equilibrium it is given by

$$\tau_{ij} = 2\mu \left(S_{ij} - \frac{1}{3} \frac{\partial U_k}{\partial x_k} \delta_{ij} \right) \quad , \tag{4.14}$$

μ being the dynamic viscosity with dimensions $^{\mathrm{kg}}/_{\mathrm{m\,s}}$ and $\mathbf{S}$ the strain rate tensor

$$S_{ij} = \frac{1}{2} \left(\frac{\partial U_i}{\partial x_j} + \frac{\partial U_j}{\partial x_i} \right) \quad . \tag{4.15}$$

Since the internal stresses must cancel out everywhere except at the boundary, they act as a surface source. The external forces $\boldsymbol{f}^e$, on the other hand, appear as volume sources in the momentum conservation equation. For multicomponent mixtures these forces act on each species individually, and the volume force expands to

$$f_i^e = \sum_{\alpha=1}^{N_s} Y_\alpha f_{\alpha,i}^e \quad , \tag{4.16}$$

where $\boldsymbol{f}_\alpha^e$ is the volume force acting on species α. In the further discussion, the summarised force $\boldsymbol{f}^e$ will be used for simplicity of notation.

Substituting $\mathcal{U} = \rho \boldsymbol{U}$ and the definitions for the surface and volume sources derived above into (4.9), the momentum transport equation, best known as the *Navier-Stokes* equation of motion, follows as

$$\begin{aligned} \frac{\partial \rho U_i}{\partial t} + \frac{\partial \rho U_j U_i}{\partial x_j} &= \frac{\partial \sigma_{ij}}{\partial x_j} + \rho f_i^e \\ &= -\frac{\partial p}{\partial x_i} + \frac{\partial \tau_{ij}}{\partial x_j} + \rho f_i^e \quad . \end{aligned} \tag{4.17}$$

Assuming a Newtonian fluid, using the definitions for the shear stress tensor (4.14) and the strain rate tensor (4.15), it follows that

$$\frac{\partial \rho U_i}{\partial t} + \frac{\partial \rho U_j U_i}{\partial x_j} = -\frac{\partial p}{\partial x_i} + \frac{\partial}{\partial x_j} \mu \left(\frac{\partial U_i}{\partial x_j} + \frac{\partial U_j}{\partial x_i} - \frac{2}{3} \frac{\partial U_k}{\partial x_k} \delta_{ij} \right) + \rho f_i^e \quad . \tag{4.18}$$

By subtracting the continuity equation (4.10) multiplied by $\boldsymbol{U}$ from (4.17), the equivalent, non-conservative form is obtained

$$\frac{\mathrm{D} U_i}{\mathrm{D} t} \equiv \rho \frac{\partial U_i}{\partial t} + \rho U_j \frac{\partial U_i}{\partial x_j} = -\frac{\partial p}{\partial x_i} + \frac{\partial \tau_{ij}}{\partial x_j} + \rho f_i^e \quad , \tag{4.19}$$

where the material, or convective derivative $^{\mathrm{D}}/_{\mathrm{D}t}$ has been introduced.

For flows with constant density and viscosity, applying the divergence free condition (4.12), the momentum equation reduces to

$$\frac{\partial U_i}{\partial t} + U_j \frac{\partial U_i}{\partial x_j} = -\frac{1}{\rho}\frac{\partial p}{\partial x_i} + \nu \frac{\partial^2 U_i}{\partial x_j \partial x_j} + f_i^e \quad , \tag{4.20}$$

where $\nu = \mu/\rho$ is the kinematic viscosity (m^2/s).

For an ideal, compressible, inviscid fluid, the Euler equation of motion is obtained:

$$\frac{\partial \rho U_i}{\partial t} + \frac{\partial \rho U_j U_i}{\partial x_j} = -\frac{\partial p}{\partial x_i} + \rho f_i^e \quad . \tag{4.21}$$

This equation further simplifies for incompressible flows to

$$\frac{\partial U_i}{\partial t} + U_j \frac{\partial U_i}{\partial x_j} = -\frac{1}{\rho}\frac{\partial p}{\partial x_i} + f_i^e \quad . \tag{4.22}$$

4.6 Species Mass Conservation

In particular for reactive flows, species transport is of importance as the chemical reactions introduce sinks and sources for the species in the flow field. But also pure mixing problems, where inhomogeneous concentrations are subject to convection and to diffusion, require the solution of the species mass equations. Possible applications could be the analysis of an accident where a toxin was released into the sea and one wishes to predict its spreading.

The mass of species α per unit volume, ρY_α, is the conserved variable $\mathcal{U}$ for the species mass conservation equation. The convective flux function is straight forward to obtain and the diffusive flux is given by the *diffusion velocity* $\boldsymbol{V}^\alpha$ of species α:

$$F^C_{\alpha,i} = \rho Y_\alpha U_i \quad \text{and} \tag{4.23}$$

$$F^D_{\alpha,i} = \rho Y_\alpha V_i^\alpha \quad . \tag{4.24}$$

Note that in order to preserve mass the following condition must hold for the diffusion velocities

$$\sum_{\alpha=1}^{N_s} Y_\alpha V_{\alpha,i} = 0 \quad . \tag{4.25}$$

In order to determine the exact diffusion velocity $\boldsymbol{V}_\alpha$ it is required to

solve the system [61]

$$\begin{aligned}\frac{\partial X_\alpha}{\partial x_i} = &\sum_{\beta=1}^{N_s} \frac{X_\alpha X_\beta}{\Gamma_{\alpha\beta}} \left(V_{\beta,i} - V_{\alpha,i}\right) + \left(Y_\alpha - X_\alpha\right) \frac{1}{p} \frac{\partial p}{\partial x_i} \\ &+ \frac{\rho}{p} \sum_{\beta=1}^{N_s} Y_\alpha Y_\beta \left(f^e_{\alpha,i} - f^e_{\beta,i}\right) \quad ,\end{aligned} \tag{4.26}$$

$\Gamma_{\alpha\beta} = \Gamma_{\beta\alpha}$ being the binary diffusion coefficient of species α into species β, while $\boldsymbol{f}^e_\alpha$ is the volume force acting on species α. This formulation excludes mass diffusion due to temperature gradients, the Soret effect. The derivation of above system of equations is outside the scope of this work, in particular as it is hardly ever used in simulation tools for turbulent reactive flows. This potentially very large system of equations of size N_s^2 needs to be solved for every time-step in every grid cell, making the simulation computationally highly expensive. The interested reader is referred to Kuo [35].

Often times, however, it is justified to assume a single diffusivity Γ_α of species α into the mixture. This is accomplished using a simplified diffusion law based on Fick's law, resulting in the diffusion velocity [61]

$$V_i^\alpha Y_\alpha = -\Gamma_\alpha \frac{\partial Y_\alpha}{\partial x_i} \quad . \tag{4.27}$$

The remaining volume source term is due to chemical reaction, $\dot{\omega}_\alpha$. For the purpose of this discussion it is left unspecified, but will later be subjected to closer inspection in Section 5. Note that the same condition as for the diffusion velocity must also apply to the chemical source term:

$$\sum_{\alpha=1}^{N_s} \dot{\omega}_\alpha = 0 \quad . \tag{4.28}$$

Inserting above definitions into (4.6) results in the conservation equation for species mass subject to Fickian diffusion

$$\frac{\partial \rho Y_\alpha}{\partial t} + \frac{\partial \rho U_i Y_\alpha}{\partial x_i} = \frac{\partial}{\partial x_i} \left(\rho \Gamma_\alpha \frac{\partial Y_\alpha}{\partial x_i}\right) + \rho \dot{\omega}_\alpha \quad . \tag{4.29}$$

4.7 Energy Conservation

The conserved quantity related to energy is the total energy $e_t = e + {}^1\!/_2 U_i U_i$. Changes in the total energy of a system must be due to work introduced or

removed by forces acting on the system and due to heat that is entering or draining.

Using $\mathcal{U} = \rho e_t$ and the fact that by definition the velocity is not subject to diffusion, the convective and diffusive fluxes for the energy conservation law are given by

$$f_i^C = \rho U_i e_t \quad \text{and} \tag{4.30}$$

$$f_i^D = -\lambda \frac{\partial T}{\partial x_i} + \rho \sum_{\alpha=1}^{N_s} h_s Y_\alpha V_{\alpha,i} \quad , \tag{4.31}$$

λ being the thermal conductivity coefficient. The second term accounts for the diffusion of species with different enthalpies and only applies to multicomponent fluids [61]. Note that applying Fourier's law to determine the heat diffusion flux is only a model making many assumptions.

As mentioned above, the volume source Q^V is split into the work of the volume forces plus the heat sources $\dot{Q}$, e.g. radiation or a spark plug, resulting in

$$Q^V = \rho Y_\alpha f_i^e \left(U_i + V_{\alpha,i}\right) + \dot{Q} \quad . \tag{4.32}$$

Note that in a multicomponent mixture one has to take into account the diffusion velocities unless Fickian diffusion is assumed. Excluding external heat sources at the surface, the volume source term is given by the work of the internal forces, i.e.

$$Q_i^S = \sigma_{ij} U_j = -pU_i + \tau_{ij} U_j \quad . \tag{4.33}$$

Substituting above definitions for the conserved variable, the convective and diffusive fluxes and the volume and surface sources into (4.6) gives for the energy conservation equation

$$\begin{aligned} \frac{\partial \rho e_t}{\partial t} + \frac{\partial \rho U_i e_t}{\partial x_i} =& \frac{\partial}{\partial x_i}\left(\lambda \frac{\partial T}{\partial x_i}\right) - \frac{\partial}{\partial x_i}\left(\rho \sum_{\alpha=1}^{N_s} h_\alpha Y_\alpha V_{\alpha,i}\right) \\ & - \frac{\partial U_i p}{\partial x_i} + \frac{\partial \tau_{ij} U_j}{\partial x_i} + \rho \sum_{\alpha=1}^{N_s} Y_\alpha f_i^e \left(U_i + V_{\alpha,i}\right) + \dot{Q} \quad . \end{aligned} \tag{4.34}$$

This equation can be transformed into transport equations for the total enthalpy h_t, the inner energy e and enthalpy h, sensible inner energy e_s and sensible enthalpy h_s, total non-chemical energy E and enthalpy H, as well as for the temperature T. Refer to [61] for all the different forms of the energy transport equation.

5 Reaction Chemistry

In this section the basics of the chemical reaction kinetics are covered. The discussion will largely follow the description given by Fox [17], although the notation is adapted to be consistent with the conventions in this work.

5.1 Chemical Source Term

Conversion of the fuel and oxidiser to the combustion products is described by a set of N_r elementary chemical reactions of N_s chemical species with symbols $\mathcal{M}_\alpha$ [17], i.e. by

$$\sum_{\alpha=1}^{N_s} \upsilon'_{\alpha,i} \mathcal{M}_\alpha \underset{k_i^r}{\overset{k_i^f}{\rightleftharpoons}} \sum_{\alpha=1}^{N_s} \upsilon''_{\alpha,i} \mathcal{M}_\alpha \quad \text{for } i \in 1, \ldots, N_r, \tag{5.1}$$

with the integer stoichiometric coefficients $\upsilon'_{\alpha,i}$ and $\upsilon''_{\alpha,i}$ for the forward and reverse reactions, respectively, and the forward and reverse reaction rate constants k_i^f and k_i^r. Note that the dimension of the reaction rate constants depends on the order of the reaction. Further, non-elementary reactions can also be described by (5.1) if non-integer stoichiometric coefficients are allowed.

The reaction source term $\dot{\omega}_\alpha$ from the species mass conservation equation (4.29) is consequently given by

$$\dot{\omega}_\alpha(\boldsymbol{\phi}) \equiv \frac{W_\alpha}{\rho} \Upsilon_{\alpha i} R_i(\boldsymbol{\phi}) \quad , \tag{5.2}$$

$\boldsymbol{\Upsilon}$ being the reaction coefficient matrix with elements $\Upsilon_{\alpha i} = \upsilon''_{\alpha,i} - \upsilon'_{\alpha,i}$ and $\boldsymbol{R}(\boldsymbol{\phi})$ the reaction rate vector

$$R_i(\boldsymbol{\phi}) = k_i^f(T) \prod_{\alpha=1}^{N_s} C_\alpha^{\upsilon'_{\alpha,i}} - k_i^r(T) \prod_{\alpha=1}^{N_s} C_\alpha^{\upsilon''_{\alpha,i}} \quad . \tag{5.3}$$

The vector $\boldsymbol{\phi}$ is introduced as a shorthand notation for all scalars. Here, it would be the vector $[Y_1, Y_2, \ldots, Y_{N_s}, T]^T$. In the following discussion it is assumed that all elements $R_i(\boldsymbol{\phi})$ are linearly independent which is almost always the case [17]. In the case of two or more elements being linearly dependent, the corresponding columns of $\boldsymbol{\Upsilon}$ could be replaced by a single column. As a consequence of mass conservation it holds that [61]

$$\begin{aligned} &\sum_{\alpha=1}^{N_s} \upsilon^f_{\alpha,i} W_\alpha = \sum_{\alpha=1}^{N_s} \upsilon^r_{\alpha,i} W_\alpha \qquad \text{or, alternatively} \\ &\sum_{\alpha=1}^{N_s} \Upsilon_{\alpha i} W_\alpha = 0 \qquad\qquad \forall i \in \{1, \ldots, N_r\} \quad . \end{aligned} \tag{5.4}$$

The forward reaction rates are commonly modelled by the Arrhenius law

$$k^f_i(T) = A_i T^{\beta_i} \exp\left(-\frac{E_i}{R_u T}\right) \quad , \tag{5.5}$$

where the preexponential factor A_i, the temperature exponent β_i and the activation energy E_i are obtained from reaction mechanism tabulations, such as GRI-3.0. The reverse reaction rate is obtained using the relation

$$k^r_i(T) = \frac{k^f_i(T)}{K_i(T)} \quad , \tag{5.6}$$

the equilibrium constant

$$K_i = \left(\frac{p_a}{R_u T}\right)^{\sum_{\alpha=1}^{N_s} \Upsilon_{\alpha i}} \exp\left(\frac{\Delta S^0_i}{R_u} - \frac{\Delta H^0_i}{R_u T}\right) \quad , \tag{5.7}$$

being derived from thermodynamic considerations using Gibbs free energies [61], where $p_a = 1\,\text{bar}$ and ΔH^0_i and ΔS^0_i are the enthalpy and entropy changes due to reaction i, respectively, typically obtained from chemical tabulations.

Chemical elements are preserved for elementary reactions. This is easy to see when one considers that in normal chemical processes no fission or fusion is occurring. This principle can be expressed through the element matrix $\boldsymbol{\Lambda}$ of size $N_e \times N_s$, N_e being the number of elements in the chemical system. Each row corresponds to a single element and every column to a chemical species. The integer entries $\Lambda_{e\alpha}$ give the multiplicity of element e

in species α. The element conservation can be expressed through [17]

$$\begin{aligned} \sum_{\alpha=1}^{N_s} \Lambda_{e\alpha} \frac{\rho}{W_\alpha} \dot{\omega}_\alpha = 0 \quad \forall e \in \{1, \ldots, N_e\} \quad \text{or} \\ \sum_{\alpha=1}^{N_s} \Lambda_{e\alpha} \Upsilon_{\alpha i} = 0 \quad \forall (e, i) \in \{1, \ldots, N_e\} \times \{1, \ldots, N_r\} \quad . \end{aligned} \tag{5.8}$$

The element matrix being constant in space and time, (5.8) can be applied to the species mass conservation equation (4.29) to eliminate the chemical source term $\dot{\omega}_\alpha$ from $N_c = N_s - N_\Upsilon$ of the N_s equations [17], where $N_\Upsilon = \text{rank}(\boldsymbol{\Upsilon})$ is the rank of the reaction coefficient matrix. These equations become then transport equations of *conserved* scalars.

Extending above concepts for non-elementary reactions is possible, if the requirement for integer reaction coefficients $\upsilon^f_{\alpha,i}$ and $\upsilon^r_{\alpha,i}$ is dropped. Although the element conservation (5.8) no longer holds, the elimination of source terms from the species mass conservation (4.29) is still possible. A suitable transformation matrix $\mathbf{M}$ can be found through the singular value decomposition (SVD) of $\boldsymbol{\Upsilon} = \mathbf{M}^T \boldsymbol{\Sigma} \mathbf{V}^T$, where $\mathbf{M}$ and $\mathbf{V}$ are orthogonal matrices and $\boldsymbol{\Sigma}$ is the diagonal matrix consisting of the $\min(N_r, N_s)$ non-negative singular values. The rows in $\mathbf{M}$ corresponding to the $N_\Upsilon \leqslant \min(N_r, N_s)$ non-zero singular values span the sub-space of the reactive scalars $\boldsymbol{\phi}_r$, the others the conserved-scalars sub-space $\boldsymbol{\phi}_c$.

This transformation can greatly simplify the chemical source terms in the species mass conservation equation (4.29). However, it does so at the expense of potentially complicating the transformed species diffusivity tensor $\mathbf{M}\,\mathbf{diag}\,(\Gamma_1, \ldots, \Gamma_{N_s})\,\mathbf{M}^T$. Only in the case of equal diffusivities the diagonal form of the species diffusivity tensor is retained; a justified assumption for highly turbulent flows as the turbulent mixing will often control the molecular diffusion terms under such conditions [17].

5.2 Chemical Time Scales

It is conventional to define the chemical time scales in terms of the N_s Eigenvalues μ_i of the Jacobian matrix $\mathbf{J}$ of the chemical source term for the molar concentrations

$$J_{\alpha\beta}(\boldsymbol{\phi}) \equiv \frac{\rho}{W_\alpha} \frac{\partial \dot{\omega}_\alpha(\boldsymbol{\phi})}{\partial Y_\beta} \equiv \Upsilon_{\alpha i} \frac{\partial R_i(\boldsymbol{\phi})}{\partial Y_\beta} \quad . \tag{5.9}$$

The chemical time scales τ_α are then given by the inverse of the magnitude of the Eigenvalues of $\mathbf{J}$:

$$\tau_i \equiv \frac{1}{\|\mu_i\|} \quad . \tag{5.10}$$

Consequently, large Eigenvalues will result in small time-scales, i.e. fast reactions, while a small Eigenvalue implies a large time-scale and slow reaction. It is of great importance that these time scales typically span across several orders of magnitudes [17], making the problem very stiff and particularly difficult to solve.

The N_c Eigenvalues of $\mathbf{J}$ which are null correspond to the conserved scalars $\boldsymbol{\phi}_c$ and no closure for the chemical source term needs to be provided for them. Hence, the discussion can be limited to the N_Υ finite chemical time scales.

5.3 Mixture Fraction Vector

It is often possible to assume equal diffusivities in high-Reynolds-number flows, leading to the simplified species mass transport equation for conserved scalars

$$\frac{\partial \rho \phi_{c,\alpha}}{\partial t} + \frac{\partial \rho U_i \phi_{c,\alpha}}{\partial x_i} = \frac{\partial}{\partial x_i}\left(\rho \Gamma \frac{\partial \phi_{c,\alpha}}{\partial x_i}\right) \quad . \tag{5.11}$$

The solutions of these linear equations are solely determined by the initial and boundary conditions. Provided that the initial conditions in the domain are spatially uniform (i.e. $\boldsymbol{\phi}_c(\boldsymbol{x}, 0) = \boldsymbol{\phi}_c^{(0)}$) and that the N_{in} inflow streams are both uniform in space and constant in time so that $\boldsymbol{\phi}_c(\boldsymbol{x} \in \partial\Omega_j, t) = \boldsymbol{\phi}_c^{(j)}$ for all $j \in \{1, \ldots, N_{\text{in}}\}$, the principle of superposition [17] can be applied

$$\phi_{c,\alpha}(\boldsymbol{x}, t) = \phi_{c,\alpha}^{(j)} w_j(\boldsymbol{x}, t) \quad , \tag{5.12}$$

where $\boldsymbol{w}$ is a coefficient vector of length $N_{\text{in}} + 1$ that follows the transport equation (5.11) for the conserved scalars

$$\frac{\partial \rho w_\alpha}{\partial t} + \frac{\partial \rho U_i w_\alpha}{\partial x_i} = \frac{\partial}{\partial x_i}\left(\rho \Gamma \frac{\partial w_\alpha}{\partial x_i}\right) \quad , \tag{5.13}$$

subject to the following initial and boundary conditions:

$$w_i(\boldsymbol{x}, 0) = \begin{cases} 1 & \text{if } i = 0 \\ 0 & \text{else} \end{cases} \quad \forall i \in \{0, \ldots, N_{\text{in}}\} \quad \text{and} \tag{5.14}$$

$$w_i(\boldsymbol{x} \in \partial\Omega_j, t) = \begin{cases} 0 & \text{if } i = 0 \\ 1 & \text{if } i = j \\ 0 & \text{else} \end{cases} \quad \forall (i,j) \in \{0, \ldots, N_{\text{in}}\} \times \{1, \ldots, N_{\text{in}}\} \quad . \tag{5.15}$$

This system of equations is over-determined since $\sum_{i=0}^{N_{\text{in}}} w_i = 1$, and consequently one of the weights can be eliminated by forming centralised vectors of conserved scalars by subtracting any of the $N_{\text{in}} + 1$ vectors $\boldsymbol{\phi}_c^{(j)}$ from the others, here conveniently chosen to be $\boldsymbol{\phi}_c^{(0)}$: $\boldsymbol{\varphi}_c^{(j)} = \boldsymbol{\phi}_c^{(j)} - \boldsymbol{\phi}_c^{(0)}$. Further elements from the coefficient vector $\boldsymbol{w}$ can be removed by dropping linearly dependent vectors $\boldsymbol{\phi}_c^{(j)}$. Defining the matrix

$$\boldsymbol{\Phi}_c^{(0)} \equiv \left[\boldsymbol{\varphi}_c^{(1)} \ldots \boldsymbol{\varphi}_c^{(N_{\text{in}})}\right] \quad ,$$

the minimum number of scalar transport equations required to describe the evolution of the conserved scalars is hence defined by the rank of the matrix $\boldsymbol{\Phi}_c^{(0)}$

$$N_{\Phi_c^{(0)}} \equiv \text{rank}\left(\boldsymbol{\Phi}_c^{(0)}\right) \leqslant \min(N_c, N_{\text{in}}) \quad .$$

This means that the conserved scalar sub-space $\boldsymbol{\varphi}_c$ can be further split into $N_{\Phi_c^{(0)}}$ components $\boldsymbol{\varphi}_{cv}$ that evolve in space and time and $N_c - N_{\Phi_c^{(0)}}$ constant or uniform components $\boldsymbol{\varphi}_{cc}$. This partitioning can be obtained through the SVD of $\boldsymbol{\Phi}_c^{(0)}$ [17]:

$$\boldsymbol{\Phi}_c^{(0)} = \mathbf{U}^{(0)} \boldsymbol{\Sigma}^{(0)} \mathbf{V}^{(0)T} \quad .$$

This decomposition can be used to define

$$\boldsymbol{\Phi}_{cv}^{(0)} = \mathbf{U}_v^{(0)T} \boldsymbol{\Phi}_c^{(0)} \quad , \tag{5.16}$$

where $\mathbf{U}_v^{(0)}$ is composed of the first $N_{\Phi_c^{(0)}}$ columns of $\mathbf{U}^{(0)}$ which correspond to the non-zero singular values in descending order. Applying the linear transformation (5.16) to the transport equation of the coefficients vector $\boldsymbol{w}$, (5.13), the conserved variable scalar vector follows

$$\frac{\partial \rho \varphi_{cv,\alpha}}{\partial t} + \frac{\partial \rho U_j \varphi_{cv,\alpha}}{\partial x_j} = \frac{\partial}{\partial x_j}\left(\rho \Gamma \frac{\partial \varphi_{cv,\alpha}}{\partial x_j}\right) \quad , \tag{5.17}$$

subject to $\varphi_{cv,\alpha}(\boldsymbol{x},0) = 0$ and $\varphi_{cv,\alpha}(\boldsymbol{x} \in \partial\Omega_j, t) = \Phi^{(0)}_{cv,\alpha j}$ for all $\alpha \in \left\{1,\ldots,N_{\Phi^{(0)}_c}\right\}$ and $j \in \{1,\ldots,N_{\text{in}}\}$.

It follows that the complete flow can be described by N_γ reactive and $N_{\Phi^{(0)}_c}$ conserved, variable scalars. In the case of stationary flows, the initial condition vector $\boldsymbol{\phi}^{(0)}$ can be replaced by any of the inflow boundary condition vectors $\boldsymbol{\phi}^{(j)}$ for any $j \in \{1,\ldots,N_{\text{in}}\}$. If additionally $N_{\text{in}} = N_{\Phi^{(0)}_c}$, then $N_{\Phi^{(j)}_c} = N_{\text{in}} - 1$ and consequently one conserved, variable scalar will be required.

5.4 The Mixture Fraction and Reaction Progress Vectors

In many cases it is possible to replace $\boldsymbol{\varphi}_{cv}$ by a mixture fraction vector $\boldsymbol{z}$ with N_z components, bounded by $N_{\Phi^{(0)}_c} \leqslant N_z \leqslant N_{\text{in}}$. Its components are all non-negative and their sum is less than or equal to unity. Note, however, that using a mixture fraction vector only offers an advantage if $N_z = N_{\Phi^{(0)}_c}$, since otherwise directly using the conserved, variable scalars is more interesting due to the reduced number of equations that need to be solved. In this case, it is clear that the obvious choice for the mixture fraction vector $\boldsymbol{z}$ is the coefficient vector $\boldsymbol{w}$ defined in (5.13). The use of a mixture fraction vector is subject to the condition that the reacting scalars $\boldsymbol{\phi}_r$ must form a linear mixture describable by the mixture fraction vector. Whether this condition is fulfilled is not always self-evident, and a methodology of establishing a mixture fraction vector in terms of a linear mixture basis for arbitrary inflow and initial conditions is given by Fox [17, Sec. 5.3.2]. In essence, one has to find a matrix $\mathbf{B}^{(k)}$ that relates the linearly dependent columns to the linearly independent columns of the matrix

$$\boldsymbol{\Phi}^{(k)}_{cv} = \left[\boldsymbol{\varphi}^{(0)}_{cv} \ldots \boldsymbol{\varphi}^{(k-1)}_{cv} \boldsymbol{\varphi}^{(k+1)}_{cv} \ldots \boldsymbol{\varphi}^{(N_{\text{in}})}_{cv}\right] \quad ,$$

where $\boldsymbol{\varphi}^{(j)}_{cv} = \boldsymbol{\phi}^{(j)}_{cv} - \boldsymbol{\phi}^{(k)}_{cv}$ for some $k \in \{0,\ldots,N_{\text{in}}\}$. All components of $\mathbf{B}^{(k)}$ must be non-negative and it must hold that the last $N_{\text{in}} - N_z$ initial and boundary conditions for the reactive scalars $\boldsymbol{\varphi}^{(j)}_r$ must be a linear combination of the first N_z initial and boundary conditions as defined by $\mathbf{B}^{(k)}$:

$$\varphi^{(j)}_{r,\alpha} = B^{(k)}_{i,j-N_z} \varphi^{(i)}_{r,\alpha} \quad \forall j \in \{N_z+1,\ldots,N_{\text{in}}\} \quad .$$

In principle, all $N_{\text{in}} + 1$ reference vectors and all possible combinations of linearly independent initial and boundary conditions must be searched to find a valid linear mixture fraction basis, which is tedious at best. In practice,

however, the number of inflow streams with differing compositions is usually limited to one or two, making this a very simple task.

Renumbering the initial and inflow conditions such that the N_z first vectors form the mixture fraction basis, and using the N_z first initial and inflow conditions for the reactive scalars to define the linear transformation matrix $\mathbf{\Phi}_{\text{rp}} = \left[\boldsymbol{\varphi}_r^{(1)} \ldots \boldsymbol{\varphi}_r^{(N_z)}\right]$, the reaction progress vector $\boldsymbol{\varphi}_{\text{rp}}$ is given by

$$\varphi_{rp,\alpha} = \varphi_{r,\alpha} - \Phi_{rp,\alpha i} z_i \tag{5.18}$$

with the particular property of being null for all initial and inflow conditions and in the limit of all reaction rate constants being zero. The flow can now be fully described by both, the reaction progress vector $\boldsymbol{\varphi}_{\text{rp}}$ and the mixture fraction vector z.

In the limit of equilibrium chemistry, where all relevant chemical time scales τ_α are much smaller than the flow and scalar mixing time scales, the transport equation for the reaction progress vector reduces to an ordinary differential equation with only the transformed reaction source term on the right hand side, depending only on the vector itself and the mixture fraction vector. Since local equilibrium is assumed, the reaction progress vector can now be set equal to the equilibrium solution $\boldsymbol{\varphi}_{\text{eq}}$ of the system of ordinary differential equations,

$$\varphi_{rp,\alpha}(\boldsymbol{x}, t) = \varphi_{eq,\alpha}\left(z(\boldsymbol{x}, t)\right) \quad ,$$

the only dependence being the mixture fraction vector at the given point in space and time. This simplifies the numerical simulation, as only the transport equation related to the mixture fraction vector must be solved which does not include any source terms. The equilibrium solutions $\boldsymbol{\varphi}_{\text{eq}}$ are initial value problems that can be solved and tabulated independently of the flow simulation, e.g. in a preprocessing step. The modelling of turbulent combustion will be further expanded on in Section 8.

6 Reynolds Averaged Equations

When conducting simulations or experiments, one is often more interested in mean quantities than in instantaneous, heavily fluctuating results. There are many ways to define such means, e.g. for stationary problems by averaging a given signal $U(t)$ over time:

$$\langle U(\boldsymbol{x})\rangle_T = \lim_{T\to\infty} \frac{1}{T} \int_t^{t+T} U(\boldsymbol{x}, t')\mathrm{d}t' \quad .$$

For spatially homogeneous problems, volume averaging is the appropriate choice

$$\langle U(t)\rangle_V = \lim_{V\to\infty} \frac{1}{V} \iiint_V U(\boldsymbol{x}, t)\mathrm{d}\boldsymbol{X} \quad .$$

The most general averaging method is the so called *ensemble* averaging. Consider an experiment that is repeated N times with the same initial and boundary conditions, and for each a time-dependent signal is recorded. To obtain the mean signal, the averaging operation is now performed across these N signals

$$\langle U(\boldsymbol{x}, t)\rangle_E = \lim_{N\to\infty} \frac{1}{N} \sum_{i=1}^{N} U_i(\boldsymbol{x}, t) \quad . \tag{6.1}$$

If all three methods are interchangeable, i.e. the signal is both stationary and homogeneous, the *ergodic* hypothesis applies and the short-hand notation $\langle U\rangle$ will be used. The fluctuating signal can then be split into a mean and a fluctuating part

$$U(t) = \langle U\rangle + u'(t) \quad , \tag{6.2}$$

where the following properties apply

$$\langle\langle U\rangle\rangle = \langle U\rangle \quad , \tag{6.3}$$
$$\langle UV\rangle = \langle U\rangle\langle V\rangle + \langle u'v'\rangle \quad \text{and} \tag{6.4}$$
$$\langle u'\rangle = 0 \quad . \tag{6.5}$$

This method is called *Reynolds averaging* and *decomposition*, respectively. It is also commonly referred to as *volume averaging*. This name conveys the meaning that each measurement has the same importance when taken from a given sampling volume. As an example, this is an appropriate way to quantify the mean volume fraction of tiny, uniformly sized glass beads used to seed the flow during an experiment.

If, however, the relative mass of the samples is of importance, such as for the mean velocity in a variable density flow, one has to use *mass-weighted* or *Favre* averaging:

$$\widetilde{U} = \frac{\langle \rho U(t)\rangle}{\langle \rho\rangle} \quad . \tag{6.6}$$

Similar to (6.2) the instantaneous signal can again be decomposed into a mean and a fluctuating part

$$U(t) = \widetilde{U} + u''(t) \quad , \tag{6.7}$$

subject to the same properties as the Reynolds decomposition:

$$\widetilde{\widetilde{U}} = \widetilde{U} \quad , \tag{6.8}$$
$$\widetilde{UV} = \widetilde{U}\widetilde{V} + \widetilde{u''v''} \quad \text{and} \tag{6.9}$$
$$\widetilde{u''} = 0 \quad . \tag{6.10}$$

6.1 Derivation of the Reynolds Averaged Equations

Applying Reynolds averaging to equations (4.10), (4.18), (4.34) and (4.29), excluding volume forces and molecular effects (e.g. heat conduction) and assuming equal diffusivities, results in a system of equations that is referred

to as the Reynolds averaged equations for compressible flows:

$$\frac{\partial \langle\rho\rangle}{\partial t} + \frac{\partial \langle\rho\rangle \widetilde{U}_i}{\partial x_i} = 0 \quad , \tag{6.11a}$$

$$\frac{\partial \langle\rho\rangle \widetilde{U}_i}{\partial t} + \frac{\partial \langle\rho\rangle \widetilde{U}_j\widetilde{U}_i + \langle p\rangle \delta_{ij} - \langle\tau_{ij}\rangle}{\partial x_j} = -\frac{\partial \langle\rho\rangle \widetilde{u_i''u_j''}}{\partial x_j} \quad , \tag{6.11b}$$

$$\begin{aligned}\frac{\partial \langle\rho\rangle \widetilde{e}_t}{\partial t} + \frac{\partial \langle\rho\rangle \widetilde{U}_i\widetilde{e_t} - \widetilde{U}_i\langle p\rangle - \widetilde{U}_j\langle\tau_{ij}\rangle}{\partial x_i} = \\ \frac{\partial \left\langle p'u_i''\right\rangle - \langle\rho\rangle \widetilde{e_t''u_i''}}{\partial x_i} + \frac{\partial \left\langle\tau_{ij}u_j''\right\rangle}{\partial x_i} + \widetilde{\dot{Q}}\end{aligned} \tag{6.11c}$$

and

$$\begin{aligned}\frac{\partial \langle\rho\rangle \widetilde{Y}_\alpha}{\partial t} + \frac{\partial \langle\rho\rangle \widetilde{U}_i\widetilde{Y}_\alpha}{\partial x_i} - \frac{\partial}{\partial x_i}\left(\langle\rho\rangle \Gamma\frac{\partial\widetilde{Y}_\alpha}{\partial x_i}\right) = \\ -\frac{\partial \langle\rho\rangle \widetilde{Y_\alpha''u_i''}}{\partial x_i} + \langle\rho\rangle \widetilde{\dot{\omega}}_\alpha \quad .\end{aligned} \tag{6.11d}$$

All the equations have been rearranged such that the closed terms are on the left hand side. The terms on the right hand side either represent higher order statistics that are unknown (e.g. the six so called *Reynolds stress* tensor components $\widetilde{u_i''u_j''}$ cannot be computed from the mean velocity $\widetilde{\boldsymbol{U}}$) or are source terms for the species mass fraction and the energy that are highly non-linear, i.e. $\widetilde{\dot{\omega}_\alpha(\boldsymbol{\phi})} \neq \dot{\omega}_\alpha(\widetilde{\boldsymbol{\phi}})$.

By multiplying the instantaneous momentum equation (4.18) with u_j'', averaging and some rearrangement, the six Reynolds stress transport equations are obtained [84], i.e.

$$\begin{aligned}\frac{\partial \langle\rho\rangle \widetilde{u_i''u_j''}}{\partial t} + \frac{\partial \langle\rho\rangle \widetilde{U}_k\widetilde{u_i''u_j''}}{\partial x_k} - \mathcal{P}_{ij} = -\frac{\partial \mathcal{T}_{kij}}{\partial x_k} + \Pi_{ij} - \varepsilon_{ij} \\ + \langle u_i''\rangle \frac{\partial \langle p\rangle}{\partial x_j} + \left\langle u_j''\right\rangle \frac{\partial \langle p\rangle}{\partial x_i} \quad ,\end{aligned} \tag{6.12}$$

where

$$\mathcal{P}_{ij} = -\langle\rho\rangle\,\widetilde{u_i'' u_k''}\frac{\partial \widetilde{U}_j}{\partial x_k} - \langle\rho\rangle\,\widetilde{u_j'' u_k''}\frac{\partial \widetilde{U}_i}{\partial x_k} \quad , \tag{6.13}$$

$$\begin{aligned}\mathcal{T}_{kij} = \langle\rho\rangle\,\widetilde{u_i'' u_j'' u_k''} + \langle p' u_i''\rangle\,\delta_{jk} + \langle p' u_j''\rangle\,\delta_{ik} \\ - \langle\tau_{kj} u_i''\rangle - \langle\tau_{ki} u_j''\rangle \quad ,\end{aligned} \tag{6.14}$$

$$\Pi_{ij} = \left\langle p'\frac{\partial u_i''}{\partial x_j}\right\rangle + \left\langle p'\frac{\partial u_j''}{\partial x_k}\right\rangle \tag{6.15}$$

and

$$\varepsilon_{ij} = \left\langle \tau_{kj}\frac{\partial u_i''}{\partial x_k}\right\rangle + \left\langle \tau_{ki}\frac{\partial u_j''}{\partial x_k}\right\rangle \tag{6.16}$$

are the Reynolds stress production, Reynolds stress flux, the pressure-rate of strain and the dissipation tensors, respectively. All, except the production term, are in unclosed form. The process of deriving equations for these terms could be repeated in a similar fashion as for the Reynolds stress terms, but new unclosed, even higher order terms would appear. There is no level of statistics at which this series will converge and a closed system of equations is obtained. This is referred to as the *closure problem* of turbulence modelling, and hence the need for modelling approaches which try to approximate these unclosed terms at various levels of closure using lower order terms.

As a notational convenience, the normal components of the Reynolds stress tensor are quantified as their standard deviation, denoted by

$$u_i' = \sqrt{\widetilde{u_i''^2}} \quad .$$

Commonly, this is also referred to as the root-mean-square (RMS) of the fluctuating velocities. The conflicting notation with the fluctuating component of the Reynolds stress decomposition is not a real problem, as the meaning is usually clear from the context.

6.2 Turbulence Modelling

Modelling the Reynolds stresses is a rich research topic in its own right. Only the most important concepts will be covered here, with the main focus on the topics relevant to this work. Most popular models fall into

one of two large families of turbulence models. The so called *eddy viscosity models* attempt to describe the turbulent stress tensor in terms of the mean velocity gradients and an *eddy viscosity* μ_T, in analogy with the molecular stress tensor, making a Boussinesq approximation. These models take the form

$$\langle\rho\rangle \widetilde{u_i'' u_j''} = -2\mu_T \left(\widetilde{S}_{ij} - \frac{1}{3}\frac{\partial \widetilde{U}_k}{\partial x_k}\delta_{ij} \right) + \frac{2}{3}\langle\rho\rangle\, k\delta_{ij} \tag{6.17}$$

where k is the turbulent kinetic energy (TKE) defined by

$$k = \frac{1}{2}\widetilde{u_i'' u_i''} \tag{6.18}$$

and $\widetilde{\mathbf{S}}$ is the mean strain rate tensor

$$\widetilde{S_{ij}} = \frac{1}{2}\left(\frac{\partial \widetilde{U}_i}{\partial x_j} + \frac{\partial \widetilde{U}_j}{\partial x_i} \right) \quad . \tag{6.19}$$

The transport equation for the TKE is obtained by taking one half of the trace of the Reynolds stress transport equation (6.12) [84]

$$\begin{aligned} \frac{\partial \langle\rho\rangle\, k}{\partial t} + \frac{\partial \langle\rho\rangle \widetilde{U}_i k}{\partial x_i} + \langle\rho\rangle \widetilde{u_i'' u_j''}\frac{\partial \widetilde{U}_j}{\partial x_i} = \\ \frac{\partial}{\partial x_j}\left(\langle \tau_{ji} u_i'' \rangle - \frac{\langle\rho\rangle \widetilde{u_i'' u_i'' u_j''}}{2} - \langle p' u_j'' \rangle \right) \\ - \varepsilon + \langle u_i'' \rangle \frac{\partial \langle p \rangle}{\partial x_i} + \left\langle p' \frac{\partial u_i''}{\partial x_i} \right\rangle \end{aligned} \tag{6.20}$$

The turbulent dissipation

$$\varepsilon = \left\langle \tau_{ji} \frac{\partial u_i''}{\partial x_j} \right\rangle \tag{6.21}$$

is defined as one half of the trace of the dissipation tensor (6.16) Again, all terms on the right-hand side of (6.20) require modelling.

Often, the *turbulent transport* term is approximated by a gradient diffusion ansatz and the *pressure diffusion* term is reasonably small compared to the other terms for simple flows with low compressibility as indicated by DNS data by Mansour et al. [42]. It is usual to model these two terms together using a gradient diffusion approximation, resulting in

$$\frac{\langle\rho\rangle \widetilde{u_i'' u_i'' u_j''}}{2} + \langle p' u_j'' \rangle = -\frac{\mu_T}{\sigma_k}\frac{\partial k}{\partial x_j} \quad . \tag{6.22}$$

Here, σ_k is the turbulent Prandtl number, usually assumed to be unity.

Little is known about the *pressure-dilation* term $\langle p' \partial u_i''/\partial x_j \rangle$, and for low-Mach number flows it is often ignored, as is done for the *pressure work* term $\left\langle u_i'' \right\rangle \partial\langle p \rangle/\partial x_i$, or $\left\langle u_i'' \right\rangle \partial\langle p \rangle/\partial x_j + \left\langle u_j'' \right\rangle \partial\langle p \rangle/\partial x_i$ in the Reynolds-stress equation [84].

The other class of turbulence models are the so called *Reynolds stress* models which directly solve the six transport equations (6.12), using models to close the turbulent flux, pressure rate of strain and the dissipation tensor.

6.2.1 Eddy Viscosity Models

The main task for eddy viscosity models is to provide an expression for the turbulent viscosity μ_T. The simplest models try to do so using an *algebraic*, or *zero-equation* model, directly computing it from the available flow quantities and user-provided parameters. Examples of this category are Prandtl's mixing length model [66], which defines the turbulent viscosity as

$$\mu_T = \langle \rho \rangle \, \ell_m^2 \sqrt{2 \widetilde{S}_{ij} \widetilde{S}_{ij}} \quad , \tag{6.23}$$

where the mixing length ℓ_m has to be specified as an input to the model. These models drop the term $2/3 \langle \rho \rangle k \delta_{ij}$ from (6.17) and the molecular diffusion term $\left\langle \tau_{ij} u_i'' \right\rangle$ from the mean energy equation (6.11c). For low-Mach number flows this is a good approximation and is even applicable for higher level closure models, since the energy contained in the turbulence is much smaller than the mean enthalpy, i.e. $k \ll \widetilde{h}$ [84]. Other examples for algebraic models, which are more modern variants of the mixing length model, include the model by Smith and Cebeci [75], Wilcox [84] and the Baldwin-Lomax model [2, 84], all of which employ special treatment for the boundary layer near walls.

The Turbulent Kinetic Energy model [84], independently developed by Kolmogorov [33] and Prandtl and Wiegehardt [67] is an example for a one-equation model. It solves the transport equation for the TKE (6.20), assuming that

$$\varepsilon = C_D \frac{k^{\frac{3}{2}}}{\ell} \quad \text{and}$$
$$\mu_T = \langle \rho \rangle \, \ell \sqrt{k} \quad ,$$

where C_D is a model constant commonly chosen between 0.07 and 0.09 and ℓ is the turbulent length scale that, as ℓ_m for the mixing length model

(6.23), must be specified as an input. Other one-equation models are not based on the TKE, but directly solve a transport equation for the kinematic turbulent viscosity $\nu_T = \mu_T/\langle\rho\rangle$. Examples of such models would be the one proposed by Nee and Kovasznay [54] and the more refined models by Baldwin and Barth [1] and by Spalart and Allmaras [78].

All algebraic and the Turbulent Kinetic Energy models have the serious disadvantage of being incomplete, as they require the specification of a length scale field as an input. The Baldwin-Barth and Spalart-Allmaras models are both examples for closures at the lowest possible level. They are mostly applicable to aerodynamic flows, where they proved to be quite successful. However, they are not general.

More popular for general applications are the so called *two-equation models*, for which the famous $k-\varepsilon$ [32, 39] and the $k-\omega$ [83, 84] models are the prime examples. All of them have in common that they not only solve an equation for k, but also for the turbulent length scale, or another variable which allows it to be computed. Consequently, all of these models are complete, as they do not require the length scale to be specified a priori. The so-called *standard* $k-\varepsilon$ model by Jones and Launder [32], later recalibrated by Launder and Sharma [39], is arguably the most widely used turbulence model, and the one used for the simulations in this work. It defines the turbulent viscosity as

$$\mu_T = \langle\rho\rangle\, C_\mu \frac{k^2}{\varepsilon} \quad , \tag{6.24}$$

where for k equation (6.20) is solved and the gradient-diffusion approximation (6.22) is employed to model the turbulent transport and pressure diffusion. ε evolves according to the modelled equation

$$\frac{\partial \langle\rho\rangle \varepsilon}{\partial t} + \frac{\partial \langle\rho\rangle \widetilde{U}_j \varepsilon}{\partial x_j} = C_{\varepsilon 1} \frac{\varepsilon}{k} \widetilde{u_i'' u_j''} \frac{\partial \widetilde{U}_i}{\partial x_j} - C_{\varepsilon 2} \langle\rho\rangle \frac{\varepsilon^2}{k} + \frac{\partial}{\partial x_j}\left[\left(\mu + \frac{\mu_T}{\sigma_\varepsilon}\right)\frac{\partial \varepsilon}{\partial x_j}\right] \quad . \tag{6.25}$$

Although an exact transport equation for the turbulent dissipation ε can be derived [84], it contains many unclosed terms which would be very difficult to model and are almost impossible to measure experimentally. This is the reason that a modelled equation with a similar form as the transport equation for k, has been developed. Also, note that the turbulent transport has been modelled using the same gradient diffusion ansatz as for the TKE

in (6.22). The model coefficients as specified by Launder and Sharma [39] are

$$\begin{aligned} C_{\varepsilon 1} = 1.44, \qquad C_{\varepsilon 2} = 1.92, \qquad C_\mu = 0.09, \\ \sigma_k = 1.0 \quad \text{and} \quad \sigma_\varepsilon = 1.3 \quad . \end{aligned} \tag{6.26}$$

However, these coefficients have been shown to produce bad predictions for a number of flow patterns, such as circular jets, where the model is known to significantly over-predict the spreading rate of the jet. Several extensions have been proposed, modifying the C_μ, $C_{\varepsilon 1}$ and $C_{\varepsilon 2}$ coefficients for this flow scenario as a function of the jet half-width (the distance from the jet centre line to the location where the velocity is half the centre line velocity) and the flow variables and their gradients at the jet centre line. Refer to Launder et al. [38], Rodi [69], McGuirk and Rodi [45], Morse [49] and Hackett and Pope [21]. All of these modifications, with the exception of the one by Hackett and Pope, have in common that they are specific to the flow configuration, depending on centre line values and are purely empirical with no convincing physical motivation. Hackett and Pope point out that just increasing $C_{\varepsilon 1}$ to a value of 1.6 also produces the desired result for this setup.

6.2.2 Reynolds Stress Models

Instead of making the eddy-viscosity assumption (6.17), so called Reynolds Stress models solve the transport equations (6.12) for the individual stress components directly, thus providing a second moment closure. For this type of models, the main challenge lies in devising an appropriate approximation for the *pressure-rate-of-strain* tensor $\mathbf{\Pi}$ defined by (6.15). Modelling of the Reynolds stress equations is outside the scope of this work and the interested reader is referred to Wilcox [84] for a very thorough treatise on the topic.

7 Transported Joint PDF Equations

The goal of this section is to find a description for the *statistical* evolution of the flow quantities. This can be achieved by deriving a transport equation for the one-point joint velocity-composition probability density function (JPDF) $f_{\boldsymbol{U},\boldsymbol{\phi}}(\boldsymbol{V},\boldsymbol{\psi};\boldsymbol{x},t)$. Given a point in space $\boldsymbol{x}$ and a time t it defines the probability density of the velocity taking the value $\boldsymbol{U}=\boldsymbol{V}$ *and* the composition being $\boldsymbol{\phi}=\boldsymbol{\psi}$.

The primary motivation for solving the JPDF transport equation is that any one-point statistical moment , such as mean, variance and covariances, can be recovered. For example

$$\langle\rho\rangle\,\widetilde{U}_i = \int_{-\infty}^{+\infty}\!\!\int V_i\rho(\boldsymbol{\psi})f_{\boldsymbol{U},\boldsymbol{\phi}}(\boldsymbol{V},\boldsymbol{\psi};\boldsymbol{x},t)\mathrm{d}\boldsymbol{V}\mathrm{d}\boldsymbol{\psi} \quad ,$$

$$\langle\rho\rangle\,\widetilde{u_i''u_j''} = \int_{-\infty}^{+\infty}\!\!\int (V_i-\langle U_i\rangle)(V_j-\langle U_j\rangle)\rho(\boldsymbol{\psi})f_{\boldsymbol{U},\boldsymbol{\phi}}(\boldsymbol{V},\boldsymbol{\psi};\boldsymbol{x},t)\mathrm{d}\boldsymbol{V}\mathrm{d}\boldsymbol{\psi} \quad ,$$

$$\langle\rho\rangle\,\widetilde{\phi_\alpha} = \int_{-\infty}^{+\infty}\!\!\int \psi_\alpha\rho(\boldsymbol{\psi})f_{\boldsymbol{U},\boldsymbol{\phi}}(\boldsymbol{V},\boldsymbol{\psi};\boldsymbol{x},t)\mathrm{d}\boldsymbol{V}\mathrm{d}\boldsymbol{\psi} \quad .$$

This means that the turbulent transport terms, e.g. $\widetilde{\boldsymbol{u}''h''}$, are all closed and hence need no modelling. In particular, this also includes the – in the RANS context notoriously difficult to model – mean chemical source term $\widetilde{\dot{\omega}_\alpha(\boldsymbol{\phi})}$ in the species transport equation. However, the one-point PDF cannot provide information about gradients, which would require multipoint statistics. For example the scalar dissipation rate

$$\widetilde{\chi}_\alpha = 2\Gamma_\alpha\widetilde{\frac{\partial\phi_\alpha''}{\partial x_i}\frac{\partial\phi_\alpha''}{\partial x_i}} \tag{7.1}$$

involves gradients of the scalar field $\boldsymbol{\phi}''$, which cannot be computed from the one-point PDF, thus requiring modelling.

7.1 Derivation of the JPDF Transport Equation

Pope [62, Sec. 3.5] and Fox [17, Sec. 6.2] derive the PDF transport equation for the Navier-Stokes equations by finding two independent expressions for the mean convected derivative of a nearly arbitrary function of the velocity and compositions. Both expressions being equal, they can be equated and the remaining terms will then form the PDF transport equation because the function for which the expression has been derived is arbitrary.

First Form Let $Q(\boldsymbol{U}, \boldsymbol{\phi})$ be an arbitrary measurable, one-point scalar function. Since velocity $\boldsymbol{U}$ and composition $\boldsymbol{\phi}$ are random fields, Q must also be a random field. Its mean transport can be expressed as

$$\begin{aligned}\left\langle \rho \frac{\mathrm{D}Q}{\mathrm{D}t} \right\rangle &= \frac{\partial \langle \rho Q \rangle}{\partial t} + \frac{\partial \langle \rho U_i Q \rangle}{\partial x_i} \\ &= \frac{\partial}{\partial t} \int\limits_{-\infty}^{+\infty}\!\!\!\int Q(\boldsymbol{V}, \boldsymbol{\psi}) \rho(\boldsymbol{\psi}) f \,\mathrm{d}\boldsymbol{V}\,\mathrm{d}\boldsymbol{\psi} \\ &\quad + \frac{\partial}{\partial x_i} \int\limits_{-\infty}^{+\infty}\!\!\!\int V_i Q(\boldsymbol{V}, \boldsymbol{\psi}) \rho(\boldsymbol{\psi}) f \,\mathrm{d}\boldsymbol{V}\,\mathrm{d}\boldsymbol{\psi} \\ &= \int\limits_{-\infty}^{+\infty}\!\!\!\int Q(\boldsymbol{V}, \boldsymbol{\psi}) \left(\rho(\boldsymbol{\psi}) \frac{\partial f}{\partial t} + \rho(\boldsymbol{\psi}) V_i \frac{\partial f}{\partial x_i} \right) \mathrm{d}\boldsymbol{V}\,\mathrm{d}\boldsymbol{\psi} \quad ,\end{aligned} \tag{7.2}$$

where in the first step the continuity equation(4.10) and the fact that the expectation operator commutes with the derivative were used. The second step simply expands the expectation operator. The last simplification is due to Q not being a function of space and time since $\boldsymbol{V}$ and $\boldsymbol{\psi}$ are independent variables. Note that the subscripts and arguments to the PDF have been dropped for brevity.

Second Form Using the chain rule, the expected convective derivative of Q can also be written as

$$\begin{aligned}\left\langle \rho \frac{\mathrm{D}Q}{\mathrm{D}t} \right\rangle &= \left\langle \rho \frac{\partial Q}{\partial U_i} \left(\frac{\partial U_i}{\partial t} + U_j \frac{\partial U_i}{\partial x_j} \right) \right\rangle \\ &\quad + \left\langle \rho \frac{\partial Q}{\partial \phi_k} \left(\frac{\partial \phi_k}{\partial t} + U_j \frac{\partial \phi_k}{\partial x_j} \right) \right\rangle \\ &= \left\langle \rho \frac{\partial Q}{\partial U_i} A_i \right\rangle + \left\langle \rho \frac{\partial Q}{\partial \phi_k} \Theta_k \right\rangle \quad ,\end{aligned} \tag{7.3}$$

where the abbreviations $\boldsymbol{A}$ and $\boldsymbol{\Theta}$ have been introduced for the convective derivative of $\boldsymbol{U}$ and $\boldsymbol{\phi}$, respectively. Both are random variables depending on multipoint information of $\boldsymbol{U}$ and $\boldsymbol{\phi}$, such as gradients and Laplacians. For the further discussion, they will be collected into the random vector $\boldsymbol{Z}(\boldsymbol{x}, t)$. Using the definition of a conditional PDF, the PDF of $\boldsymbol{U}$, $\boldsymbol{\phi}$ and $\boldsymbol{Z}$ can be written as

$$f_{\boldsymbol{U},\boldsymbol{\phi},\boldsymbol{Z}}(\boldsymbol{V}, \boldsymbol{\psi}, z) = f_{\boldsymbol{Z}|\boldsymbol{U},\boldsymbol{\phi}}(z|\boldsymbol{V}, \boldsymbol{\psi}) f_{\boldsymbol{U},\boldsymbol{\phi}}(\boldsymbol{V}, \boldsymbol{\psi}) \quad , \tag{7.4}$$

here z being the sample-space variable of $\boldsymbol{Z}$. Using (7.4), the expected value of the term involving $\boldsymbol{A}$ in (7.3) can be expressed as

$$\begin{aligned}\left\langle \rho \frac{\partial Q}{\partial U_i} A_i \right\rangle &= \int_{-\infty}^{+\infty}\int\int \rho(\boldsymbol{\psi}) \frac{\partial Q(\boldsymbol{V}, \boldsymbol{\psi})}{\partial V_i} A_i(\boldsymbol{V}, \boldsymbol{\psi}, z) f_{\boldsymbol{U},\boldsymbol{\phi},\boldsymbol{Z}}(\boldsymbol{V}, \boldsymbol{\psi}, z) \mathrm{d}\boldsymbol{V} \mathrm{d}\boldsymbol{\psi} \mathrm{d}z \\ &= \int_{-\infty}^{+\infty}\int \rho(\boldsymbol{\psi}) \frac{\partial Q(\boldsymbol{V}, \boldsymbol{\psi})}{\partial V_i} \langle A_i|\boldsymbol{V}, \boldsymbol{\psi}\rangle f \mathrm{d}\boldsymbol{V} \mathrm{d}\boldsymbol{\psi}\end{aligned} \tag{7.5}$$

with the conditional expectation

$$\langle A_i|\boldsymbol{V}, \boldsymbol{\psi}\rangle = \int_{-\infty}^{+\infty} A_i(\boldsymbol{V}, \boldsymbol{\psi}) f_{\boldsymbol{Z}|\boldsymbol{U},\boldsymbol{\phi}}(z|\boldsymbol{V}, \boldsymbol{\psi}) \mathrm{d}z \quad .$$

Similarly, for the term containing $\boldsymbol{\Theta}$ it follows

$$\left\langle \rho \frac{\partial Q}{\partial \phi_k} \Theta_j \right\rangle = \int_{-\infty}^{+\infty}\int \rho(\boldsymbol{\psi}) \frac{\partial Q(\boldsymbol{V}, \boldsymbol{\psi})}{\partial \psi_k} \langle \Theta_k|\boldsymbol{V}, \boldsymbol{\psi}\rangle f \mathrm{d}\boldsymbol{V} \mathrm{d}\boldsymbol{\psi} \quad . \tag{7.6}$$

Using integration by parts over V_i for (7.5) and over ψ_k for (7.6), respectively, and by exploiting the fact that the PDF's are required to have

compact support (i.e. vanish at infinity), the mean convective transport in its second form can now be written as

$$\left\langle \rho \frac{\mathrm{D}Q}{\mathrm{D}t} \right\rangle = -\int_{-\infty}^{+\infty}\!\!\!\!\!\!\int Q(\boldsymbol{V},\boldsymbol{\psi}) \left(\frac{\partial \rho(\boldsymbol{\psi}) \left\langle A_i | \boldsymbol{V},\boldsymbol{\psi} \right\rangle f}{\partial V_i} + \frac{\partial \rho(\boldsymbol{\psi}) \left\langle \Theta_j | \boldsymbol{V},\boldsymbol{\psi} \right\rangle f}{\partial \psi_k} \right) \mathrm{d}\boldsymbol{V}\mathrm{d}\boldsymbol{\psi} \quad (7.7)$$

Final Form Equating (7.2) and (7.7) and using the fact that the expression must hold for arbitrary choices of Q, the basic form of the PDF transport equation follows as

$$\rho \frac{\partial f}{\partial t} + \rho V_i \frac{\partial f}{\partial x_i} = -\frac{\partial \rho \left\langle A_i | \boldsymbol{V},\boldsymbol{\psi} \right\rangle f}{\partial V_i} - \frac{\partial \rho \left\langle \Theta_k | \boldsymbol{V},\boldsymbol{\psi} \right\rangle f}{\partial \psi_k} \quad . \quad (7.8)$$

This equation is exact and so far involves no modelling. However, for the conditional fluxes $\langle \boldsymbol{A} | \boldsymbol{V},\boldsymbol{\psi} \rangle$ and $\langle \boldsymbol{\Theta} | \boldsymbol{V},\boldsymbol{\psi} \rangle$ closures need to be provided to actually introduce the physics into the equation. First, they are expanded by the right-hand sides of the momentum transport equation (4.18), excluding volume forces, and the species mass transport equation (4.29):

$$\rho(\boldsymbol{\psi}) \left\langle A_i | \boldsymbol{V},\boldsymbol{\psi} \right\rangle = -\frac{\partial \left\langle p \right\rangle}{\partial x_i} + \frac{\partial \left\langle \tau_{ij} \right\rangle}{\partial x_j} + \left\langle \frac{\partial \tau'_{ij}}{\partial x_j} - \frac{\partial p'}{\partial x_i} \middle| \boldsymbol{V},\boldsymbol{\psi} \right\rangle \quad (7.9)$$

$$\rho(\boldsymbol{\psi}) \left\langle \Theta_\alpha | \boldsymbol{V},\boldsymbol{\psi} \right\rangle = \rho(\boldsymbol{\psi}) \dot{\omega}_\alpha(\boldsymbol{\psi}) - \frac{\partial \left\langle J_{\alpha,i} \right\rangle}{\partial x_i} - \left\langle \frac{\partial J'_{\alpha,i}}{\partial x_i} \middle| \boldsymbol{V},\boldsymbol{\psi} \right\rangle \quad . \quad (7.10)$$

Here, the diffusion fluxes have been abbreviated as $\boldsymbol{J}_\alpha$. The conditional moments of (7.9) account for the effects of the fluctuating viscous stresses and the pressure fluctuations. Being unclosed they are one of the modelling challenges together with the unclosed third term of (7.10), which describes molecular diffusion and is of imminent importance for reactive flows. It is noteworthy that the chemical source term $\dot{\boldsymbol{\omega}}$ appears in closed form. For high-Reynolds-number flows away from walls the mean viscous stress and the mean diffusion are of little importance and will be neglected in the further discussion. Using (7.9) and (7.10) with above mentioned simplifications,

the PDF transport equation (7.8) reads

$$\rho(\boldsymbol{\psi})\frac{\partial f}{\partial t}+\rho(\boldsymbol{\psi})V_i\frac{\partial f}{\partial x_i}-\frac{\partial\langle p\rangle}{\partial x_i}\frac{\partial f}{\partial V_i}+\frac{\partial\rho(\boldsymbol{\psi})\dot{\omega}_k(\boldsymbol{\psi})f}{\partial\psi_k}= \\ -\frac{\partial}{\partial V_i}\left(\left\langle\frac{\partial\tau'_{ij}}{\partial x_j}-\frac{\partial p'}{\partial x_i}\middle|\boldsymbol{V},\boldsymbol{\psi}\right\rangle f\right)+\frac{\partial}{\partial\psi_k}\left(\left\langle\frac{\partial J'_{k,i}}{\partial x_i}\middle|\boldsymbol{V},\boldsymbol{\psi}\right\rangle f\right) \quad , \tag{7.11}$$

where the closed terms have been moved to the left-hand side of the equation.

When dealing with variable density flows, as e.g. in reactive flows, it is often more natural to use the mass-weighted PDF given by

$$\tilde{f}=\frac{\rho(\boldsymbol{\psi})}{\langle\rho\rangle}f \tag{7.12}$$

and the mass-density function (MDF)

$$\begin{aligned}\mathcal{F}_{U,\boldsymbol{\phi},X}(\boldsymbol{V},\boldsymbol{\psi},\boldsymbol{x};t)&\equiv\rho(\boldsymbol{\psi})f(\boldsymbol{V},\boldsymbol{\psi};\boldsymbol{x},t)\\&\equiv\langle\rho\rangle(\boldsymbol{x},t)\widetilde{f}(\boldsymbol{V},\boldsymbol{\psi};\boldsymbol{x},t) \quad .\end{aligned} \tag{7.13}$$

By integration over the whole sample space, the mean density is recovered, making it clear why working with the MDF is beneficial for variable density flows, where the conservation of mass is of utmost importance:

$$\int_{-\infty}^{+\infty}\!\!\!\int\mathcal{F}_{U,\boldsymbol{\phi},X}(\boldsymbol{V},\boldsymbol{\psi},\boldsymbol{x};t)\mathrm{d}\boldsymbol{V}\mathrm{d}\boldsymbol{\psi}=\langle\rho\rangle(\boldsymbol{x},t) \quad .$$

Substituting the definition of the MDF (7.13) into the PDF transport equation (7.11) and using the continuity equation, the MDF transport equation

$$\frac{\partial\mathcal{F}}{\partial t}+\frac{\partial V_i\mathcal{F}}{\partial x_i}-\frac{1}{\langle\rho\rangle}\frac{\partial\langle p\rangle}{\partial x_i}\frac{\partial\mathcal{F}}{\partial V_i}+\frac{\partial\dot{\omega}_k\mathcal{F}}{\partial\psi_k}= \\ -\frac{\partial}{\partial V_i}\left(\left\langle\frac{1}{\rho(\boldsymbol{\psi})}\frac{\partial\tau'_{ij}}{\partial x_j}-\frac{1}{\rho(\boldsymbol{\psi})}\frac{\partial p'}{\partial x_i}\middle|\boldsymbol{V},\boldsymbol{\psi}\right\rangle\mathcal{F}\right) \\ +\frac{\partial}{\partial\psi_k}\left(\left\langle\frac{1}{\rho(\boldsymbol{\psi})}\frac{\partial J'_{k,i}}{\partial x_i}\middle|\boldsymbol{V},\boldsymbol{\psi}\right\rangle\mathcal{F}\right) \tag{7.14}$$

is obtained, dropping the subscripts from the MDF for the sake of brevity.

7.2 Relationship with the Reynolds-Averaged Equations

By taking the appropriate moments of the PDF transport equation (7.11), the Reynolds-averaged equations (6.11a) to (6.11d) can be recovered. E.g. the mean continuity equation can be obtained by integrating (7.14) over the full sample space and the momentum equation is obtained by multiplying the MDF transport equation with V_i before integrating over the sample space. For the derivations of the momentum and Reynolds-stress equations, it is referred to Fox [17, Sec. 6.4].

7.3 Closure of the Conditional Acceleration Term

An approach that has been successfully employed for the solution of PDF transport equations is to construct a stochastic system, which is linear in $\boldsymbol{V}$ and results in a realisable Reynolds-stress model; see Haworth and Pope [24]. These models have the form

$$\left\langle \frac{\partial \tau'_{ij}}{\partial x_j} - \frac{\partial p'}{\partial x_i} \middle| \boldsymbol{V}, \boldsymbol{\psi} \right\rangle = G_{ij}(V_i - \widetilde{U}_j) - \frac{C_0 \varepsilon}{2f} \frac{\partial f}{\partial V_i} \quad , \tag{7.15}$$

where the tensor $\mathbf{G}$ is a function of the Reynolds stresses $\widetilde{u''_i u''_j}$, the mean velocity gradients $\partial \widetilde{U}_i / \partial x_j$ and the dissipation rate ε. For the simplified Langevin model (SLM) [63] , G_{ij} is defined as

$$G_{ij} = -\left(\frac{1}{2} + \frac{3}{4} C_0\right) \frac{\varepsilon}{k} \delta_{ij} \tag{7.16}$$

and for the particular choice of $C_0 = 2.1$ Rotta's Reynolds stress model is recovered [62]. The generalised Langevin model (GLM) [24], on the other hand, models G_{ij} as

$$G_{ij} = \frac{\varepsilon}{k} \left(\alpha_1 \delta_{ij} + \alpha_2 b_{ij} + \alpha_3 b_{ij}^2\right) H_{ijkl} \frac{\partial \widetilde{U}_k}{\partial x_l} \quad , \tag{7.17}$$

$\mathbf{b} = \widetilde{u''_i u''_j} / 2k - \delta_{ij}/3$ being the anisotropy tensor and $\mathbf{H}$ a fourth-order tensor, which is linear in $\mathbf{b}$ and in addition to α_1, α_2 and α_3 contains 9 further model parameters. Totalling 12 model parameters, the GLM can be made consistent with any realisable Reynolds-stress model [64].

7.4 Closure of the Molecular Mixing Term

In order to find a closure for the molecular mixing term $\langle {}^{\partial J'_{\alpha,i}}/_{\partial x_i} | \boldsymbol{V}, \boldsymbol{\psi} \rangle$, one must be aware of important constraints that such a model must fulfil [17, Sec. 6.6.1]:

1. The model must not directly change the scalar mean.
2. The model must yield the correct scalar dissipation rate (7.1).
3. The model must result in the correct local scalar isotropy.

While the first constraint is honoured by most mixing models, the second one is very difficult to achieve since it involves the modelling of gradient information. The third constraint is largely ignored [17]. Fox [17, Sec. 6.6.2] further formulates *desirable* properties that a mixing model should fulfil:

1. In homogeneous turbulence, the PDF of inert scalars should relax from arbitrary initial conditions to a multivariate Gaussian distribution.
2. All scalars must remain in the allowable range.
3. The mean of any conserved linear combination must be preserved.
4. Mixing should be local in scalar space.
5. The evolution of the scalar PDF should depend on the distribution of the length scales in the scalar fields.
6. Known Reynolds, Schmidt and Damköhler number dependencies should be included.

The physical motivations for these desirable properties can be found in Fox [17, Sec. 6.5.8].

There exists a large number of mixing models published in literature, some of which are the Curl or CD model proposed by Curl [13], which uses a stochastic jump process to describe molecular mixing and for which several modified versions exist; the very sophisticated EMST model by Subramaniam and Pope [80], whose outstanding feature is the accurate treatment of locality in scalar space; or the PSP model by Meyer and Jenny [47], which is based on parametrised profiles to model scalar gradients, inherently providing information about the scalar dissipation rate. In this work the discussion

is limited to the very simple interaction by exchange with the mean (IEM) model which, as its name hints at, relaxes the scalar to its mean value:

$$\left\langle \frac{\partial J'_{\alpha,i}}{\partial x_i} \middle| \boldsymbol{V}, \boldsymbol{\psi} \right\rangle = -\frac{\widetilde{\chi}_\alpha}{2\widetilde{\phi''^2_\alpha}}(\psi_\alpha - \widetilde{\phi}_\alpha) \quad . \tag{7.18}$$

Here, the scalar dissipation rate $\widetilde{\chi}_\alpha$ is found using a separate model; most often a simple scales-similarity model assuming a fully developed scalar spectrum is employed [17, Sec. 3.3.4]:

$$\frac{\widetilde{\chi}_\alpha}{2\widetilde{\phi''^2_\alpha}} = C_\phi \frac{\varepsilon}{k} \quad , \tag{7.19}$$

where $C_\phi = {}^{(\widetilde{\phi''^2_\alpha}/\widetilde{\chi}_\alpha)}/_{(k/\varepsilon)}$ is the scalar-to-mechanical time scale ratio, and for inert simulations usually assumed to be $C_\phi \approx 2$. The main drawback of the IEM mixing model is that it preserves the initial shape of the PDF in homogeneous turbulence, just narrowing the profile as time progresses. This problem is not so pronounced in the presence of inhomogeneity in the turbulent flow field.

Note that many of the available mixing models have been developed at the level of stochastic processes, which will be discussed in Section 9.1.

7.5 The Modelled JPDF Transport Equation

Bringing everything together by applying the simplified Langevin model and the IEM mixing model to the unclosed JPDF transport equation (7.11), the modelled joint velocity-composition PDF transport equation is obtained which reads

$$\begin{aligned} \rho(\boldsymbol{\psi})\frac{\partial f}{\partial t} + \rho(\boldsymbol{\psi})V_i\frac{\partial f}{\partial x_i} - \frac{\partial \langle p \rangle}{\partial x_i}\frac{\partial f}{\partial V_i} + \frac{\partial \rho(\boldsymbol{\psi})\dot{\omega}_k(\boldsymbol{\psi})f}{\partial \psi_k} = \\ \left(\frac{1}{2} + \frac{3}{4}C_0\right)\frac{\varepsilon}{k}\delta_{ij}\frac{\partial\left(V_i - \widetilde{U}_j\right)f}{\partial V_i} + \frac{C_0\varepsilon}{2}\frac{\partial^2 f}{\partial V_i^2} \\ - \frac{\partial}{\partial \psi_k}\left(C_\phi\frac{\varepsilon}{k}\left(\psi_k - \widetilde{\phi}_k\right)f\right) \quad . \end{aligned} \tag{7.20}$$

8 Turbulent Combustion

This section briefly introduces the reader to the various combustion regimes and the relevant modelling approaches. However, this is a large research field on its own and no attempt at completeness will be made in this work.

The primary types of combustion are premixed, non-premixed and partially premixed combustion. These are related to the way in which the fuel and oxidiser enter the combustion chamber. In premixed mode, the reactants and the oxidiser (most commonly air) enter the domain in a fully mixed state. Stationary gas turbines and spark-ignition engines are typical examples. If they enter separately and are separated by the flame surface, on the other hand, the flame is non-premixed. Partially premixed flames exhibit characteristics of both major combustion modes.

8.1 Premixed Combustion

In premixed combustion, there exists a flame front feeding into the unburnt mixture, cleanly separating it from the burnt products. In the laminar flow regime this propagation speed is denoted by the laminar flame speed s_L. Inside the reaction front, several zones can be identified as depicted in Figure 8.1: the preheat zone, the reaction zone (or inner layer) and the oxidation layer. The first is mainly due to heat diffusion, the primary reason for the flame propagation. Because of the rising temperature, dissociation occurs and thus the preheat zone is responsible for the formation of radical pools, which are crucial for the reaction zone, where most of the fuel conversion occurs. The last zone, the oxidation layer, is responsible for the reduction of the radical pools and very slow chemical reactions with little heat release take place, such as the formation of nitric oxide (NO).

In a turbulent flow field the eddies interact with the flame front. The form of this interaction is a further characteristic for a turbulent flame. If the smallest eddies are only able to bend and wrinkle the flame front, this is referred to as the wrinkled or corrugated flamelet regime. Here, the

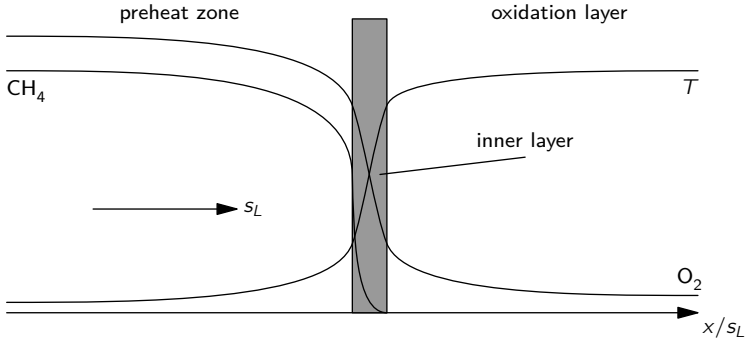

Figure 8.1 – Sketch of the flame structure for a premixed CH_4-air flame.

chemical time scales are much smaller than the shortest flow time scales, i.e. the *Karlowitz* number

$$Ka = \frac{\tau_c}{\tau_K}$$

is smaller than 1. Here, τ_c is the largest relevant chemical time scale and $\tau_K = \sqrt{\nu/\varepsilon}$ is the Kolmogorov time scale. For $1 < Ka < 100$, the smallest eddies penetrate the preheat zone, giving rise to the thin-reaction regime. In the broken reaction zone regime, where $Ka > 100$, the turbulence disrupts the inner layer, literally breaking up the flame front.

Another characteristic can be found by relating the integral turbulent time scale τ_l to the largest relevant chemical time scale τ_c, giving rise to the *Damköhler* number

$$Da = \frac{\tau_l}{\tau_c} \quad .$$

It distinguishes flames where the fuel conversion rate is limited by the chemical reaction rates from ones limited by the molecular and turbulent mixing, that is by the rate at which heat and products are diffused and transported away and reactants are brought to the flame front.

The turbulent flame is further influenced by physical effects, such as the following:

1. Strain in the flow field causes heat to be diffused away from the flame, reducing the flame temperature, potentially even quenching it.

2. The heat released by the flame leads to gas expansion, giving rise to counter gradient diffusion. Gradient diffusion models for scalar fluxes are not appropriate, if this effect is of importance.

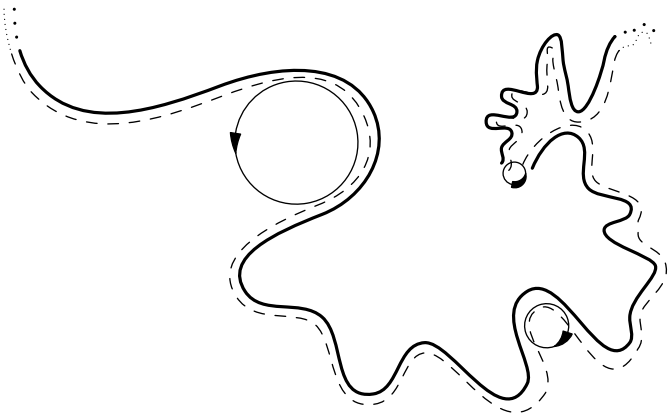

Figure 8.2 – Sketch of a turbulent flame front, illustrating the corrugated flamelet, thin-reaction and broken reaction zone regimes.

3. The flow acceleration and heat release can enhance, or even generate turbulence.

4. Temperature-dependence of the viscosity can potentially lead to laminarisation downstream of the flame.

A central parameter for the premixed combustion mode is the equivalence ratio. When considering a single fuel species F and a single oxidiser species O with the forward stoichiometric coefficients $\upsilon_{\mathrm{F}}^{f}$ and $\upsilon_{\mathrm{O}}^{f}$ for a global reaction of the form

$$\upsilon_{\mathrm{F}}{}^{\mathrm{f}}\mathrm{F} + \upsilon_{\mathrm{O}}^{f}\mathrm{O} \longrightarrow \text{Products}$$

stoichiometric conditions are given for

$$s = \left(\frac{Y_{\mathrm{O}}}{Y_{\mathrm{F}}}\right)_{\mathrm{st}} = \frac{\upsilon_{\mathrm{O}}^{f} W_{\mathrm{O}}}{\upsilon_{\mathrm{F}}^{f} W_{\mathrm{F}}} \quad , \tag{8.1}$$

where s is the mass-stoichiometric ratio. The equivalence ratio of a mixture is then defined as

$$\phi = s\frac{Y_{\mathrm{F}}}{Y_{\mathrm{O}}} \quad . \tag{8.2}$$

If there is not enough oxidiser present to fully convert all fuel molecules, the flame is said to be *rich* and $\phi > 1$. Conversely, in *lean* combustion the oxidiser is in excess and $\phi < 1$.

The interested reader is referred to the literature for the details of the physics relevant to turbulent flames and their characterisation, e.g. Peters [59] or Poinsot and Veynante [61].

8.2 Non-Premixed and Partially Premixed Combustion

In the non-premixed regime, fuel and oxidiser enter the combustor as separate streams. Only due to molecular diffusion a flammable mixture is formed, and provided that enough heat is present, the flame will be located on the stoichiometric manifold. In contrast to premixed combustion, the flame is not able to propagate away from the stoichiometric surface. This makes the dreaded flashbacks, where the flame propagates back into the fuel supply, impossible. However, the overall reaction rate is limited by the diffusion of fuel and oxidiser towards the reaction zone. This dependence on the diffusion process gives rise to another name for this type of combustion: *diffusion flames*. In addition to the physical effects of turbulence-flame interaction described above for premixed combustion, here the impact of the turbulence on the turbulent mixing process adds another complication as the eddies are able to modify the diffusion layer surrounding the flame, thus changing the mass and heat flow rates to and from the flame.

In regions where the turbulence level is too high, the heat is transported away from the flame at such a high rate that the flame is quenched. In these regions the fuel and oxidiser can mix without being consumed. Once this mixture reaches a lower turbulence intensity further downstream and the local heat is sufficient, a premixed type of combustion takes place locally, which is why this is called a *partially-premixed* flame. Usually these areas of premixed combustion are connected to a diffusion flame surface, provided the required ignition energy is achieved. These structures form the so-called *triple-edge* flames, since there exists a lean and a rich premixed branch expanding from the stoichiometric surface towards the oxidiser and fuel sides, respectively, and a third, non-premixed flame branch is located along the stoichiometric surface, as is illustrated in Figure 8.3. This type of flame is typical for jet burners, where a very fast fuel jet is surrounded by a relatively slow co-flow supplying the oxidiser. If the jet is too fast, the diffusion flame fails to attach to the burner rim, allowing fuel and oxidiser to mix without any reactions taking place before reaching the flame front.

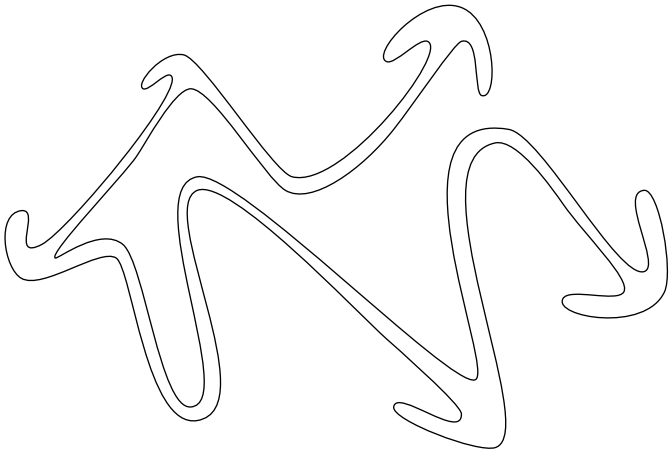

Figure 8.3 – Illustration of triple flames embedded in a turbulent flow field. The long stretched structures are the diffusion flames located along the stochiometric manifold. At their ends, premixed flame branches feed into the partially premixed gases, forming the characteristic triple edge flames (inspired by Peters [59]).

8.3 Models for Premixed Combustion

The details of turbulent combustion modelling are not topic of this work, and consequently will only briefly be touched upon, in particular for the premixed mode of combustion.

Most models for premixed combustion solve a transport equation of a scalar indicating the location of the flame front. Finding the source terms that describe the interaction of the flame with the turbulent flow field is the major hurdle for these models. In the BML-model proposed by Bray, Moss and Libby [9] a transport equation for a progress variable, the normalised temperature c, is solved:

$$\frac{\partial \langle\rho\rangle \widetilde{c}}{\partial t} + \frac{\partial \langle\rho\rangle \widetilde{U}_i \widetilde{c}}{\partial x_i} = -\frac{\partial \langle\rho\rangle \widetilde{u_i'' c''}}{\partial x_i} + \langle\rho S_c\rangle \quad .$$

Unburnt mixture is indicated by $c = 0$ and $c = 1$ indicates the burnt state. In flame regimes close to the thin reaction zone, the distribution of c is assumed to be bimodal as the conversion from the unburnt to the burnt state is assumed to occur instantaneously with respect to the flow time scales. As already mentioned, finding appropriate models for the source

term $\langle \rho S_c \rangle$ in the transport equation for the mean progress variable is the main challenge of this approach.

Another popular model, mainly applicable to the corrugated flamelet regime, is the level-set, or G-equation approach; see Osher and Sethian [57] or Williams [86] among others. Here, the transport equation

$$\rho \frac{\partial G}{\partial t} + \rho U_i \frac{\partial G}{\partial x_i} = \rho_u s_d \left| \frac{\partial G}{\partial x_i} \right| \quad ,$$

for the conserved scalar G is solved, which is used to track the flame front. $G < G_0$ indicates fresh or unburnt gas, and $G > G_0$ indicates burnt gas. Here, s_d is the displacement speed, depending on the laminar flame speed s_L, the local strain rate and the curvature of the iso-surface, and ρ_u is the density of the unburnt gas. G being a non-reactive scalar, its transport equation does not involve a source term that requires modelling, also avoiding complications related to counter-gradient diffusion. However, above transport equation can only be solved directly, if the instantaneous flame surface is fully resolved. In the RANS or LES context, closure of the covariances or filtered terms is anything but straightforward.

8.4 Models for Non-Premixed Combustion

8.4.1 The Burke-Schumann Assumption

If the mixing time scales are much larger than the chemical time scales, chemistry can be regarded as being infinitely fast, allowing the mixing process to be decoupled from the chemical reactions. This assumption has first been introduced by Burke and Schumann [10] in 1928. In order to solve the mixing problem separately from the reaction problem, a conserved scalar must be found that is not subject to change due to chemical reactions. For the case where a single mixture fraction is sufficient to describe the mixing problem (see Section 5.3), Bilger [6] introduced the notion of a normalised mixture fraction z based on the element mass fractions which are not affected by reactions:

$$z = \frac{\frac{Z_C - Z_C^{Ox}}{mW_C} + \frac{Z_H - Z_H^{Ox}}{nW_H} - \frac{Z_O - Z_O^{Ox}}{W_O}}{\frac{Z_C^F - Z_C^{Ox}}{mW_C} + \frac{Z_H^F - Z_H^{Ox}}{nW_H} - \frac{Z_O^F - Z_O^{Ox}}{W_O}} \quad . \tag{8.3}$$

The variables Z_C, Z_H and Z_O are element mass fractions of carbon, hydrogen and oxygen, respectively. This formula was derived for the combustion

of a hydrocarbon with the global reaction of the form

$$4\,C_mH_n + (4m+n)O_2 \longrightarrow 4m\,CO_2 + 2n\,H_2O \quad .$$

The superscripts F and Ox refer to the states in the fuel and oxidiser streams, respectively. It is clear that this definition of the mixture fraction will yield 1 in the fuel stream and 0 in the oxidiser stream, irrespective of their composition (provided that they are not identical).

Using this model, the mass fractions and temperature are given as piecewise linear functions of the mixture fraction z connecting the oxidiser stream, stoichiometric and fuel stream states [61, Sec. 3.3.1], resulting in

$$\begin{bmatrix} Y_F(z) \\ Y_{O_2}(z) \\ T(z) \end{bmatrix} = \begin{cases} \begin{bmatrix} 0 \\ \left(1 - \frac{z}{z_{st}}\right) Y_{O_2}^{Ox} \\ zT^F + (1-z)T^{Ox} + \frac{RY_F^F}{c_p} z \end{bmatrix} & \text{if } z < z_{st} \\ \begin{bmatrix} \frac{z-z_{st}}{1-z_{st}} Y_F^F \\ 0 \\ zT^F + (1-z)T^{Ox} + \frac{RY_F^F}{c_p} z_{st} \frac{1-z}{1-z_{st}} \end{bmatrix} & \text{if } z \geqslant z_{st} \end{cases} ,$$

where Y_F and Y_{O_2} are the fuel and oxidiser mass fractions, respectively. z_{st} is the stoichiometric mixture fraction

$$z_{st} = \frac{1}{1 + \frac{(4m+n)W_{O_2} Y_F^F}{4W_F Y_{O_2}^{Ox}}}$$

and R is the single step reaction rate as given by (5.3). The adiabatic flame temperature at $z = z_{st}$ is consequently given by

$$T_{ad} = z_{st}T^F + (1 - z_{st})T^{Ox} + \frac{RY_F^F}{c_p} z_{st} \quad .$$

8.4.2 The Laminar Flamelet Assumption

Williams [85] proposed the assumption that flames below the broken reaction zone regime can be treated as an ensemble of embedded laminar flames, so called *flamelets*. The rationale is that the laminar diffusion flame sheet is merely twisted and folded by the turbulent flow field, but otherwise left intact as illustrated in Figure 8.4. Liew et al. [41] put forward the idea of using precalculated laminar flame profiles and Peters [58] and Kuznetsov [36]

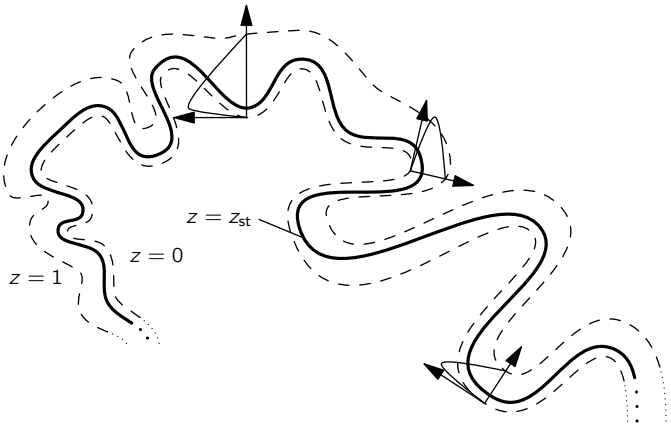

Figure 8.4 – Sketch of an embedded laminar flamelet.

derived a flamelet equation describing a laminar diffusion flame in mixture fraction space, dependent on the scalar dissipation rate:

$$\frac{\partial \phi_\alpha}{\partial t} = \frac{1}{Le_\alpha}\frac{\chi}{2}\frac{\partial^2 \phi_\alpha}{\partial z^2} + \dot{\omega}_\alpha \quad .$$

Here, Le_α is the Lewis number, relating heat and mass diffusion rates

$$Le_\alpha = \frac{\lambda}{\rho c_p \Gamma_\alpha} \quad , \tag{8.4}$$

and χ is the scalar dissipation rate of the mixture fraction

$$\chi = 2\Gamma_z \frac{\partial z}{\partial x_i}\frac{\partial z}{\partial x_i} \quad , \tag{8.5}$$

Γ_z being the diffusion coefficient for the mixture fraction. It is referred to Peters [59] for more information about the choice of Γ_z.

The greatest feature of the flamelet equation is that it is decoupled from the flow problem with the mixture fraction z being a coordinate. This allows it to be solved and tabulated for a range of scalar dissipation rates in a preprocessing step, as is illustrated in Figure 8.5. During the actual flow simulation, only the mixing problem is solved; the thermodynamic state (temperature, density, composition) is then obtained through a simple lookup operation based on the instantaneous mixture fraction and scalar dissipation rate.

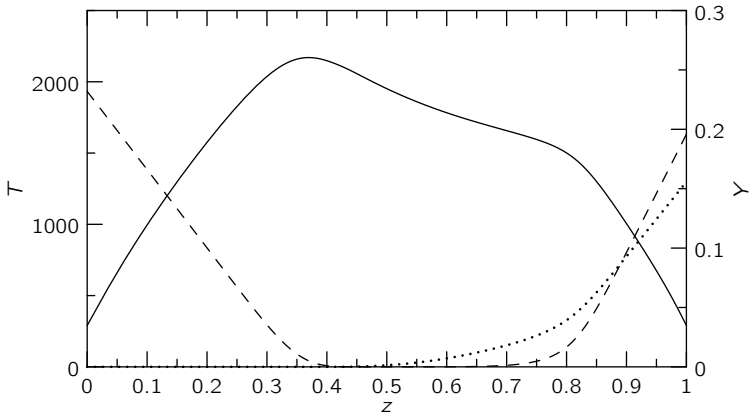

Figure 8.5 – Example flamelet for a CH_4-air flame, where the fuel consists of 25% CH_4 and 75% air. The solid line represents the temperature in K, the dashed and dotted lines the CH_4 and air mass fractions, respectively.

The laminar flamelet assumption is to date one of the most successful modelling approaches for non-premixed turbulent combustion. However, it is only valid if the smallest eddies are not able to penetrate the reaction zone. Similarly, the classical flamelet model fails to predict reignition after local extinction or premixed flame propagation, hence being unsuitable for the modelling of partially-premixed flames. There exist efforts to extend the flamelet model for partially premixed flames, it is referred to e.g. Hegetschweiler et al. [25, 26], Bradley et al. [7, 8], Sanders and Lamers [70], Müller et al. [53] and Chen et al. [12].

Part II
Novel Hybrid FV/Transported JPDF Algorithm

9 Introduction

The transport equation (7.11) describes the evolution of the joint PDF not only in time and physical space, but also in velocity and composition space, resulting in $7 + N_s$ dimensions. Although theoretically possible, applying a classical discretisation approach, such as the finite difference, finite element or finite volume (FV) methods, will not be tractable for any reasonably complex setting as their computational cost scales approximately with the power of the number of dimensions. On the other hand, for Lagrangian Monte-Carlo (MC) methods the computational cost only increases linearly with the number of dimensions. Applying such a scheme for the solution of the PDF/MDF transport equation requires that a stochastic system be devised that is consistent with the transport equation for the Eulerian PDF/MDF, which will be the topic of this and the following sections.

In 1827 Robert Brown for the first time systematically described the agitated, apparently random motion of small pollen particles suspended in water. It was not until Einstein [15] and von Smoluchowski [77] that the phenomenon was understood [18]. Later, Langevin [37, 40] found another description which was, according to him, *infinitely more simple*, resulting in the first example of a stochastic differential equation (SDE) , the theory of which is going to be outlined in the following as far as it is relevant to this work.

The *Langevin* equation

$$\mathrm{d}X(t) = -\frac{1}{\tau}X(t)\mathrm{d}t + \sqrt{\frac{2\sigma^2}{\tau}}\mathrm{d}W(t) \tag{9.1}$$

describes the stochastic evolution of a particle with random position X as a function of a time scale τ and a variance parameter σ^2. $\mathrm{d}W(t)$ is the increment of a so called *Wiener* process, whose properties will be investigated later in this section. Here, it suffices to know that the Wiener increment is an independent random number with normal distribution, zero mean and

a variance equal to the time increment $\mathrm{d}t$. Generalising (9.1), one obtains the canonical form of a SDE

$$\mathrm{d}X_i(t) = a_i(\boldsymbol{x}, t)\mathrm{d}t + b_{ij}(\boldsymbol{x}, t)\xi_j(t)\sqrt{\mathrm{d}t} \quad , \tag{9.2}$$

$\boldsymbol{a}(\boldsymbol{x}, t)$ and $\mathbf{b}(\boldsymbol{x}, t)$ being deterministic functions and $\boldsymbol{\xi}(t)$ a random vector. Equation (9.1) is an example for an *Ornstein-Uhlenbeck* process, where the drift coefficient $a(X, t) = {}^{-X}/_{\tau}$ must be linear in X and the diffusion coefficient $b(X, t) = \sqrt{{}^{2\sigma^2}/_{\tau}}$ constant.

9.1 Stochastic Processes

Colloquially, a stochastic process describes a system which evolves nondeterministically, but probabilistically in time. It is described by a time-dependent random variable $X(t)$, for which samples $\boldsymbol{x}_1, \boldsymbol{x}_2, \ldots$ at times $t_1, t_2, \ldots$ can be taken. Introducing the *Markov* assumption, the future state $\boldsymbol{x}_n$ at time t_n only depends on its previous state $\boldsymbol{x}_{n-1}$ at time t_{n-1}. All previous states $\boldsymbol{x}_{n-k}$ at times t_{n-k} for all $k > 1$ have no influence on $\boldsymbol{x}_n$. Using the definitions of a marginal PDF and a conditional PDF and the Markov assumption, the conditional PDF for the future state $\boldsymbol{x}_2$ at time t_2 given its previous state $\boldsymbol{x}_0$ at t_0 can be derived and reads

$$f(\boldsymbol{x}_2; t_2|\boldsymbol{x}_0, t_0) = \int_{-\infty}^{+\infty} f(\boldsymbol{x}_2; t_2|\boldsymbol{x}_1, t_1) f(\boldsymbol{x}_1; t_1|\boldsymbol{x}_0, t_0)\mathrm{d}\boldsymbol{x}_1 \quad . \tag{9.3}$$

This relation is due to Chapman and Kolmogorov, hence being called the *Chapman-Kolmogorov* equation. It connects all conditional probability density functions $f(\boldsymbol{x}_i; t_i|\boldsymbol{x}_j, t_j)$ to each other, making it a rather complex nonlinear functional equation. Note that the semi-colon (;) is used to separate sample space variables from other coordinates in the arguments of the PDF.

Under certain conditions regarding the continuity properties of the random process, Gardiner [18] derived the differential equation for the conditional PDF $f(\boldsymbol{x}; t|\boldsymbol{x}_0, t_0)$

$$\frac{\partial f(\boldsymbol{x}; t|\boldsymbol{x}_0, t_0)}{\partial t} = -\frac{\partial A_i(\boldsymbol{x}, t) f(\boldsymbol{x}; t|\boldsymbol{x}_0, t_0)}{\partial x_i} + \frac{1}{2}\frac{\partial^2 B_{ij}(\boldsymbol{x}, t) f(\boldsymbol{x}; t|\boldsymbol{x}_0, t_0)}{\partial \boldsymbol{x}_i \partial \boldsymbol{x}_j}$$
$$+ \int_{-\infty}^{+\infty} \left[\mathcal{W}(\boldsymbol{x}|\boldsymbol{x}', t) f(\boldsymbol{x}'; t|\boldsymbol{x}_0, t_0) - \mathcal{W}(\boldsymbol{x}'|\boldsymbol{x}, t) f(\boldsymbol{x}; t|\boldsymbol{x}_0, t_0)\right] \mathrm{d}\boldsymbol{x}' \quad . \tag{9.4}$$

The first two terms on the right hand side give rise to drift and diffusion processes, $\boldsymbol{A}$ and $\mathbf{B}$ being the drift coefficient vector and diffusion coefficients matrix, respectively. The last term describes a *jump* process with jump probability density $\mathcal{W}$. The probability of state $\boldsymbol{y}$ transitioning (or jumping) to state $\boldsymbol{x}$ is given by $\mathcal{W}(\boldsymbol{x}|\boldsymbol{y}, t)\mathrm{d}t$ within the infinitesimal time interval $\mathrm{d}t$. Setting $\boldsymbol{A}$ and $\mathbf{B}$ to null, one obtains the differential equation for a pure jump process, the so called *Master* equation. It is obvious that the sample path of such a process is discontinuous. Processes involving jumps are of little relevance for this work, and will not be investigated any further.

Conversely, for drift-diffusion processes the jump probabilities become zero, resulting in the *Fokker-Planck* equation

$$\frac{\partial f(\boldsymbol{x}; t|\boldsymbol{x}_0, t_0)}{\partial t} = -\frac{\partial A_i(\boldsymbol{x}, t) f(\boldsymbol{x}; t|\boldsymbol{x}_0, t_0)}{\partial x_i} + \frac{1}{2}\frac{\partial^2 B_{ij}(\boldsymbol{x}, t) f(\boldsymbol{x}; t|\boldsymbol{x}_0, t_0)}{\partial \boldsymbol{x}_i \partial \boldsymbol{x}_j} \quad . \tag{9.5}$$

Note that albeit the resulting sampling paths are continuous, they need not be differentiable. In the case of the diffusion coefficient matrix $\mathbf{B}$ being zero, the Fokker-Planck equation decays to the *Liouville* equation, pertaining to a deterministic process, which is differentiable.

9.2 Diffusion Processes

A pure diffusion processes, where the drift coefficient vector $\boldsymbol{A}$ is zero and the diffusion coefficient matrix is the identity matrix, is referred to as a *Wiener* process $W(t)$. By setting the time-derivative of its Fokker-Planck equation to null, one can solve it for the stationary distribution which recovers a Gaussian PDF with mean $\boldsymbol{x}_0$ and variance $t - t_0$

$$f(\boldsymbol{x}; t|\boldsymbol{x}_0, t_0) = \frac{1}{\sqrt{2\pi\,(t - t_0)}} \exp\left(-\frac{1}{2}\frac{(x_i - x_{0,i})(x_i - x_{0,i})}{t - t_0}\right)$$

Since the Ornstein-Uhlenbeck process described by the Langevin equation (9.1) is a drift-diffusion process, there must exist a corresponding Fokker-Planck equation. By using the formalism for the treatment of SDE's using Itō calculus as described by Gardiner [18, Sec. 4.3.4 and Sec. 4.3.5], the drift and diffusion coefficients $A(x, t)$ and $B(x, t)$ can be determined. They are scalars for a single-valued process, resulting in

$$\frac{\partial f(x; t|x_0, t_0)}{\partial t} = \frac{1}{\tau}\frac{\partial f(x; t|x_0, t_0)}{\partial x} + \frac{\sigma^2}{\tau}\frac{\partial^2 f(x; t|x_0, t_0)}{\partial x^2} \quad . \tag{9.6}$$

Comparing the coefficients of above equation with the ones in the Langevin equation (9.1), it can be observed that the drift coefficient is the same, while the diffusion coefficient appears squared in the Fokker-Planck equation. Indeed, it is generally true for all Langevin-type equations of the form of (9.2) that

$$A_i(x,t) = a_i(x,t) \quad \text{and} \quad B_{ij}(x,t) = b_{ik}(x,t)b_{kj}(x,t) \quad . \tag{9.7}$$

Consequently, it now is clear that for every Fokker-Plank equation there exists an equivalent stochastic particle system and vice versa. Solving either of them is consistent with solving the other system.

Comparing (9.5) with the modelled JPDF transport equation (7.20), it follows that the latter is a Fokker-Planck equation evolving in the high-dimensional $\boldsymbol{X} - \boldsymbol{V} - \boldsymbol{\psi}$ space and consequently it must be possible to construct a stochastic system that solves it. This is the goal of the following sections.

9.3 The Lagrangian Stochastic Particle System

9.3.1 Relating the Lagrangian to the Eulerian PDF

In order to use a Lagrangian solution method for the JPDF transport equation, an equivalent Lagrangian description for the Eulerian JPDF transport equation must be found. In a Lagrangian description, a flow variable Q^+ is related to its Eulerian counterpart through

$$Q^+(\boldsymbol{X}_0, t) = Q(\boldsymbol{X}^+(\boldsymbol{X}_0, t), t) \quad ,$$

where $\boldsymbol{X}^+(\boldsymbol{X}_0, t)$ denotes the position of a particle with initial position $\boldsymbol{X}_0$. The temporal change of a Lagrangian flow variable corresponds to the convective derivative of the Eulerian variable, which can easily be shown by applying the chain rule and the fact that ${}^{\mathrm{d}\boldsymbol{X}^+}/_{\mathrm{d}t} = \boldsymbol{U}$

$$\frac{\mathrm{d}Q^+(\boldsymbol{X}_0, t)}{\mathrm{d}t} = \left[\frac{\partial Q(\boldsymbol{X}, t)}{\partial t} + U_i \frac{\partial Q(\boldsymbol{X}, t)}{\partial x_i}\right]_{\boldsymbol{X}=\boldsymbol{X}^+(\boldsymbol{X}_0,t)} \quad .$$

The Lagrangian PDF can be understood as the PDF of particles originating at a certain location in phase space $\boldsymbol{x}_0$, $\boldsymbol{V}_0$ and $\boldsymbol{\Psi}_0$ at t_0, i.e. $f_L(\boldsymbol{V}, \boldsymbol{\psi}, \boldsymbol{x}; t | \boldsymbol{V}_0, \boldsymbol{\psi}_0, \boldsymbol{x}_0, t_0)$. The alternative interpretation is that of a transition probability for a particle to evolve from the state $\boldsymbol{x}_0$, $\boldsymbol{V}_0$ and $\boldsymbol{\Psi}_0$ at t_0 to the state $\boldsymbol{V}$, $\boldsymbol{\psi}$ and $\boldsymbol{x}$ at time t.

The Eulerian PDF, on the other hand, can be viewed as the PDF generated by all particles in space and time governed by a stochastic process with the PDF $f(\boldsymbol{V}, \boldsymbol{\psi})$, i.e. $f(\boldsymbol{V}, \boldsymbol{\psi}|\boldsymbol{x}, t)$. With of

$$f(\boldsymbol{V}, \boldsymbol{\psi}; \boldsymbol{x}, t) = f(\boldsymbol{V}, \boldsymbol{\psi}|\boldsymbol{x}, t) \quad ,$$

using the definitions of a conditional PDF, the link between the Eulerian and Lagrangian description is established as

$$\begin{aligned} f(\boldsymbol{V}, \boldsymbol{\psi}; \boldsymbol{x}, t) &= \frac{f(\boldsymbol{V}, \boldsymbol{\psi}, \boldsymbol{x}; t)}{f(\boldsymbol{x}; t)} \\ &= \frac{1}{f(\boldsymbol{x}; t)} \iiint_{-\infty}^{+\infty} f(\boldsymbol{V}, \boldsymbol{\psi}, \boldsymbol{x}, \boldsymbol{V}_0, \boldsymbol{\psi}_0, \boldsymbol{x}_0; t) \mathrm{d}\boldsymbol{V}_0 \mathrm{d}\boldsymbol{\psi}_0 \mathrm{d}\boldsymbol{x}_0 \\ &= \frac{1}{f(\boldsymbol{x}; t)} \iiint_{-\infty}^{+\infty} f_L(\boldsymbol{V}, \boldsymbol{\psi}, \boldsymbol{x}|\boldsymbol{V}_0, \boldsymbol{\psi}_0, \boldsymbol{x}_0; t) \\ &\qquad \times f(\boldsymbol{V}_0, \psi_0, \boldsymbol{x}_0) \mathrm{d}\boldsymbol{V}_0 \mathrm{d}\boldsymbol{\psi}_0 \mathrm{d}\boldsymbol{x}_0 \quad . \end{aligned} \tag{9.8}$$

Hence, the Eulerian PDF is obtained by integration of the product of the Lagrangian PDF f_L with the initial state PDF $f(\boldsymbol{V}_0, \boldsymbol{\psi}_0, \boldsymbol{x}_0)$ over all initial states and dividing by the particle distribution PDF $f(\boldsymbol{x}, t)$. A similar expression for the MDF can be obtained by multiplication with $Mf(\boldsymbol{x}; t)$, M being the constant, total mass in the flow domain:

$$\begin{aligned} Mf(\boldsymbol{V}, \boldsymbol{\psi}; \boldsymbol{x}, t) f(\boldsymbol{x}; t) &= Mf(\boldsymbol{V}, \boldsymbol{\psi}, \boldsymbol{x}; t) = \mathcal{F}(\boldsymbol{V}, \boldsymbol{\psi}, \boldsymbol{x}; t) \\ &= \iiint_{-\infty}^{+\infty} f_L(\boldsymbol{V}, \boldsymbol{\psi}, \boldsymbol{x}|\boldsymbol{V}_0, \boldsymbol{\psi}_0, \boldsymbol{x}_0; t) Mf(\boldsymbol{V}_0, \boldsymbol{\psi}_0, \boldsymbol{x}_0) \mathrm{d}\boldsymbol{V}_0 \mathrm{d}\boldsymbol{\psi}_0 \mathrm{d}\boldsymbol{x}_0 \\ &= \iiint_{-\infty}^{+\infty} f_L(\boldsymbol{V}, \boldsymbol{\psi}, \boldsymbol{x}|\boldsymbol{V}_0, \boldsymbol{\psi}_0, \boldsymbol{x}_0; t) \mathcal{F}(\boldsymbol{V}_0, \boldsymbol{\psi}_0, \boldsymbol{x}_0) \mathrm{d}\boldsymbol{V}_0 \mathrm{d}\boldsymbol{\psi}_0 \mathrm{d}\boldsymbol{x}_0 \quad . \end{aligned} \tag{9.9}$$

The first step once again uses the definition of the conditional PDF and the second and fourth steps use the fact that M is the normalisation factor of the MDF.

9.3.2 Stochastic Lagrangian PDF Method

In this section, the stochastic process used to solve the Lagrangian PDF transport equation is established. Note that $f_L(\boldsymbol{V}, \boldsymbol{\psi}; \boldsymbol{x}, t)$ being the Lagrangian PDF of the real, physical flow and $f^*(\boldsymbol{V}, \boldsymbol{\psi}; \boldsymbol{x}, t)$ the calculated

one, here it is merely required that the stochastic system to be developed is consistent with the real system in a statistical sense, i.e. that

$$f^*(\boldsymbol{V}, \boldsymbol{\psi}; \boldsymbol{x}, t) = f_L(\boldsymbol{V}, \boldsymbol{\psi}; \boldsymbol{x}, t) \quad . \tag{9.10}$$

At no point is it required that the realisations of the stochastic system are equal to the real ones, which would be a much stronger requirement (see Pope [62, Sec. 4.1] and Fox [17, Sec. 6.7.2]). However, due to above relation, it is required that (9.8) holds for the calculated PDF.

In order to solve for the PDF, Lagrangian *notional* particles evolve in physical-velocity-composition space, i.e. $\boldsymbol{X}^*$, $\boldsymbol{U}^*$ and $\boldsymbol{\phi}^*$, according to stochastic processes whose corresponding Fokker-Planck equation is the desired PDF transport equation:

$$\begin{aligned} \frac{\mathrm{d}X_i^*}{\mathrm{d}t} &= U_i^* \quad , \\ \mathrm{d}U_i^* &= a_{U,i}\mathrm{d}t + b_{UU,ij}\mathrm{d}W_{U,j} + b_{U\phi,ij}\mathrm{d}W_{\phi,j} \quad \text{and} \\ \mathrm{d}\phi_\alpha^* &= a_{\phi,\alpha}\mathrm{d}t + b_{\phi U,\alpha k}\mathrm{d}W_{U,k} + b_{\phi\phi,\alpha k}\mathrm{d}W_{\phi,k} \quad . \end{aligned} \tag{9.11}$$

The goal now is to find appropriate values for the drift and diffusion coefficients $\boldsymbol{a}_U$, $\boldsymbol{a}_\phi$, $\mathbf{b}_{UU}$, $\mathbf{b}_{U\phi}$, $\mathbf{b}_{\phi U}$ and $\mathbf{b}_{\phi\phi}$, respectively.

Fortunately, for most applications many of these coefficients are null, such as $\mathbf{b}_{U\phi}$ and $\mathbf{b}_{\phi U}$. Using the theory from Section 9.2, the corresponding Fokker-Planck equation for the Eulerian or Lagrangian PDF's can be obtained. Finding appropriate models for the unclosed terms, however, is quite challenging. Either one searches closure at the Lagrangian level, requiring that $f_L^* = f_L$, or much more difficult, at the Eulerian level, where $f^* = f$ must hold. The former, working directly at the level of the stochastic equations, is the more intuitive choice which will be pursued here.

The motion of the notional particles can be modelled with the conditional fluxes using (7.3):

$$\begin{aligned} \frac{\mathrm{d}X_i^*}{\mathrm{d}t} &= U_i^* \quad , \\ \frac{\mathrm{d}U_i^*}{\mathrm{d}t} &= \langle A_i | \boldsymbol{U}^*, \boldsymbol{\phi}^*, \boldsymbol{X}^* \rangle + \mathcal{N}_{U,i}(t) \quad \text{and} \\ \frac{\mathrm{d}\phi_\alpha^*}{\mathrm{d}t} &= \langle \Theta_\alpha | \boldsymbol{U}^*, \boldsymbol{\phi}^*, \boldsymbol{X}^* \rangle + \mathcal{N}_{\phi,\alpha}(t) \quad , \end{aligned} \tag{9.12}$$

where $\mathcal{N}_U$ and $\mathcal{N}_\phi$ are noise terms which control the evolution of the joint PDF. Comparing above equations to (9.11), it is clear that

$$\begin{aligned} \left(\langle A_i | \boldsymbol{U}^*, \boldsymbol{X}^* \rangle + \mathcal{N}_{U,i}(t)\right)\mathrm{d}t &= a_{U,i}\mathrm{d}t + b_{UU,ij}\mathrm{d}W_{U,j} \quad , \\ \left(\langle \Theta_\alpha | \boldsymbol{U}^*, \boldsymbol{\phi}^*, \boldsymbol{X}^* \rangle + \mathcal{N}_{\phi,\alpha}(t)\right)\mathrm{d}t &= a_{\phi,\alpha}\mathrm{d}t + b_{\phi\phi,\alpha k}\mathrm{d}W_{\phi,k} \quad , \end{aligned}$$

and the main goal of Lagrangian PDF modelling is to find the coefficients for the right-hand side of above equations that are consistent with the conditional fluxes.

The conditional acceleration is decomposed into the mean and fluctuating part resulting in

$$\langle A_i | \boldsymbol{U}^*, \boldsymbol{X}^* \rangle = \frac{1}{\langle \rho \rangle} \frac{\partial \left\langle \tau_{ij}^* | \boldsymbol{X}^* \right\rangle}{\partial x_j} (\boldsymbol{X}^*, t) - \frac{1}{\langle \rho \rangle} \frac{\partial P}{\partial x_i} (\boldsymbol{X}^*, t) + \langle A_i' | \boldsymbol{U}^*, \boldsymbol{X}^* \rangle$$

where the mean fields have been replaced by the conditional equivalents based on the particle quantities; $\langle \boldsymbol{\tau}^* | X^* \rangle$ and P are the mean *particle-stress* and *particle-pressure* fields, respectively. For high-Reynolds number flows, the mean viscous stress is negligible and dropped. However, the particle-pressure field must be computed from the particles, e.g. by solving a Poisson equation for incompressible flows. Notice that since this field is computed from the means of the stochastic field and the second derivatives thereof, the inevitable noise present in the fields poses a major challenge when applying a Lagrangian stochastic particle method.

This is the main reason why Jenny et al. [31] proposed a hybrid method, where the mean conditional particle fields are replaced by their Eulerian counterparts obtained from a RANS simulation running alongside with the particle simulation. Such a scheme significantly reduces stochastic noise and the bias error, also greatly improving convergence. This work will use a similar scheme, hence the particle-pressure field will not be further investigated here. The interested reader is referred to Pope [62] and Fox [17] instead.

The remaining term in the conditional acceleration to be modelled is the fluctuating part, i.e.

$$(\langle A_i' | \boldsymbol{U}^*, \boldsymbol{X}^* \rangle + \mathcal{N}_{U,i}(t))\, \mathrm{d}t = a_{U,i}' \mathrm{d}t + b_{UU,ij} \mathrm{d}W_{U,j} \quad .$$

The development of appropriate models that ensure consistency with the Reynolds stress transport equation is beyond the scope of this work. Here, the Lagrangian SLM model is used. The drift coefficient is then given by

$$a_{U,i}' = -\left(\frac{1}{2} + \frac{3}{4} C_0\right) \frac{1}{\tau} (U_i^* - \widetilde{U}_i)$$

and the diffusion coefficient follows as

$$b_{UU,ij} = \sqrt{C_0 \frac{k}{\tau}} \delta_{ij} \quad ,$$

where τ is a turbulent time scale.

There are quite a few possibilities to model the time scale τ, such as (a) using the mean dissipation rate and turbulent kinetic energy ($\tau = {}^{k}/_{\varepsilon}$, the approach taken in this work); (b) using the particle kinetic energy instead ($\tau = {}^{k^*}/_{\varepsilon}$); (c) using a dedicated stochastic process for the particle turbulence frequency ω^*, see Jayesh and Pope [30], Van Slooten et al. [81] and Jenny et al. [31]. When using the latter approach, it is usually best to use the conditional mean defined by

$$\Omega = C_\Omega \frac{\langle \rho^* \omega^* | \, \omega^* \geqslant \widetilde{\omega} \rangle}{\langle \rho \rangle}$$

as the inverse time scale in order to account for intermittency effects. C_Ω is a model constant. It is important that the averaging operation in above equation is *not* equivalent to the Favre average due to the conditioning.

Using the IEM mixing model to close the conditional diffusion term, the drift and diffusion coefficients are

$$a_{\phi,\alpha} = \frac{1}{\langle\rho\rangle}\frac{\partial}{\partial x_i}\left(\langle\rho\rangle\, \Gamma_\alpha \frac{\partial \widetilde{\phi^*_\alpha | \boldsymbol{X}*}}{\partial x_i}\right) + \dot{\omega}_\alpha(\boldsymbol{\phi}^*) - \frac{1}{2} C_\phi \left(\phi^*_\alpha - \widetilde{\phi_\alpha | \boldsymbol{X}^*}\right)\frac{1}{\tau}$$

and

$$b_{\phi\phi,\alpha\beta} = 0 \quad ,$$

respectively. Neglecting the mean diffusion term and modelling the time scale $\tau = {}^{\varepsilon}/_{k}$, in summary the particle evolution equations read

$$\mathrm{d}X^*_i = U^*_i \mathrm{d}t \tag{9.13}$$

$$\mathrm{d}U^*_i = -\frac{1}{\langle\rho\rangle}\frac{\partial \langle p \rangle}{\partial x_i}\mathrm{d}t - \left(\frac{1}{2} + \frac{3}{4}C_0\right)\frac{\varepsilon}{k}(U^*_i - \widetilde{U}_i)\mathrm{d}t + \sqrt{C_0 \varepsilon}\ \mathrm{d}W_i \tag{9.14}$$

$$\frac{\mathrm{d}\phi^*_\alpha}{\mathrm{d}t} = -\frac{1}{2} C_\phi \left(\phi^*_\alpha - \widetilde{\phi}_\alpha\right)\frac{\varepsilon}{k} + \dot{\omega}_\alpha(\boldsymbol{\phi}^*) \quad . \tag{9.15}$$

9.3.3 Consistency Requirement

Defining the discrete mass density function $\mathcal{F}_N(\boldsymbol{V}, \boldsymbol{\psi}, \boldsymbol{x})$ generated by N notional particles with individual statistical masses m summing up to M as (Pope [62, Sec. 3.4])

$$\mathcal{F}_N(\boldsymbol{V}, \boldsymbol{\psi}, \boldsymbol{x}) \equiv \frac{1}{N}\sum_{n=1}^{N} \delta(\boldsymbol{V} - \boldsymbol{U}^{(n)})\delta(\boldsymbol{\psi} - \boldsymbol{\phi}^{(n)})\delta(\boldsymbol{x} - \boldsymbol{X}^{(n)}) m^{(n)} \quad ,$$

its expectation can be written as

$$\langle \mathcal{F}_N(\boldsymbol{V}, \boldsymbol{\psi}, \boldsymbol{x}; t) \rangle = \frac{1}{N} \sum_{n=1}^{N} \left\langle \delta(\boldsymbol{V} - \boldsymbol{U}^{(n)}) \delta(\boldsymbol{\psi} - \boldsymbol{\phi}^{(n)}) \delta(\boldsymbol{x} - \boldsymbol{X}^{(n)}) m^{(n)} \right\rangle \quad ,$$

or, alternatively, for any n with $1 \leqslant n \leqslant N$

$$\langle \mathcal{F}_N(\boldsymbol{V}, \boldsymbol{\psi}, \boldsymbol{x}; t) \rangle = \left\langle \delta(\boldsymbol{V} - \boldsymbol{U}^{(n)}) \delta(\boldsymbol{\psi} - \boldsymbol{\phi}^{(n)}) \delta(\boldsymbol{x} - \boldsymbol{X}^{(n)}) m^{(n)} \right\rangle \quad .$$

It is required that this expectation is equal to the mass density function $\mathcal{F}$:

$$\langle \mathcal{F}_N(\boldsymbol{V}, \boldsymbol{\psi}, \boldsymbol{x}; t) \rangle = \mathcal{F}(\boldsymbol{V}, \boldsymbol{\psi}, \boldsymbol{x}; t) \quad .$$

With $\widetilde{f}^*(\boldsymbol{x}; t)$ denoting the probability density of a notional particle with mass m^* being at location $\boldsymbol{X}^* = \boldsymbol{x}$ at time t (i.e. the density-weighted position PDF of the notional particles), then

$$\iint_{-\infty}^{+\infty} \langle \mathcal{F}_N \rangle (\boldsymbol{V}, \boldsymbol{\psi}, \boldsymbol{x}; t) \mathrm{d}\boldsymbol{V} \mathrm{d}\boldsymbol{\psi} = M \widetilde{f}^*(\boldsymbol{x}; t) = \langle \rho \rangle (\boldsymbol{x}) \tag{9.16}$$

must hold. From this relation it becomes clear that in order to be consistent, the particle mass density $q = M\widetilde{f}^*(\boldsymbol{x}; t)$ must be equal to the mean fluid density $\langle \rho \rangle$. This very fundamental requirement is often very much underappreciated; in fact many, researchers using Lagrangian PDF methods ignore it.

9.4 Accuracy and Efficiency Considerations

Assuming that the flow is solved by a stand-alone Monte-Carlo particle method using an ensemble of N particles, a time step size Δt, a grid with the resolution $M^3 = M_x \times M_y \times M_z$ in a domain with an extent of $\mathcal{L}_x \times \mathcal{L}_y \times \mathcal{L}_z$, the number of particles per cell is $N_{\mathrm{pc}} = {}^{N}/_{M^3}$ and a measure for the cell spacing is given by $h = \sqrt[3]{\mathcal{L}_x \mathcal{L}_y \mathcal{L}_z}/M$. Due to M and N_{pc} being finite and Δt not approaching 0, numerical errors exist in the solution that need to be understood and reduced as far as possible. Since in this work only weak convergence is required, i.e. that the Lagrangian MDF $\mathcal{F}_L^*$ represented by the N particles converges to the modelled MDF $\mathcal{F}_L$, any mean quantity estimated from $\mathcal{F}_L^*$ must converge to the actual mean. The numerical error of this mean quantity is composed of the statistical, bias and discretisation errors, where the latter two are deterministic and the statistical error is

random in nature. Since the total error is random, the convergence should be treated in a mean-square sense [88]. Denoting the mean estimate of the quantity Q at a given point in space and time from the particle ensemble of size N_{pc} with identical particle weights, with a grid of size M^3 and a time step size Δt as $\langle Q^* \rangle_{N_{\text{pc}},M,\Delta t}$ and the actual mean as $\langle Q \rangle$, the error reads

$$\epsilon = \langle Q^* \rangle_{N_{\text{pc}},M,\Delta t} - \langle Q \rangle = \epsilon_S + \epsilon_B + \epsilon_D \quad ,$$

ϵ_S being the random statistical error and ϵ_B and ϵ_D the bias and discretisation errors, respectively.

The simple ensemble mean

$$\langle Q^* \rangle_{N_{\text{pc}},M,\Delta t} = \frac{1}{N_{\text{pc}}} \sum_{i=1}^{N_{\text{pc}}} Q(\boldsymbol{U}^{*(i)}, \boldsymbol{\phi}^{*(i)}) \quad ,$$

$\boldsymbol{U}^{*(i)}$ and $\boldsymbol{\phi}^{*(i)}$ being the velocity and composition of particle i, is for independent and identically distributed samples an unbiased estimator. However, for finite N_{pc}, it is a random variable subject to fluctuations; the statistical error. According to the central limit theorem (Section 3.5) the statistical error tends to zero with $\sqrt{N_{\text{pc}}}$.

Since the statistical error in the mean estimation enters more or less directly (depending on the numerical solution scheme) the stochastic equations (9.14) and (9.15), Xu and Pope [87] showed that the independence of the samples is no longer given and that a bias error is introduced, given by

$$\epsilon_B = \left\langle \langle Q^* \rangle_{N_{\text{pc}},M,\Delta t} \right\rangle - \langle Q^* \rangle_{\infty,M,\Delta t} \quad .$$

Here, $\langle Q^* \rangle_{\infty,M,\Delta t} \equiv \lim_{N_{\text{pc}} \to \infty} \langle Q \rangle_{N_{\text{pc}},M,\Delta t}$. Pope [65] and Xu and Pope [87] showed that the bias error scales as $1/N_{\text{pc}}$.

Finally, the discretisation error is identified as

$$\epsilon_D = \langle Q^* \rangle_{\infty,M,\Delta t} - \langle Q \rangle \quad ,$$

consisting both of the spatial discretisation error and the time-integration error.

9.4.1 Reduction of Noise and Bias

Time Averaging: For stationary problems, *time-averaging* can be employed to reduce the noise. Suppose that after reaching steady state at T_s,

the solution is averaged over a time span T_{avg}, or $N_{\text{avg}} = {}^{T_{\text{avg}}}/_{\Delta t}$ iterations as

$$\left\langle \langle Q^* \rangle_{N_{\text{pc}},M,\Delta t} \right\rangle_{T_{\text{avg}}} \equiv \frac{1}{T_{\text{avg}}} \int_{T_s}^{T_s+T_{\text{avg}}} \langle Q^* \rangle_{N_{\text{pc}},M,\Delta t}(t')\mathrm{d}t' \quad .$$

Defining the reduction factor $\mathcal{R}_Q$ of the statistical noise as

$$\mathcal{R}_Q \equiv \frac{\text{Var}\left(\left\langle \langle Q^* \rangle_{N_{\text{pc}},M,\Delta t} \right\rangle_{T_{\text{avg}}}\right)}{\text{Var}\left(\langle Q^* \rangle_{N_{\text{pc}},M,\Delta t}\right)} \quad ,$$

where Var indicates the variance operator, Xu and Pope [87] employed a time series analysis [68] to show that

$$R_Q^2\left(T_{\text{avg}}\right) = \frac{2}{T_{\text{avg}}} \int_0^{T_{\text{avg}}} \left(1 - \frac{|t'|}{T_{\text{avg}}}\right) \varrho(t')\mathrm{d}t' \quad .$$

Here, $\varrho(t)$ is the autocorrelation function. For large T_{avg} it can be shown that

$$R_Q \sim \sqrt{\frac{2\tau}{T_{\text{avg}}}}$$

with the time scale

$$\tau \equiv \int_0^{\infty} \varrho(t')\mathrm{d}t' \quad .$$

This indicates that time averaging over a long time reduces the statistical error by a factor of $\sqrt{{}^{2\tau}/_{T_{\text{avg}}}}$. This corresponds to increasing the number of particles per cell N_{pc} by a factor of ${}^{T_{\text{avg}}}/_{2\tau}$. Xu and Pope [88] demonstrated that the time scale τ relates to the turbulence frequency as

$$\tau \approx \frac{C_\tau}{\widetilde{\omega}} \quad ,$$

where C_τ is a constant of about 0.1.

Hybrid RANS/JPDF Methods: Jenny et al. [31] proposed a method that significantly reduces the bias error by combining the stochastic particle simulation with a deterministic RANS simulation, resulting in a so-called *hybrid FV/JPDF* scheme. In such a scheme the mean quantities (velocity and

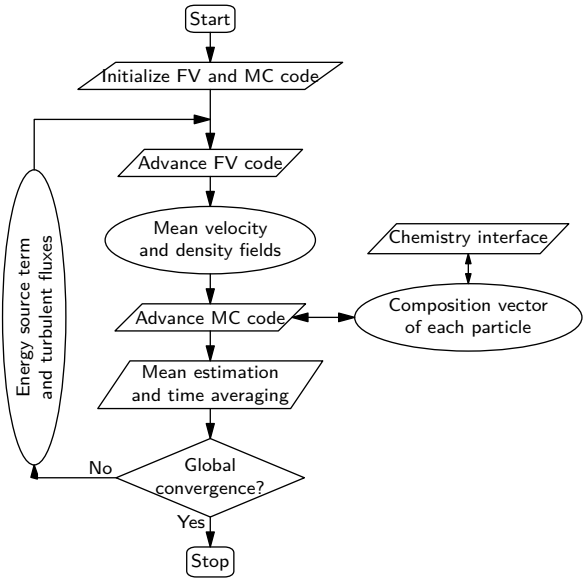

Figure 9.1 – Schematic of the hybrid coupling proposed by Jenny et al. [31].

pressure) in the particle evolution equations (9.11) are not computed from the particles, but are rather taken from the RANS simulation. Conversely, Jenny et al. used the energy source term and the Reynolds stress tensor computed from the particles in the RANS simulation. This coupling is illustrated in Figure 9.1. This hybrid coupling significantly reduces the noise in the mean fields used by the stochastic equations, thus greatly reducing the bias error.

9.4.2 Internal Consistency

With a hybrid scheme as described in the previous section, some flow quantities are bound to be computed redundantly. In the case of Jenny et al. [31], the particle system is only solved for the fluctuating velocity components $\boldsymbol{u}''^{*}$. The energy, however, is computed using both, RANS and the particle system, where the chemical source term was being obtained and then transferred to the RANS simulation. Further, (9.16) requires that the particle mass density is also consistent with the mean flow density. Finally, from the definition of the Favre average it is required that the mean particle

fluctuating velocities be null, i.e. $\widetilde{\boldsymbol{u}''^*|\boldsymbol{x}} = \mathbf{0}$ everywhere.

On the level of the modelled equations all quantities are consistent by construction. However, due to numerical errors, deviations between the redundant fields occur, which must be corrected using appropriate schemes.

9.4.3 Hybrid Coupling

For hybrid schemes there is no obvious or natural choice for the coupling method. Jenny et al. [31] proposed a coupling by feeding the mean velocity field from the FV solver to the Lagrangian Monte-Carlo particle solver, which in return provides the energy source term and Reynolds stress tensor to the FV part. The turbulent time scale is calculated in the particle code using a stochastic process as described in Section 9.3.2. Jenny et al. chose to reformulate the JPDF transport equation for the fluctuating velocity $\boldsymbol{u}''$ instead of the full velocity $\boldsymbol{U}$, resulting in the stochastic particle velocity evolution equation

$$\mathrm{d}u_i''^* = \frac{1}{\langle\rho\rangle}\frac{\partial\,\langle\rho\rangle\,\widetilde{u_i''u_j''}}{\partial x_j}\mathrm{d}t - u_j''^*\frac{\partial\widetilde{U}_i}{\partial x_j}\mathrm{d}t - \left(\frac{1}{2}+\frac{3}{4}C_0\right)\Omega u_i''^*\mathrm{d}t + \sqrt{C_0 k\Omega}\,\mathrm{d}W_i\ .$$

This formulation has the advantage of avoiding the ambiguity between the mean velocities computed by the FV and MC parts, respectively. Further, opposed to the evolution equation for the full velocity (9.14), the mean pressure gradient does not appear in above equation. Instead the divergence of the Reynolds stress tensor and the mean velocity are required. In the light of the bias error analysis, the former is problematic, especially as it is computed from the fluctuating particle velocities. Also, experience has shown that the noise in the Reynolds stress tensor as computed by the particles can be quite disruptive for the FV Reynolds averaged equations solver, which relies on smooth Reynolds stress fields.

Jenny et al. used a *tight* coupling between the FV and MC methods, i.e. the two parts were executed in lock-step. This would be a requirement if the solver was intended for transient problems. For steady state problems, though, a *loose* coupling between the FV and MC methods can be more effective. Since in general time-averaging is applied for the MC code, the FV part converges much faster, making it undesirable to execute it that often. Further, the tight coupling introduces a lot of noise into the FV system, thus reducing its stability. Experience has shown that a loose coupling scheme where the FV and MC parts iterate individually for a variable number of

steps before switching to the other part, can enhance the stability of the solver, increase the convergence rate and reduce the computational cost.

9.4.4 Efficiency Enhancements

When using a MC particle method there are several issues that can arise and negatively impact either performance or accuracy. Each cell should contain roughly the same number of particles throughout the simulation. If there are too few particles, the statistical noise increases. Too many particles, on the other hand, incur additional computation cost. This is why a *particle number control* scheme can be beneficial.

Another problem impacting the statistical error and the efficiency is that the particle time step restriction imposed by the CFL criterion can lead to very small time steps. That is, very fast particles and very small cells determine the time step size. Unfortunately, both of these conditions frequently occur in the same region of the computational domain; in jet flames, where one wants to resolve the shear layer between the fast jet and the slow co-flow, for example. The required simulated time until convergence, however, is not determined by the fast fluid but by the slow parts in the flow domain. In order to obtain good statistics, several flow-through times and time-averaging times should be simulated. E.g. for jet flames, where the co-flow velocity can be one or two orders of magnitude slower than the jet velocity, the long required simulation time, together with the small time step due to the fast jet, results in a very large number of time-steps until convergence is reached. Another factor negatively influencing the bias error is that in cells with a very small Courant number, the same particles are sampled many times, resulting in very bad statistics. For steady state solutions, a *local* or *asynchronous* time-stepping scheme can be employed, where the time step size is determined by a local CFL criterion, greatly enhancing the computational efficiency and reducing the bias error of the simulation.

10 Hybrid FV/JPDF Algorithm

Here, the final hybrid algorithm used for this work is described. Using the finite volume solver, the steady state Reynolds averaged equations for variable density flows are solved. The Reynolds stresses are closed using the standard $k - \varepsilon$ model. The Monte-Carlo solver evolves the stochastic particles according to the evolution equations outlined before. The simplified Langevin Model (SLM) [63] is used to model the conditional acceleration term and the IEM model closes the molecular mixing term. Chemistry is treated using the standard laminar flamelet model. The turbulent time scales are provided by the RANS model, i.e. no separate particle process is involved. The mean pressure gradient and the mean velocity are also taken from the Reynolds averaged solution. Conversely, the mean density required by the RANS solver is computed from the particle solution. Since the particles in the JPDF simulation carry velocity and temperature information, no additional energy transport equation in the RANS solver is necessary. The coupling between the RANS and JPDF solvers is loose, i.e. the RANS solver performs N_{FV} steps, before the algorithm switches to the JPDF solver, which then advances by N_{MC} iterations. N_{FV} and N_{MC} are parameters of the algorithm. A schematic of the loose hybrid coupling scheme is shown in Figure 10.1. Appropriate schemes to ensure consistency between the mean and the particle mass density, the Reynolds averaged mean and the PDF mean velocity and between the Reynolds stress tensors obtained from the RANS model and the particle velocities are used.

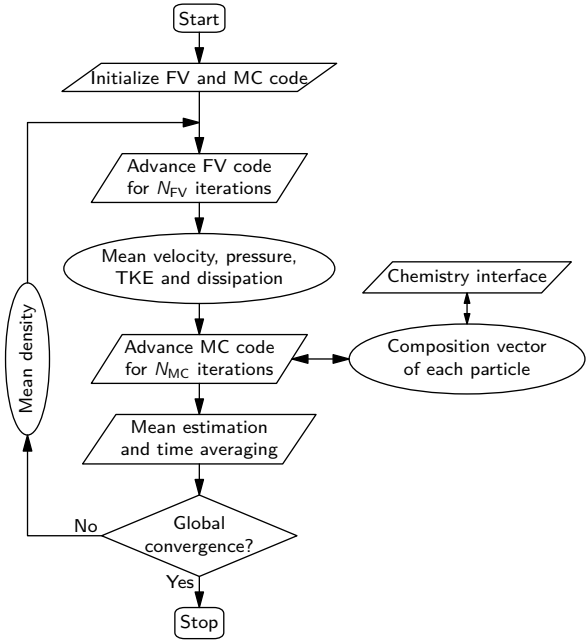

Figure 10.1 – Schematic of the hybrid coupling scheme.

10.1 Reynolds Averaged Equations

The Reynolds averaged equations for steady state and variable density flows are given by

$$\frac{\partial \langle\rho\rangle \widetilde{U}_i}{\partial x_i} = 0 \quad , \tag{10.1}$$

$$\frac{\partial \langle\rho\rangle \widetilde{U}_j \widetilde{U}_i + \langle p\rangle \delta_{ij} - \langle\tau_{ij}\rangle}{\partial x_j} = -\frac{\partial \langle\rho\rangle \widetilde{u_i'' u_j''}}{\partial x_j} \quad , \tag{10.2}$$

where the continuity equation reduced to a compatibility condition, similar to the incompressible flow case. Since for atmospheric flames at low Mach numbers the energy contained in the pressure waves is small, a low Mach number approximation can be used; everywhere, except in the momentum equation, the pressure is replaced by the thermodynamic pressure p_0. This filters out the pressure waves, removing the time-step limitation induced by the speed of sound. In order to find an equation for the pressure for the use in the momentum equation, a Poisson equation is derived for variable density flows. Here, this is done on the semi-discretisation of the momentum equation

$$a_p U_{p,i} + \sum a_n U_{n,i} = -\frac{\delta p}{\delta x_i} \quad ,$$

where $a_p \boldsymbol{U}_p$ and $a_n \boldsymbol{U}_n$ are the contributions from the point itself and the neighbours obtained from the discretisation of the mean convective term $\nabla(\langle\rho\rangle \widetilde{\boldsymbol{U}}\widetilde{\boldsymbol{U}})$ and the divergence of the effective stress tensor. $\delta/\delta x_i$ stands for the discrete differential operator. Defining

$$H_i \equiv -\sum a_n U_{n,i} \quad ,$$

the semi-discrete momentum equation reads

$$a_p U_{p,i} = H_i - \frac{\delta p}{\delta x_i} \quad .$$

Re-arranging the equation and multiplying it with $\langle\rho\rangle$, the following is obtained:

$$\langle\rho\rangle U_{p,i} = \frac{\langle\rho\rangle H_i}{a_p} - \frac{\langle\rho\rangle}{a_p}\frac{\delta p}{\delta x_i} \quad .$$

Taking the divergence of above equation and defining $\boldsymbol{\varphi} \equiv \langle\rho\rangle \boldsymbol{H}/a_p$ as the momentum flux field at the cell faces, the discrete Poisson equation for the pressure reads

$$\frac{\delta}{\delta x_i}\left(\frac{\langle\rho\rangle}{a_p}\frac{\delta p}{\delta x_i}\right) = \frac{\delta \varphi_i}{\delta x_i} \quad . \tag{10.3}$$

The momentum and pressure equations are solved using a standard SIMPLE algorithm, see Ferziger and Perić [16, Sec. 7.3.4].

10.2 JPDF Algorithm

The stochastic particle system evolves according to equations (9.13), (9.14) and (9.15), reproduced here for reference:

$$\begin{aligned}
\mathrm{d}X_i^* &= U_i^* \mathrm{d}t \\
\mathrm{d}U_i^* &= -\frac{1}{\langle\rho\rangle}\frac{\partial\langle p\rangle}{\partial x_i}\mathrm{d}t - \left(\frac{1}{2}+\frac{3}{4}C_0\right)\frac{\varepsilon}{k}(U_i^*-\widetilde{U}_i)\mathrm{d}t + \sqrt{C_0\varepsilon}\,\mathrm{d}W_i \\
\frac{\mathrm{d}\phi_\alpha^*}{\mathrm{d}t} &= -\frac{1}{2}C_\phi\left(\phi_\alpha^*-\widetilde{\phi}_\alpha\right)\frac{\varepsilon}{k}+\dot{\omega}_\alpha(\boldsymbol{\phi}^*) \quad .
\end{aligned}$$

Here, the inverse time scale is modelled as

$$\Omega = \frac{\varepsilon}{k} \quad .$$

Chemistry is modelled by a steady flamelet model, as described in Section 8.4.2, where the thermodynamic state is tabulated in a preprocessing step as a function of the mixture fraction z and the scalar dissipation rate χ. Hence, the only transported scalar property of the particles is the mixture fraction z. Being a conserved scalar, there exists no source term and the particle evolution equation for the mixture fraction reads

$$\frac{\mathrm{d}z^*}{\mathrm{d}t} = -\frac{1}{2}C_\phi\left(z^*-\widetilde{z}\right)\frac{\varepsilon}{k} \quad .$$

The scalar dissipation rate χ required for the flamelet lookup is modelled using the scale-similarity approach (7.19) as proposed by Poinsot and Veynante [61], reading

$$\chi^* = C_\chi \frac{\varepsilon}{k}\widetilde{z''^2} \quad .$$

Here, C_χ is a model constant for which a value of 6 is suggested. From the flamelet table, the particle density $\rho^*(z^*,\chi^*)$ and temperature $T^*(z^*,\chi^*)$ are retrieved from the flamelet table using bilinear interpolation.

10.3 Numerical Integration

The particle position $\boldsymbol{X}^*$ is integrated using the *mid-point rule* as described by Jenny et al. [31], achieving second order accuracy. In a first half step the

particle is moved to

$$X_i^{*(n+\frac{1}{2})} = X_i^{*(n)} + \frac{\Delta t}{2} U_i^{*(n)} \quad , \tag{10.4}$$

where n denotes the old and $n+1$ the new time level. At this stage, the velocity, mixing and flamelet models are evaluated to obtain $\boldsymbol{U}^{*(n+1)}$, $\boldsymbol{\phi}^{*(n+1)}$, $\rho^{*(n+1)}$ and $T^{*(n+1)}$. The full time step is then performed as

$$X_i^{*(n+1)} = X_i^{*(n)} + \frac{\Delta t}{2} \left(U_i^{*(n)} + U_i^{*(n+1)} \right) \quad . \tag{10.5}$$

Using

$$a \equiv - \left(\frac{1}{2} + \frac{3}{4} C_0 \right) \frac{\varepsilon}{k}$$

and

$$b_i \equiv - \frac{1}{\langle \rho \rangle} \frac{\partial \langle p \rangle}{\partial x_i} - a \widetilde{U}_i \quad ,$$

the velocity evolution equation (9.14) reads

$$\mathrm{d}U_i^* = b_i \mathrm{d}t + a U_i^* \mathrm{d}t + \sqrt{C_0 \varepsilon} \mathrm{d}W_i \quad .$$

A second order scheme, similar to the one described by Jenny et al. [31], is used to integrate the simplified Langevin model:

$$\begin{aligned} \Delta U_i &= \left(b_i + a U_i^{*(n)} \right) \Delta t + \sqrt{C_0 \varepsilon \Delta t} \xi_i \\ U_i^{*(n+1)} &= U_i^{*(n)} + \Delta U_i + \frac{1}{2} a \Delta U_i \Delta t \quad . \end{aligned}$$

The coefficients a, $\boldsymbol{b}$ and $\Delta \boldsymbol{U}$ are evaluated at the estimated midpoint $\boldsymbol{X}^{*(n+\frac{1}{2})}$ and $\boldsymbol{\xi}$ is a vector of standard normal random variables.

Last, the IEM mixing model (9.15) can be analytically integrated from $t^{(n)}$ to $t^{(n+1)}$:

$$\phi_\alpha^{*(n+1)} = \phi_\alpha^{*(n)} - \left(1.0 - e^{-C_\phi \frac{\varepsilon}{k} \Delta t} \right) \left(\phi_\alpha^{*(n)} - \widetilde{\phi}_\alpha \right) \quad .$$

In order for the scheme to be conservative, the cell-averaged values are used for the mean scalar $\widetilde{\boldsymbol{\phi}}$.

10.4 Mean Field Estimation

As described in Section 7, the mean quantities are obtained from the joint PDF by computing its moments. When using a stochastic particle system to solve for the joint PDF transport equation, a similar operation has to be defined over a discrete ensemble of notional particles. This will be described in the following.

The vector of the estimated instantaneous moments of the JPDF at time step n is given by

$$\boldsymbol{E}^{(n)} = \left[\mathcal{M}^{(n)}, \mathcal{V}^{(n)}, \mathcal{I}_i^{(n)}, \mathcal{E}_{ij}^{(n)}, \mathcal{S}_\alpha^{(n)}, \mathcal{C}_{\alpha\beta}^{(n)}\right]^T = \sum \hat{g}(\boldsymbol{X}^{*(n)}) m^{*(n)} \boldsymbol{e}^{*(n)} \quad ,$$

where $\boldsymbol{e}^*$ is the vector of the following particle-derived quantities

$$\boldsymbol{e}^* = \left[1, 1/\rho^*, U_i^*, U_i^* U_j^*, \phi_\alpha^*, \phi_\alpha^* \phi_\beta^*\right]^T \quad .$$

Here, $\hat{g}(\boldsymbol{x}^*)$ is a kernel function which in this work is chosen to be a simple top-hat function coinciding with the computational cell. Thus, the entries in $\boldsymbol{E}$ are the mass in the corresponding cell, volume, momentum, energy, mean scalar times mass and scalar covariance times mass.

To reduce the statistical error, time-averaging is used as laid out in Section 9.4.1. The time-averaged quantities are defined as

$$\boldsymbol{E}_{\text{avg}}^{(n)} \equiv \alpha \boldsymbol{E}_{\text{avg}}^{(n-1)} + (1-\alpha)\boldsymbol{E}^{(n)} \quad , \tag{10.6}$$

where $0 \leqslant \alpha < 1$ is a time-averaging parameter which should be close to unity. Here it is given by

$$\alpha \equiv \frac{1}{1 + \frac{\Delta t}{\tau_{\text{avg}} - \Delta t}} \equiv \frac{K-1}{K} \quad ,$$

where τ_{avg} is the *averaging time scale* and K is the number of time steps required to cover τ_{avg}, i.e. the fraction $\tau_{\text{avg}}/\Delta t$ expresses the averaging time scale as a number of time steps and corresponds to the time-averaging factor K defined by Jenny et al. [31]. This results in a moving time-averaging scheme with exponentially decaying weight, as can be seen when expanding (10.6) to read:

$$\boldsymbol{E}_{\text{avg}}^{(n)} = (1-\alpha)\left(\boldsymbol{E}^{(n)} + \alpha \boldsymbol{E}^{(n-1)} + \alpha^2 \boldsymbol{E}^{(n-2)} + \ldots + \alpha^n \boldsymbol{E}^{(0)}\right) \quad ,$$

The estimated, instantaneous moments of interest can then be computed

as

$$\begin{aligned}
\langle\rho\rangle &= \frac{\mathcal{M}}{\mathcal{V}} \quad , & \widetilde{U}_i^{(\mathrm{mc})} &= \frac{\mathcal{I}_i}{\mathcal{M}} \quad , \\
\widetilde{u_i'' u_j''}^{(\mathrm{mc})} &= \frac{\mathcal{E}_{ij}}{\mathcal{M}} - \widetilde{U}_i^{(\mathrm{mc})}\widetilde{U}_j^{(\mathrm{mc})} \quad , & k^{(\mathrm{mc})} &= \frac{1}{2}\widetilde{u_i'' u_i''}^{(\mathrm{mc})} \quad , \\
\widetilde{\phi}_\alpha &= \frac{\mathcal{S}_\alpha}{\mathcal{M}} \quad , & \widetilde{\phi_\alpha'' \phi_\beta''} &= \frac{\mathcal{C}_{\alpha\beta}}{\mathcal{M}} - \widetilde{\phi}_\alpha\widetilde{\phi}_\beta \quad \text{and} \\
\langle q\rangle &= \frac{\mathcal{M}}{\|\Omega\|_{\mathrm{cell}}} \quad .
\end{aligned} \tag{10.7}$$

Here, $\|\Omega\|_{\mathrm{cell}}$ is the cell volume and the fields that are redundant are distinguished from the finite volume fields with the (mc) superscript. By replacing the instantaneous vector $\boldsymbol{E}$ with $\boldsymbol{E}_{\mathrm{avg}}$, the time-averaged moments are recovered.

10.5 Internal Consistency

Jenny et al. [31] corrected the mean fluctuating velocity $\widetilde{\boldsymbol{u}''}$ by simply subtracting the time averaged deviation from every particle. Very elaborate schemes for the correction of the density and energy errors were proposed by Muradoglu et al. [52].

10.5.1 Density/Position Correction

The basic principle of position correction schemes is to compute a correction velocity $\boldsymbol{U}^c$ which is added to the particle transport such that the time averaged particle mass density q_{avg} matches the mean fluid density $\langle\rho\rangle_{\mathrm{avg}}$.

In the following, the method proposed by Muradoglu et al. [52] is presented. First, for each cell the normalised, instantaneous density error Q is computed

$$Q \equiv \frac{\langle q\rangle - \langle\rho\rangle}{\langle\rho\rangle_{\mathrm{avg}}} \quad ,$$

from which the smoothed density difference $\overline{Q}$ is computed by solving:

$$\frac{\partial\overline{Q}}{\partial t} = (\overline{Q} - Q)c\frac{U_0}{L} + fU_0 L\frac{\partial^2\overline{Q}}{\partial x_i\,\partial x_i} \quad .$$

Here, U_0 and L are velocity and length scales, and c and f are non-dimensional parameters. This is a smoothing operation both in space and

time with an averaging time scale $\tau^c_{\text{avg}} = {}^{L}/_{U_0 c}$. Further, the correction potential Φ evolves as

$$\frac{\partial \Phi}{\partial t} = b U_0^2 Q \quad ,$$

b being another non-dimensional parameter. Finally, the correction velocity is defined by

$$U_i^c = -\frac{\partial \Phi}{\partial x_i} - a U_0 L \left(\zeta \frac{\partial \overline{Q}}{\partial x_i} + (1-\zeta) \frac{\partial Q}{\partial x_i} \right)$$

with the indicator function ζ

$$\zeta = \begin{cases} 1 & \text{if } \frac{\langle q \rangle}{\langle \rho \rangle} \geqslant \epsilon_\zeta \\ 0 & \text{if } \frac{\langle q \rangle}{\langle \rho \rangle} < \epsilon_\zeta \end{cases} \quad ,$$

allowing the algorithm to react quickly when the mass density error compared to the fluid density is below a critical threshold ϵ_ζ by switching from the gradient of the smooth relative error $\overline{Q}$ to the gradient of the instantaneous relative error Q. It is required that the potential Φ reaches a steady state, in which case $Q_{\text{avg}} = 0$ and consequently $\langle q \rangle_{\text{avg}} = \langle \rho \rangle_{\text{avg}}$. Muradoglu et al. [52] applied control system analysis to find an optimal choice for the many parameters, proposing

$$\begin{aligned} L &= \frac{\Delta x}{\pi} & U_0 &= |\boldsymbol{U}|_{\max} \\ c &= \frac{1}{\pi} \frac{1}{(\text{CFL})_p N^c_{\text{avg}}} & f &= k_f c \\ b &= k_b f^2 & a &= \left(1 + \frac{b}{c^2}\right) f \end{aligned} \quad ,$$

where Δx is a representative grid spacing length and $|\boldsymbol{U}|_{\max}$ the maximum mean velocity in the computational domain. The parameters are suggested to be chosen as $k_f = 3$, $k_b = 8$, $N^c_{\text{avg}} = 20$, $(\text{CFL})_p = 0.4$ and $\epsilon_\zeta = 0.25$. The energy correction scheme is not discussed here, as it is not relevant to this work.

A simpler, local correction density scheme is used in this work. It is also based on the normalised density error Q, but using the time-averaged densities:

$$Q = \frac{\langle q \rangle_{\text{avg}} - \langle \rho \rangle_{\text{avg}}}{\langle \rho \rangle_{\text{avg}}} \quad .$$

The correction velocity is then computed as

$$U_i^c = -a\frac{\partial Q}{\partial x_i}$$

with

$$a = C_{\text{pos}} \min\left(\frac{(\text{CFL})_p^c \Delta x}{\|\frac{\partial Q}{\partial x_i}\|\Delta t}\right)\tanh(10\max(Q)) \quad ,$$

where C_{pos} and $(\text{CFL})_p^c$ are coefficients to be chosen by the user. The latter is chosen to be the same as the CFL number used for the particle evolution.

When performing the particle transport as described in Section 10.3, the correction velocity is incorporated into the particle movement by defining the effective particle velocity to be

$$U^*_{\text{eff},i} = U_i^* + U_i^c \quad .$$

10.5.2 Mean Velocity Correction

Both, the RANS and the MC parts of the hybrid scheme compute a mean velocity, i.e. $\widetilde{\boldsymbol{U}}$ and $\widetilde{\boldsymbol{U}}^{(\text{mc})}_{\text{avg}}$, respectively. To ensure they that are consistent, the particle velocities are relaxed towards the finite volume mean velocity by adding a drift term to the particle velocity evolution equation (9.14), resulting in

$$\mathrm{d}U_i^* = -\frac{1}{\langle\rho\rangle}\frac{\partial\langle p\rangle}{\partial x_i}\mathrm{d}t - \left(\frac{1}{2}+\frac{3}{4}C_0\right)\frac{\varepsilon}{k}(U_i^* - \widetilde{U}_i)\mathrm{d}t + \sqrt{C_0\varepsilon}\,\mathrm{d}W_i + \frac{\widetilde{U}_i - \widetilde{U}^{(\text{mc})}_{\text{avg},i}}{\tau_U}\mathrm{d}t \quad .$$

Here, τ_U is the drift time scale; a numerical parameter. All the mean fields are evaluated at the particle location $\boldsymbol{X}^*$. In the numerical integration, this term is applied sequentially, using an explicit forward Euler scheme.

10.5.3 Reynolds Stress Tensor Correction

Similar to the mean velocity, the Reynolds stress tensor is computed by the FV solver using a two-equations eddy-viscosity RANS model (e.g. $k-\varepsilon$), while the one obtained from the MC solver using the SLM is consistent to a Reynolds stress model using Rotta's return to isotropy model. As the

latter is more sophisticated, it is expected that the deviatoric part of the Reynolds stress tensor as computed by the SLM is more accurate than the one provided by the eddy viscosity assumption. Hence, it is undesirable to enforce full consistency of the Reynolds stress tensor; instead only agreement between the turbulent kinetic energies k and $k_{\text{avg}}^{(\text{mc})}$ is enforced. Therefore, similar as for the mean velocity correction, another drift term is added to the particle velocity evolution equation. Instead of shifting all the particle velocities to adjust the mean, here the fluctuations are scaled in order to obtain the correct TKE. The modified velocity equation, including the above defined mean velocity correction, reads

$$\begin{aligned} \mathrm{d}U_i^* = &-\frac{1}{\langle\rho\rangle}\frac{\partial\langle p\rangle}{\partial x_i}\mathrm{d}t - \left(\frac{1}{2}+\frac{3}{4}C_0\right)\frac{\varepsilon}{k}(U_i^*-\widetilde{U}_i)\mathrm{d}t \\ &+\sqrt{C_0\varepsilon}\;\mathrm{d}W_i + \frac{\widetilde{U}_i-\widetilde{U}_{\text{avg},i}^{(\text{mc})}}{\tau_U}\mathrm{d}t + \frac{U_i^*-\widetilde{U}_i}{\tau_k}\left(\sqrt{\frac{k}{k_{\text{avg}}^{(mc)}}}-1\right)\mathrm{d}t \quad , \end{aligned}$$

where τ_k is a model parameter. Like the mean velocity correction term, the correction term for the TKE is also applied sequentially using the explicit forward Euler scheme. Notice that it proved to be more robust to use the cell averaged values for k and $k_{\text{avg}}^{(\text{mc})}$, instead of interpolated ones.

10.5.4 Particle Distribution Correction

When using a density correction algorithm as described in Section 10.5.1, due to interpolation errors, artificial particle patterns can emerge, if the correction is too strong. To make the algorithm more robust against such artefacts, one can argue that the exact location of a particle inside a computational cell is of little importance. This is justified by the fact that all particles inside a cell are considered to be part of the same ensemble, and when mean quantities are estimated a top-hat filter is used. Based on this reasoning, a little numerical dispersion, or jitter, is added to the particle tracking, generating uncertainty in the particle destination position proportional to the travelling distance and the cell size. The modified particle evolution equation reads

$$\mathrm{d}X_i^* = U_i^*\mathrm{d}t + \sqrt{C_{\text{diff}}h\|\boldsymbol{U}^*\|}\mathrm{d}W_i \quad ,$$

where h is a length a scale that should be proportional to the local cell size (e.g. $\sqrt[3]{\|\Omega\|_{\text{cell}}}$) and C_{diff} is a model coefficient in the order of 0.01.

10.6 Efficiency Enhancements

10.6.1 Particle Number Control

As described above, actively controlling the number of particles can be crucial for the accuracy and performance of the MC solver. Fox [17, Sec. 7.3.1] proposes an algorithm that controls the particle weight distribution in every cell by *cloning* heavy and *eliminating* light particles. For every cell I, the estimated mean particle mass is computed as

$$\overline{m}_I \equiv \frac{1}{N_I} \sum_{n=1}^{N_I} m^{(n)} \quad ,$$

where N_I is the number of particles in the cell I and $m^{(n)}$ is the mass of the nth particle in that cell. If $m^{(k)} \geqslant 2\overline{m}_I$ for any $k \in \{1, \ldots, N_I\}$. Then, particle k is cloned, where the children have half of the parent's mass. Thus the total mass in the cell is preserved. If, on the other hand, $m^{(k)} \leqslant \overline{m}_I/2$, then another particle k^* is selected randomly and eliminated with the probability $m^{(k)}/\left(m^{(k)}+m^{(k^*)}\right)$, otherwise particle k^* is eliminated. The mass of the surviving particle is set to $m^{(k)} + m^{(k^*)}$, hence also preserving the total mass inside the cell.

In order to control the number of particles inside a cell, Subramaniam and Haworth [79] proposed a similar method. Particles are cloned, if the number of particles inside the cell drops below a prescribed threshold using the same cloning method as described by Fox. If the particle number exceeds an upper threshold, however, the probability of a particle being eliminated is scaled inversely with its weight, hence preferring light particles. The weight of the deleted particle is evenly distributed amongst the remaining particles instead of giving it to a single other particle as is done in the method proposed by Fox.

Both of the proposed particle elimination or clustering methods have the disadvantage of degrading the representation of the underlying PDF as they are biased to removing particles with a small weight, hence reducing the number of samples in that part of the PDF. The original reasoning behind this preferential deletion is that the removal of a light particle has less impact on the PDF than the removal of a heavy particle. However, in cases where the particle weight is correlated with other particle properties, such as the momentum or composition, this scheme can lead to bad statistics because of the biased removal of particles. An exemplary situation where this arises is a jet flame in which the particles from the fuel jet are substantially lighter

than the particles from the surrounding co-flow due to the small cell size and lower fuel density.

While the cloning of particles is unproblematic, reducing the number of particles is more challenging. For a more systematic review of particle number control methods, refer to Haworth [23] and Hack [20].

10.6.2 A Novel Particle Number Control Algorithm

The goal of the proposed method is that in the particle number reduction algorithm the full joint PDF is preserved in a statistical sense. This is achieved by ensuring that the joint PDF of the removed particles corresponds to the full joint PDF in the grid cell. At the same time it is attempted to minimise the impact of the particle removal by preferably deleting a light subset of particles that fulfils the criterion of preserving the JPDF.

When the number of particles N_l in a given cell falls below a threshold value $C_{\mathsf{min}} N_{\mathsf{pc}}$, N_{pc} being the desired number of particles per cell, the $N_{\mathsf{pc}} - N_l$ heaviest particles are cloned by creating an identical twin, dividing the mass of the new and old particle by a factor of two. C_{min} is a coefficient in $[0, 1)$, where 0 indicates that no cloning should be performed. This procedure is analogous to the ones discussed by Haworth [23] and Hack [20]. However, in contrast to most popular implementations of the cloning algorithm, here the newly created particle is placed randomly with a uniform distribution within the computational cell in which the original particle is located.

If the number of particles N_l exceeds the upper threshold $C_{\mathsf{max}} N_{\mathsf{pc}}$, two populations A and B of particles are formed, where the probability of a particle being picked is $2^{(N_l - N_{\mathsf{pc}})}/N_l$ and the assignment to population A or B is equally probable. In average, both populations have a size of $N_l - N_{\mathsf{pc}}$ particles with mass m_A and m_B, respectively. With a probability $m_B/(m_A+m_B)$, population A is eliminated, otherwise population B is deleted. The masses of the particles in the surviving population are then scaled up to compensate for the mass lost by deleting the other set. Since both populations are representative sub-samples of the full joint histogram in the cell, all moments are preserved in a mean sense. Similar to the cloning algorithm, C_{max} is a coefficient in $(1, \infty)$, where $C_{\mathsf{max}} \to \infty$ indicates that no particle elimination should be performed.

10.6.3 Local Particle Time-Stepping

Möbus et al. [48] proposed a method for local time stepping that was later

mathematically motivated by Muradoglu and Pope [51]. The goal is to use a local CFL criterion to determine the particle time step size, while still solving for the same steady-state MDF. Here, an abbreviated and simplified derivation for this particular local time-stepping approach is given.

Assuming that the local particle time increment $\mathrm{d}\theta$ is related to the global time increment $\mathrm{d}t$ through

$$\mathrm{d}\theta(\boldsymbol{x}, t) = \eta(\boldsymbol{x}, t)\mathrm{d}t \quad ,$$

where η is a strictly positive non-dimensional field, the stochastic particle evolution equations read (using $\boldsymbol{A}$, B and $\boldsymbol{C}$ for the drift and diffusion coefficients for brevity)

$$\begin{aligned}
\mathrm{d}X_i^* &= U_i^* \eta \, \mathrm{d}t \\
\mathrm{d}U_i^* &= A_i \eta \, \mathrm{d}t + \sqrt{2\eta B} \, \mathrm{d}W_i \\
\mathrm{d}\phi_\alpha^* &= C_\alpha \eta \, \mathrm{d}t \quad ,
\end{aligned}$$

resulting in the transport equation for the modified MDF $\mathcal{F}^{\mathrm{mod}}$

$$\frac{\partial \mathcal{F}^{\mathrm{mod}}}{\partial t} = -\frac{\partial V_i \eta \mathcal{F}^{\mathrm{mod}}}{\partial x_i} - \frac{\partial A_i \eta \mathcal{F}^{\mathrm{mod}}}{\partial V_i} - \frac{\partial C_i \eta \mathcal{F}^{\mathrm{mod}}}{\partial \psi_i} + \frac{\partial^2 B \eta \mathcal{F}^{\mathrm{mod}}}{\partial V_i \partial V_i} \quad .$$

It is easy to see that in steady state on obtains the same solution of $\eta\mathcal{F}^{\mathrm{mod}}$ as for $\mathcal{F}$ when no local time stepping is applied. Since we are interested in the latter, one has to consider

$$\mathcal{F} = \eta \mathcal{F}^{\mathrm{mod}} = \langle \eta m \delta(\boldsymbol{U} - \boldsymbol{V}) \delta(\boldsymbol{\phi} - \boldsymbol{\psi}) \delta(\boldsymbol{X} - \boldsymbol{x}) \rangle$$

as the relevant steady state solution.

Muradoglu and Pope [51] choose $\eta(\boldsymbol{x}, t)$ to be a function of a local CFL criterion. Assuming a Gaussian velocity distribution, the maximum particle velocity is estimated as

$$U_{\mathrm{max},i} = |\widetilde{U}_i| + 2u_i' \quad ,$$

including roughly 95% of all possible velocities according to the 68–95–99.7 rule[3]. Together with an estimation of the grid spacing $\Delta \boldsymbol{x}$ and CFL

[3] Also known as the three-sigma rule, stating that for a Gaussian distribution 68% of the samples lie within one standard deviation from the mean, 95% within two standard deviations, and 99.7% within three standard deviations

conditions for the velocity, C_U, and the turbulence frequency, C_Ω, the time step for each cell is computed as

$$\Delta t(\boldsymbol{x}, t) = \min\left(\frac{C_U U_{\max,1}}{\Delta x_1}, \frac{C_U U_{\max,2}}{\Delta x_2}, \frac{C_U U_{\max,3}}{\Delta x_3}, \frac{C_\Omega}{\Omega}\right) \quad .$$

$\Delta t_{\min}$ is defined to be the smallest Δt in the whole domain and $\Delta t_{\max} = \kappa \Delta t_{\min}$ the largest permissible time step. The local time-stepping parameter is then given by

$$\eta(\boldsymbol{x}, t) = \frac{\min(\Delta t_{\max}, \Delta t)}{\Delta t_{\min}} \quad , \tag{10.8}$$

whereas the values 0.4, 0.2 and 20 are suggested for C_U, C_Ω and κ, respectively.

10.7 Boundary Conditions

When performing a particle Monte-Carlo simulation, appropriate boundary conditions for the particles must be specified. Most commonly used are the *inflow*, *outflow*, *slip* or *no-flux* and *symmetry* boundary conditions. The first two occur when the mean velocity vector has a component normal to the wall. If it points into the domain, it is a *inflow* boundary and a *outflow* boundary otherwise.

If the mean velocity vector is parallel to the wall, the boundary is a so called *slip* or *no-flux* boundary. If, in addition, its wall-normal gradient is also zero at the wall, it is a so called *symmetry* condition. For *no-slip* walls, i.e. real, solid walls with adhesion, the velocity vector at the boundary must be null. This kind of wall is not discussed here, as its treatment poses significant modelling challenges with respect to the damping of the velocity fluctuations and since it is not relevant to the flow scenarios considered in this work.

10.7.1 Slip and Symmetry Wall

This type of boundary conditions is easiest to treat, as both can be considered as an impermeable wall where the resulting net-flux is zero. It can be implemented by simply reflecting the particles at such boundaries, as is illustrated in Figure 10.2.

The particle velocity $\hat{\boldsymbol{U}}^*$ after the collision is given by the reflection about the wall-normal vector, i.e. the Householder reflection

$$\hat{U}_i^* = (\delta_{ij} - 2 n_i n_j)\, U_j^* \quad , \tag{10.9}$$

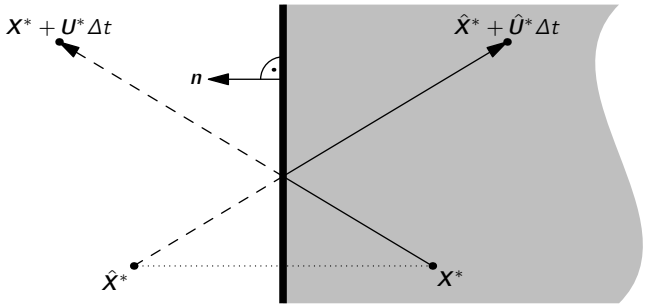

Figure 10.2 – Reflection of a particle at a slip or symmetry wall. The shaded area indicates the flow domain and the thick vertical line the wall. $\hat{\boldsymbol{X}}^*$ and $\hat{\boldsymbol{U}}^*$ represent the reflected particle position and velocity, respectively. $\boldsymbol{n}$ is the wall-normal vector.

$\boldsymbol{n}$ being the wall normal unit-vector pointing out of the domain and $\boldsymbol{U}^*$ the particle velocity before the reflection.

10.7.2 Outflow Boundary

For the purpose of this discussion, only the wall-normal components of all velocities and coordinates are considered, as indicated by the lack of a subscript.

Fox [17] treats outflow boundaries by just deleting all particles that leave the domain. However, this assumption ignores particles that enter the domain through the outflow boundary due to their counter-flow fluctuating velocity, as noted by Meyer and Jenny [46]. The wall-normal mean velocity at the outflow boundary x_b is given by

$$\widetilde{U|_{x_b}} = \int_{-\infty}^{+\infty} V f_U \mathrm{d}V = \int_{-\infty}^{0} V f_U \mathrm{d}V + \int_{0}^{\infty} V f_U \mathrm{d}V \quad ,$$

where f_U is the Eulerian mass weighted wall-normal-velocity PDF. The first integral in the second step of above equation corresponds to the contribution of the particles entering the domain through the outflow boundary. In the wall-normal system it is negative and by ignoring it, as Fox proposes, the resulting mean velocity would be too high, which leads to a net mass loss. The error is small, if the velocity standard deviation $u''|_{x_b}$ is small compared to the mean velocity $\widetilde{U|_{x_b}}$, i.e. if the flow is dominated by mean convection.

Meyer and Jenny [46] proposed a method for a consistent outflow boundary treatment. Considering the case where $\widetilde{U|\,x_b} \to 0$, the outflow boundary can be considered to be a slip wall, reflecting all particles that hit it. This is justified because in order to preserve mass, momentum and energy, every particle that leaves the domain through the boundary must be matched by another particle that enters the domain. The properties of this „inflowing" particle must correspond to the properties of the „outflowing"one, but reflected at a wall moving with the mean flow velocity $\widetilde{U|\,x_b} > 0$. For the following explanations a moving wall with position $x_0 = x_b - \widetilde{U|\,x_b}\Delta t$ at t_0 is considered.

There are three scenarios that need to be discussed when implementing this method:

1. $x^* > x_0$: The particle is located behind the moving wall. Irrespective of its velocity, it will be pushed out of the domain by the moving wall during the time interval $(t_0, t_0 + \Delta t)$. Hence it can be deleted.

2. $x^* < x_0 \wedge U^* < \widetilde{U|\,x_b}$: The particle does not interact with the boundary and stays inside the domain.

3. $x^* < x_0 \wedge (x^* + U^*\Delta t > x_b)$: The particle is in front of the moving wall and hits it during the time interval $[t_0, t_0 + \Delta t]$. In this case the particle needs to be reflected.

Note that in the last case, the reflection can easily be implemented by reflecting the particle at the stationary wall, updating the particle velocity at $t + \Delta t$ as if the particle had been reflected at the moving wall, i.e.

$$\hat{U}^* = -U^* + 2\widetilde{U|\,x_b}$$

as illustrated in Figure 10.3.

10.7.3 Inflow Boundary

There are many proposed methods for treating the inflow boundary in particle Monte-Carlo algorithms. Fox [17] proposes a method where every time step M particles are fed into the domain such that the mass is conserved, i.e.

$$\Delta m_{\text{in}} = \langle\rho\rangle_{\text{in}} S_{\text{in}} \widetilde{U}_{\text{in}} \Delta t \quad ,$$

where $\langle\rho\rangle_{\text{in}}$ is the density of the inflowing fluid, S_{in} the surface area of the inflow boundary, $\widetilde{U}_{\text{in}}$ the mean wall-normal velocity of the inflowing fluid

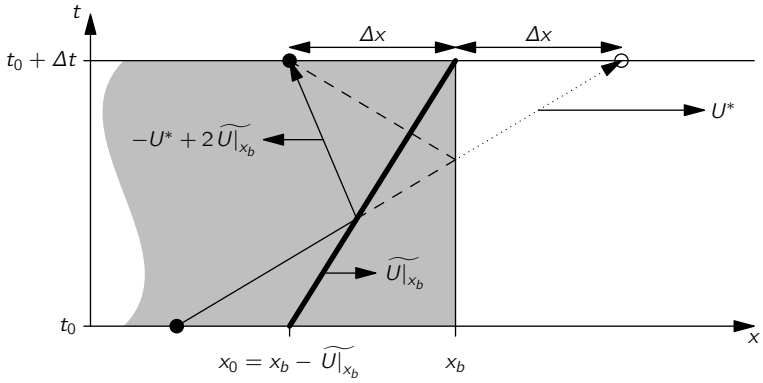

Figure 10.3 – Reflection of a particle at the moving-wall outflow boundary. The shaded area indicates the flow domain, the thick line the moving wall (inspired by Meyer and Jenny [46]).

and Δt the time step size. The N particles that would leave the domain through the inflow boundary due to their fluctuating velocities are just being reflected as if the boundary was a slip wall. This algorithm preserves mass, however, for joint velocity-composition methods, the correct mean velocity is not recovered in the case of non-zero fluctuating velocities, as Meyer and Jenny [46] point out. Assuming equal weights for all the particles and that the M particles fed into the system have the indices $1, \ldots, M$ and that the N reflected particles have the indices $M+1, \ldots, M+N$, the mean velocity at the boundary x_b is estimated as

$$\frac{1}{2N+M}\left(\sum_{n=1}^{M} U_i^{*(n)} + \sum_{n=M+1}^{M+N} U_i^{*(n)} + \sum_{n=M+1}^{M+N}\left(-U_i^{*(n)}\right)\right) = \frac{M}{2N+M}\widetilde{U}_{i,\text{in}} \ ,$$

indicating that the correct mean velocity is only recovered iff either M or N is zero. These conditions correspond to $\widetilde{U}_i/\widetilde{u_i''^2} = 0$ and $\widetilde{u_i''^2}/\widetilde{U}_i = 0$ for all $i \in \{1, 2, 3\}$, respectively.

Ghost Layers: Another method is to use a so-called *ghost layer*, a single layer of cells outside the inflow boundary. Every time-step these ghost cells are populated with M particles such that the desired inflow density is recovered. Their velocities are sampled from a prescribed PDF, e.g. a Gaussian distribution with a mean equal to $\widetilde{\boldsymbol{U}}_{\text{in}}$ and covariances honouring

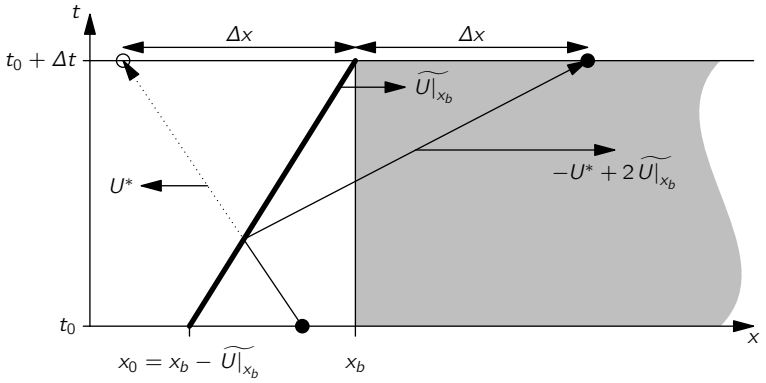

Figure 10.4 – Illustration of the ghost layer at an inflow boundary. The shaded area indicates the flow domain and the thick line the moving boundary (inspired by Meyer and Jenny [46]).

the Reynolds stress tensor at the inflow boundary. The particles then evolve for a single time-step; some leaving the ghost layer and entering the computational domain, others leaving the domain, entering the ghost layer. After the time-step all particles inside the ghost layers are deleted, before it is newly populated.

While this method works in general, it has a major drawback when it comes to unstructured meshes where ghost layers are a cumbersome concept at best and might not even be applicable inside the given framework of a simulation code. Also note that this method truncates the long tail of the velocity PDF, since it ignores very fast particles even further upstream of the ghost layer. This truncation obviously can be controlled by the thickness of the ghost layer and the time step size.

Meyer and Jenny [46] proposed a method to overcome the deficiency of the method put forward by Fox [17]. Their proposal is to reflect particles leaving the domain through the inflow boundary at a moving wall, analogously to the treatment of outflow boundaries described in Section 10.7.2. In order to account for wall-parallel velocity gradients, the velocity of the particle can be re-sampled from the desired boundary velocity PDF upon reflection. Refer to [46] for the details on velocity re-sampling. The drawback of this method is that it requires a ghost layer in which the moving wall propagates, making it equally unsuitable for unstructured meshes as the ghost-layer method is.

10.7.4 A Novel Boundary PDF Inflow Condition

In the following a method is presented that guarantees the correctness of the wall-normal velocity PDF.

Let $\widetilde{f}_U(V; x, t)$ denote the desired wall-normal one-point, one-time velocity distribution at the inflow boundary, U being the random variable for the wall-normal velocity and V the corresponding sample-space variable. Its mass-density function (MDF) is then given by $\mathcal{F}_U = \langle\rho\rangle \widetilde{f}_U$. Considering that fast particles are more likely to enter the domain than slower ones, the PDF of the particles entering the domain through the inflow boundary reads as follows

$$g_U = \begin{cases} \frac{V}{Q} f_U & \text{if } V > 0 \\ 0 & \text{else.} \end{cases} \quad , \tag{10.10}$$

Here, Q is a constant factor to ensure the normalisation property of the PDF:

$$Q = \int_0^\infty V f_U \mathrm{d}V \quad .$$

The corresponding velocity MDF of the particles entering the domain is then given by $\mathcal{G}_U = \langle\rho\rangle\, g_U$. For a mean velocity $\widetilde{U}_{\mathsf{in}} = 1\ {}^{\mathsf{m}}/_{\mathsf{s}}$ and a RMS fluctuation velocity of $u'_{\mathsf{in}} = 1{}^{\mathsf{m}}/_{\mathsf{s}}$, the shape of this PDF is displayed in Figure 10.5.

The mass flow rate across the inflow boundary is

$$\begin{aligned} \langle\rho\rangle_{\mathsf{in}}\, \widetilde{U}_{\mathsf{in}} &= \int_{-\infty}^0 V \mathcal{F}_U \mathrm{d}V + \int_0^\infty V \mathcal{F}_U \mathrm{d}V \\ &= \int_{-\infty}^0 V \mathcal{F}_U \mathrm{d}V + \langle\rho\rangle\, Q \quad , \end{aligned} \tag{10.11}$$

where the first integral accounts for the fluid flowing out of the domain and the second for the inflowing fluid. Using a Monte-Carlo PDF method, the first integral can be treated by deleting the particles that collide with the boundary. The second integral is less straight forward to treat appropriately. Given the desired velocity distribution f_U, the density $\langle\rho\rangle_{\mathsf{in}}$, the adjacent volume $\|\Omega\|$, the boundary area S_{in}, the desired number of particles per cell N_{pc} and the time step size Δt, particles have to be generated such that the mass flux and the velocity distribution are exactly reproduced.

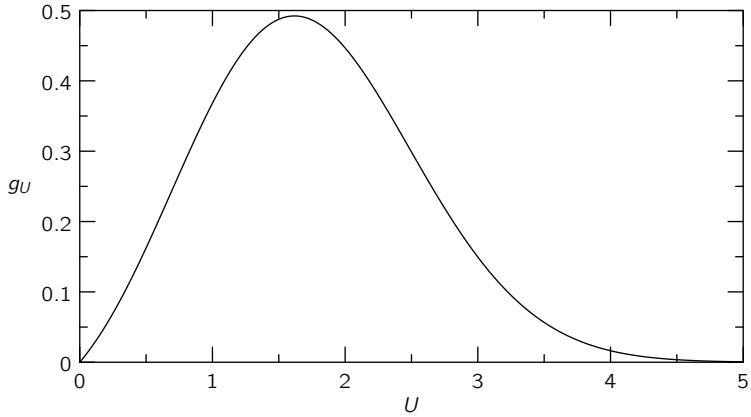

Figure 10.5 – The inflow velocity PDF for a Gaussian velocity distribution with $\widetilde{U}_{\text{in}} = 1\ {}^{\text{m}}/_{\text{s}}$ and $u'_{\text{in}} = 1\ {}^{\text{m}}/_{\text{s}}$.

The mass and the number of particles that have to be fed into the domain every time-step is determined by the mean mass flux entering the domain and the desired number N_{pc} of particles in the domain. The mean mass flux entering the domain through the inflow boundary with area S is

$$\dot{m}^+ = S_{\text{in}} \int_0^\infty V \mathcal{F}_U \mathrm{d}V \quad . \tag{10.12}$$

The mass of every particle entering the domain can then be defined as

$$m_p = \frac{\|\Omega\|}{N_{\text{pc}}} \int_{-\infty}^{+\infty} \mathcal{F}_U \mathrm{d}V = \frac{\langle\rho\rangle_{\text{in}} \|\Omega\|}{N_{\text{pc}}} \quad . \tag{10.13}$$

It follows that the mean number flux of the particles entering the domain is

$$\dot{N}^+ = \frac{\dot{m}^+}{m_p} \quad . \tag{10.14}$$

Consequently, the average number of particles with mass m_p entering the domain during a time step Δt is

$$\Delta N^+ = \frac{\dot{m}^+ \Delta t}{m_p} = N_{\text{pc}} \frac{\dot{m}^+ \Delta t}{\langle\rho\rangle_{\text{in}} \|\Omega\|} \quad . \tag{10.15}$$

Note that ΔN^+ will not be an integer number in general and special care has to be taken to treat this correctly. The naïve approach would be to round ΔN^+ up to the next integer, $\lceil \Delta N^+ \rceil$, and adjust the particle masses accordingly as $m^* = m_p {}^{\Delta N^+}/_{\lceil \Delta N^+ \rceil}$. Despite ensuring the correct mass flux and velocity PDF, such a scheme would result in a particle-number flux that is too high. In case of low mean velocities, small cell face area S_{in} or very small time steps, ΔN^+ can be close to zero, in which case far too many, very light particles will virtually be flooding the domain.

A more thought-through method is to fulfil the mass and particle number fluxes only in a statistical, mean sense. Using this approach, the number of particles entering the domain is given by

$$\Delta \hat{N}^+ = \begin{cases} \lceil \Delta N^+ \rceil & \text{if} \quad \xi < \Delta N^+ - \lfloor \Delta N^+ \rfloor \\ \lfloor \Delta N^+ \rfloor & \text{else,} \end{cases} \tag{10.16}$$

where ξ is a uniformly distributed random number in $[0, 1)$. Taking the expectation of above expression one sees that it amounts to

$$\begin{aligned} \left\langle \lfloor \Delta N^+ \rfloor + \xi \middle| \, \xi < \Delta N^+ - \lfloor \Delta N^+ \rfloor \right\rangle &= \lfloor \Delta N^+ \rfloor + \left\langle \xi \middle| \, \xi < \Delta N^+ - \lfloor \Delta N^+ \rfloor \right\rangle \\ &= \lfloor \Delta N^+ \rfloor + \Delta N^+ - \lfloor \Delta N^+ \rfloor \\ &= \Delta N^+ \quad , \end{aligned}$$

recovering the desired particle number flux, and hence also the mass flux. Algorithm 1 outlines a possible implementation.

Random numbers from the inflow boundary velocity-PDF g_U can be generated using one of the well known acceptance-rejection methods, such as the Metropolis-Hastings algorithm [22]. The inversion method cannot be used in a straight-forward manner since the cumulative density function (CDF) of g_U cannot be inverted analytically in general. To overcome this problem, numerical inversion can be used; e.g. using the Newton-Raphson method, less than ten iterations are usually sufficient for achieving high accuracy, if f_U is a Gaussian PDF.

Local Time-Stepping: When using a local particle time-stepping scheme, the MDF from which the particle velocities are sampled needs to be adapted. The new MDF can be determined by requiring that the statistical moments be preserved with respect to global time-stepping:

$$\widetilde{U^\alpha} = \frac{\int_{-\infty}^{+\infty} V^\alpha \eta \mathcal{F}_U^{\text{mod}} \mathrm{d}V}{\int_{-\infty}^{+\infty} \eta \mathcal{F}_U^{\text{mod}} \mathrm{d}V} \overset{!}{=} \frac{\int_{-\infty}^{+\infty} V^\alpha \mathcal{F}_U \mathrm{d}V}{\int_{-\infty}^{+\infty} \mathcal{F}_U \mathrm{d}V} \tag{10.17}$$

Algorithm 1 Ensure the correct mass and particle number fluxes at the inflow boundary.

$Q \leftarrow \int_0^\infty V f_U \mathrm{d}V$
$m_p \leftarrow \frac{\langle\rho\rangle_{\mathrm{in}} \|\Omega\|}{N_{\mathrm{pc}}}$ {from (10.13)}
$\Delta N^+ \leftarrow \frac{S_{\mathrm{in}}\langle\rho\rangle Q \Delta t}{m_p}$ {from (10.15)}
for $t = t_0$ **to** t_{end} **do**
  if $\xi < \Delta N^+ - \lfloor \Delta N^+ \rfloor$ **then** {from (10.16)}
    $\Delta \hat{N}^+ \leftarrow \lceil \Delta N^+ \rceil$
  else
    $\Delta \hat{N}^+ \leftarrow \lfloor \Delta N^+ \rfloor$
  end if
  for $i = 1$ **to** $\Delta \hat{N}^+$ **do**
    Generate new particle with wall normal velocity $U^* \sim g_U$ and $m^* = m_p$
  end for
  $t \leftarrow t + \Delta t$
end for

for every choice of $\alpha \in \mathbb{N}^0$. The only possible choice fulfilling this requirement (if η is considered to be possibly a function of V) is

$$\mathcal{F}_U^{\mathrm{mod}} = \frac{1}{\eta}\mathcal{F}_U \quad . \tag{10.18}$$

The velocity boundary PDF is then

$$g_U^{\mathrm{mod}} = \begin{cases} \frac{\eta V}{Q} f_U^{\mathrm{mod}} & \text{if } V > 0 \\ 0 & \text{else,} \end{cases} \quad , \tag{10.19}$$

since now the probability of a particle entering the domain also scales with η. As can be seen by substituting (10.18) into (10.19), $g_U^{\mathrm{mod}} \equiv g_U$ and consequently nothing needs to be changed for the boundary velocity PDF. Also, the mean mass flux created by the particles entering the domain in case of local time-stepping is straight-forward to express

$$\dot{m}^{+\mathrm{mod}} = S \int_0^\infty \eta V \mathcal{F}_U^{\mathrm{mod}} \mathrm{d}V = \dot{m}^+ \quad .$$

The average number of particles entering the domain over a time-interval Δt is not as easy to obtain, since it would be desirable to inversely scale

particle masses with the individual local time-stepping parameter: $m^* = {}^{m_p}/_{\eta^*}$. It would be possible to fulfil the mass-balance by computing the mean local time-stepping parameter of the particles entering the domain

$$\widetilde{\eta^+} = \frac{\int_0^\infty \eta\eta\mathcal{F}_U^{\text{mod}}\mathrm{d}V}{\int_{-\infty}^{+\infty} \eta\mathcal{F}_U^{\text{mod}}\mathrm{d}V} = \frac{\int_0^\infty \eta\mathcal{F}_U\mathrm{d}V}{\int_{-\infty}^{+\infty} \mathcal{F}_U\mathrm{d}V} \quad .$$

However, the integral in the numerator is difficult to evaluate as it depends both on the prescribed inflow MDF $\mathcal{F}_U$ and the local time-stepping function η. From the implementation point of view it would be preferable if it was possible to select them independently, without requiring the user to provide the solution in analytical form or having to perform the integration numerically.

The simpler and more flexible alternative is to adapt the algorithm presented above for the particle number flux when using global time-stepping, to the local time-stepping scenario. Here, particles are generated with mass $m^* = {}^{m_p}/_{\eta^*}$, until their cumulative mass m_{gen} exceeds the desired mass $\dot{m}^+\Delta t$. The last particle that has been generated, having the mass m^*_{last}, is now deleted with a probability of $(m_{\text{gen}} - \dot{m}\Delta t)/m^*_{\text{last}}$. The procedure is shown in algorithm 2.

This algorithm also preserves both, the mass and particle number fluxes, and is also applicable to the global time-stepping case, since $\eta = 1$ and consequently $m^* = m_p$.

Discussion: Above described method using the boundary velocity PDF for the treatment of the inflow boundary, despite being elegant, has a severe drawback. It is not straight forward to enforce the desired correlation coefficients between the wall-normal and wall-parallel velocity components. I.e. it is difficult to specify the off-diagonal components of the Reynolds stress tensor in the wall-normal coordinate system. In the present work this particular issue is not resolved.

10.8 Quasi Planar and Axi-Symmetric Flows

A flow scenario where there exists a statistically homogeneous direction, i.e. in which all mean gradients vanish and vectorial quantities are null, is called a quasi-planar flow. In such a setting great efficiency gains can be achieved in the Monte-Carlo simulation as the transport in the homogeneous direction can be ignored, although the particles in general do have a velocity

Algorithm 2 Ensure the correct mass and particle number fluxes at the inflow boundary when using local time-stepping.

$Q \leftarrow \int_0^\infty V f_U \mathrm{d}V$
$m_p \leftarrow \frac{\langle\rho\rangle_{\mathsf{in}} \|\Omega\|}{N_{\mathsf{pc}}}$ {from (10.13)}
$m_{\mathsf{in}} \leftarrow S_{\mathsf{in}} \langle\rho\rangle Q \Delta t$ {from (10.12)}
for $t = t_0$ **to** t_{end} **do**
  $m_{\mathsf{gen}} \leftarrow 0$
  loop
    Sample U^* from g_U
    Compute η^*
    $m^* \leftarrow \frac{m_p}{\eta^*}$
    if $m_{\mathsf{gen}} + m^* < m_{\mathsf{in}}$ **or** $\xi < \frac{m_{\mathsf{gen}} - m_{\mathsf{in}}}{m^*}$ **then**
      Generate particle with wall-normal velocity U^* and mass m^*
    end if
    if $m_{\mathsf{gen}} + m^* \geqslant m_{\mathsf{in}}$ **then**
      break
    else
      $m_{\mathsf{gen}} \leftarrow m_{\mathsf{gen}} + m^*$
    end if
  end loop
  $t \leftarrow t + \Delta t$
end for

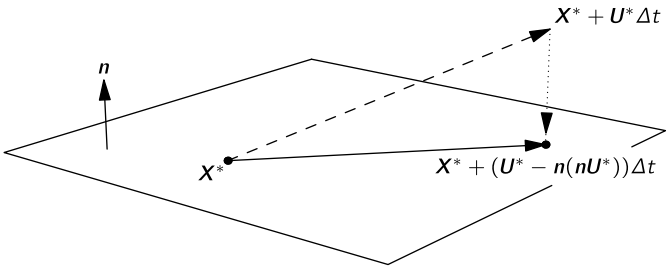

Figure 10.6 – Illustration of the particle motion in a quasi-planar flow.

component in that direction. However, since the direction is homogeneous, the particle positions in that direction are of no consequence.

The situation is more involved for a quasi axisymmetric flow where there exists a symmetry axis and the homogeneous direction is the circumferential direction. If all the flow and particle transport equations were transformed into a cylindrical coordinate system, treatment of this special case would be as simple as for the quasi planar case. However, such a transformation introduces additional terms in the evolution equations, greatly complicating the implementation which is then special-cased for exactly this flow pattern. Rather than modifying the evolution equations for the particle properties, it is easier to treat this flow pattern in the particle transport. In this flow scenario, all planes containing the symmetry axis are statistically equivalent, and it is sufficient to perform the simulation only in one of these planes. Since, however, the particle velocities are Cartesian, the movement in the out-of-plane direction results in an increase of the distance of the particle from the symmetry axis, which must be accounted for. Since every out-of-plane movement positions the particle in another, statistically equivalent plane containing the symmetry axis, the particle can simply be *rotated* back into the original plane, as illustrated in Figure 10.7.

Another complication is that a particle represents a volume that is proportional to its distance from the axis. This has to be considered when initialising the particle mass at the beginning of the simulation and at the inflow boundaries, but also when performing the mean field estimation.

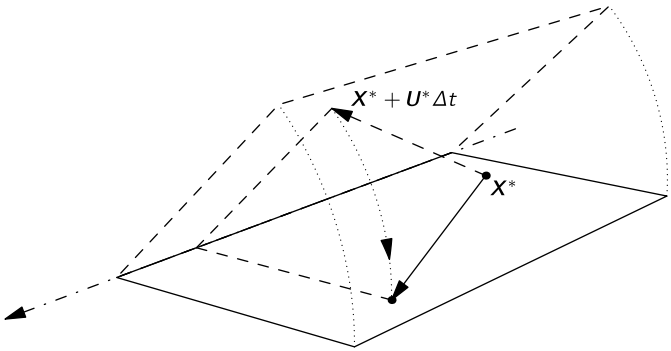

Figure 10.7 – Illustration of the quasi axisymmetric particle motion.

11 Implementation in OpenFOAM

11.1 Motivation

The framework in which the hybrid FV/JPDF algorithm described in the previous sections has been implemented is OpenFOAM®, a very comprehensive and powerful tool-kit for the solution of partial differential equations using the finite volume method. Written in well-structured, object-oriented C++, it is very extensible, featuring many *extension hooks*, where user-supplied classes can be loaded without the need for recompilation. OpenFOAM is able to run efficiently on massively parallel super computers using the MPI standard. It contains a large number of run-time selectable discretisation and time-integration schemes, ranging from simple upwinding to flux limited, NVD and TVD schemes. For time integration, second order implicit, Crank-Nicholson and first order local implicit schemes are available. In terms of solvers for the linear equation systems, OpenFOAM comes with preconditioned (bi-)conjugate gradients (PCG/PBiCG) and generalised algebraic-geometric multigrid (GAMG), supplemented by a multitude of preconditioners (e.g. diagonal incomplete Cholesky (DIC), diagonal incomplete LU) and smooth solvers, such as Gauss-Seidel or DIC.

OpenFOAM is a fully unstructured code, supporting almost arbitrary (convex) cell shapes, thus allowing for great geometric flexibility. Quasi planar and quasi axisymmetric flows are treated via a single layer (or wedge, in the axisymmetric case) of three dimensional cells, applying special boundary conditions in the homogeneous direction.

A large number of boundary conditions is available for all kinds of physical problems. New boundary conditions can be created by the user and loaded at run-time, without having to recompile all the libraries and solvers. Similarly, many turbulence models, ranging from zero-, one- and two-equation eddy viscosity models to advanced Reynolds stress models are provided. Many of the models are available for both, high Reynolds number flows using wall functions, and for low Reynolds number flows with

wall-resolution.

OpenFOAM has a large user community, both in academia and industry. Being open-source, its use can result in significant financial savings as no license costs are associated. Although the work-flow is not as polished as with commercially available packages, it is fairly standardised and the textual input files are well suited for scripting and automation. The large user base, together with the backing of the OpenFOAM Foundation and OpenCFD Ltd., the continued development is ensured and commercial support, if required, is available.

All of the above listed features make OpenFOAM a very attractive development platform. Profiting from the very advanced finite volume and mesh handling capabilities, the effort of implementing a hybrid FV/JPDF scheme is very much reduced. Also, the basic particle tracking in the unstructured mesh is handled by OpenFOAM, allowing the implementer to focus on the specifics of the JPDF algorithm.

11.2 Implementation

The main goal of the implementation of the JPDF algorithm in OpenFOAM is to maximise flexibility and modularity. Researchers should be able to implement new models for the velocity, turbulence frequency, reaction chemistry and mixing with ease. The various models should be run-time selectable and configurable, so that the code does not need to be recompiled in order to select different models or change their parameters. Indeed, new models should be loadable from a *plug-in library* using the standard OpenFOAM mechanisms.

Further, the applicability of the algorithm should not be restricted by geometric constraints, allowing for non-orthogonal meshes and non-hexagonal cell shapes. However, this flexibility comes with a price: First, devising high-order, conservative interpolation schemes is difficult, if not impossible for general three-dimensional unstructured meshes. Second, the particle tracking algorithm is much more involved than for orthogonal meshes, incurring considerable computational cost. OpenFOAM offers a number of interpolation schemes, such as the conservative 0-order scheme, where the cell-centre value is assumed constant over the cell, a linearly-weighted scheme using cell values and one with a mixed linearly weighted cell-face interpolation formulation. The latter is the most accurate, but also most expensive scheme.

Luckily, most of the complications associated with tracking particles in an unstructured mesh are handled by OpenFOAM. The only geometric

issues that had to be dealt with, are related to the implementation of the boundary conditions, the treatment of quasi planar and quasi axisymmetric flows and the computation of the particle Courant numbers.

OpenFOAM requires the programmer of a particle code to implement general *serialisation* and *deserialisation* operations, i.e. writing the particle properties to and reading them from a data stream. It then uses these operations to automatically handle input, output and most importantly, parallelisation, relieving the programmer of the ordeals of handling the domain decomposition.

OpenFOAM provides two basic C++ classes associated with the particle tracking: `Particle` is the base class for all Lagrangian particles in OpenFOAM. The particles are managed by the `ParticleCloud` class. For variable density solvers, OpenFOAM uses a class derived from `basicThermo` to compute the thermodynamic state; its responsibility is to provide the density field to the RANS solver. Considering that in the algorithm outlined in the previous sections only the mean density field is passed to the RANS solver, the stochastic particle cloud is considered to be a *thermophysical* detail. Hence it is hidden away in the `mcThermo` class, which is derived from `basicThermo`. It is merely a façade for the `mcParticleCloud` class, derived from `Cloud`, which orchestrates the whole JPDF algorithm. By composition it manages the particles, the various models and the extracted statistical moments. It performs the second order spatial integration of the particle paths, evaluating the velocity, chemistry, turbulence frequency and mixing models at the midpoint and applies the appropriate boundary conditions as specified by the user. At the end of each time step, the statistical moments are estimated and time-averaged, before computing the mean fields. The class representing the individual notional particles is `mcParticle`. It derives from `Particle` and does not contain much functionality besides input/output. It is mainly a carrier for the particle properties.

For all the different kinds of models there is a common base class – `mcModel`. From it the following base classes for the different types of models are derived:

`mcVelocityModel` All velocity models should be derived from this class. In this work, only a SLM model for the full particle velocity has been implemented.

`mcReactionModel` The base class for all reaction chemistry classes. As of this writing, a class for inert gas flows, one using the Burke-Schumann assumption and one based on the steady flamelet concept with a single

mixture fraction are implemented.

`mcMixingModel` The parent class for all mixing models. The only mixing model implemented is the interaction by exchange with the mean model (IEM).

`mcOmegaModel` This is the class all models for the mean turbulence frequency should be derived from. The only currently implemented model uses the RANS model, either defining $\Omega(\boldsymbol{X}^*, t) = {}^{\varepsilon(\boldsymbol{X}^*,t)}/_{k(\boldsymbol{X}^*,t)}$ or, if the $k-\omega$ model is being used, $\Omega(\boldsymbol{X}^*, t) = \widetilde{\omega}(\boldsymbol{X}^*, t)$.

`mcPositionCorrection` This is the starting point for the density/position correction schemes. Both models as described in Section 10.5.1 are implemented.

`mcLocalTimeStepping` The base class from which the local time-stepping models should derive from. If disabled, the base class is used, assigning $\eta^* = 1$ to every particle. The model described in Section 10.6.3 is currently provided.

The parent class for all boundary conditions is `mcBoundary`. As of this writing boundary conditions for inflow, outflow, slip walls and symmetry planes and homogeneous directions for quasi planar and quasi axisymmetric flows are implemented.

An overview of the structure using the UML[4] notation is given in Figure 11.1.

11.3 Particle Properties

The `mcParticle` class defines a velocity, density, statistical mass and turbulence frequency property. Further, particles have the notion of a *correction velocity* (set by the density/position correction model) and a *tracking velocity* which is the effective velocity the particle tracking algorithm uses (i.e. the sum of the particle and correction velocity). For quasi planar cases, the out-of-plane velocity component of the tracking velocity will be null and for quasi axisymmetric flows this represents the velocity that transports the particle to the rotated destination point. Other properties are the local time-stepping parameter η^* and the particle Courant number

$$Co^* = \max_n \left(\frac{U^*_{\mathsf{track},i} \Delta x_i^{(n)}}{\Delta x_j^{(n)} \Delta x_j^{(n)}} \right) \Delta t \quad ,$$

[4] Refer to `http://www.omg.org/spec/UML/current` for the specifics of the notation

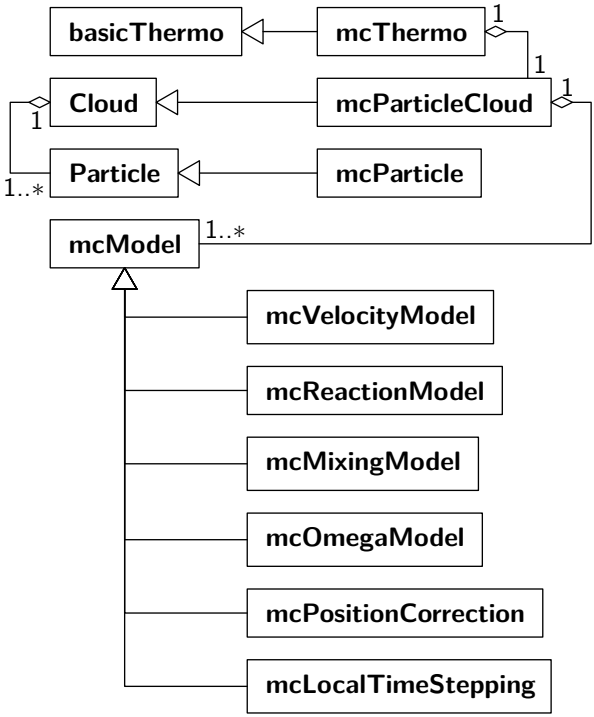

Figure 11.1 – Overview of the most important base classes and their relations.

where $\Delta \boldsymbol{x}^{(n)}$ is the distance vector from the centre of the cell in which the particle is located to the centre of the neighbouring cell n. The scalar properties, such as mixture fraction z^*, temperature T^* and scalar dissipation rate χ^* are stored in a vector that is configurable in the input data. In the same input configuration, the user is able to specify to which of the scalar properties to apply the mixing model and which of them are conserved. For the conserved properties, the algorithm computes and outputs the instantaneous, time-averaged (over 10^3 iterations) and cumulative flux errors.

11.4 Boundary Conditions

The implementation of the particle boundary conditions follows the description given in Section 10.7. The notable complication is the treatment of the outflow boundary, where the particle is not reflected at the moving wall, but rather at the physical wall. The particle velocity is then updated at the end of the iteration to recover the behaviour of the reflection at the moving wall, as is illustrated in Figure 10.3.

11.5 Particle Path Integration

This section does not describe the particle tracking algorithm implemented in OpenFOAM, as it is very involved and not subject of this work. The goal of this section is to outline the implementation of the second-order integration scheme described in Section 10.3.

The first half-step is implemented as described by (10.4). At the midpoint, all the models are evaluated. If the particle has been reflected at any boundary during the first half-step, the integration continues by switching to a first-order scheme. This is to overcome the complication of finding the reverse transformation of the newly obtained velocities at the midpoint. This may be improved in future developments of the algorithm. If, however, the particle has not been reflected during the first half-step, the particle is moved back to its starting position at $\boldsymbol{X}^{*(n)}$ and the new tracking velocity is then computed as given by (10.5).

Part III
Validation

12 Introduction

In this part of the work, four validation test cases are presented – in increasing complexity of the flow problem. First, a simple circular jet flow will be presented. The jet consists of propane, while the co-flow is plain air. This case is non-reactive and the density variations are very moderate. Its main purpose is to demonstrate internal consistency of the solver.

The second flow case is similar in geometry, but is reacting. The central jet consists of 25% methane and 75% air and it is surrounded by a premixed *pilot* flame where ethylene is used as the fuel. The pilot serves as the flame-holder; without it constantly igniting the fuel-air mixture, the flame would be blown out of the burner due to the high velocities. The jet and pilot are surrounded by a relatively slow co-flow of air. Technically, the flame is partially-premixed, but good results using models for non-premixed flames have been reported in the literature, e.g. Wang and Chen [82] and Nik et al. [55].

The next case is substantially more complex in its flow-pattern as it involves a recirculation zone. The central jet is surrounded by a circular bluff body, causing the recirculation zone. The device is again embedded in a co-flow of air. Here, the jet consists of air or ethylene, but no chemical reactions take place.

The third simulation case is that of the previously described bluff-body flow, including reactions. For this burner, the recirculation zone takes on the role of the flame-stabiliser: by feeding the hot products of the flame back towards the inlet, continuous ignition of the fresh gases is ensured. In this setting, the fuel is a 1:1 mixture (by volume) of methane and hydrogen.

Last, a auto-ignition stabilised flame in a complex three-dimensional geometry, similar to that of sequential burners, is simulated. Here, the goal is to demonstrate that the algorithm and the implementation are applicable to general geometries using an unstructured mesh.

13 Inert Propane Jet in Air

As briefly described in the introduction to this part, here the simulation results for a non-reactive propane (C_3H_8) jet in a slow co-flow of air are presented. The inner diameter of the fuel nozzle is 5.26 mm and its outer diameter is 9 mm. The bulk velocity of the propane jet is $53\,^{\mathrm{m}}/_{\mathrm{s}}$ and it exits into a square duct with an edge length of 200 mm and an axial length of 2 m. The co-flow of air inside the duct has a bulk velocity of $9.2\,^{\mathrm{m}}/_{\mathrm{s}}$. The full description of the experimental set up is given by Schefer et al. [73], Schefer and Dibble [71] and Schefer et al. [72]. The data base with experimental data, including documentation, can be obtained from the web-site of the TNF workshop [3].

Here, the density variations of the particles are computed using the ideal gas law,

$$\rho^* = \frac{p_a}{R^* T_0} \quad ,$$

where p_a =101325 Pa is the ambient pressure and T_0 =294 K the temperature of the inflow streams. The specific gas constant is computed by linear interpolation between the pure propane and air states using the mixture fraction z^*, i.e.

$$R^* = z^* R_{C_3H_8} + (1 - z^*) R_{\mathrm{air}} \quad .$$

The gas constants of propane and air are $188.55\,^{\mathrm{kg}}/_{\mathrm{mol}}$ and $287\,^{\mathrm{kg}}/_{\mathrm{mol}}$, respectively.

The data archive provides inflow profiles of the mean axial velocity $\widetilde{U}_1$ and the RMS of the axial fluctuating velocity, u', for the co-flow, but unfortunately not for the jet. Hence, the exit plane data measured by Schneider et al. [74] for the Sandia flame D, featuring a similar geometry, have been scaled for the correct bulk velocity. The TKE at the inflow is estimated from the reported RMS values for the fluctuations; in the jet, both the axial and cross-stream stresses are given by u' and v', and the TKE can be estimated as $k = {}^1/_2 \left(u'^2 + 2v'^2\right)$. In the co-flow isotropy is assumed, such

that $k = {}^3/_2 u'^2$. The inflow profile for the turbulence dissipation ε has been estimated by assuming turbulence in equilibrium for which the dissipation is equal to the production term in (6.20), i.e.

$$\varepsilon = \widetilde{u_i'' u_j''} \frac{\partial \widetilde{U}_i}{\partial x_i} \quad .$$

The Reynolds stresses in the above relation have been estimated using the eddy-viscosity assumption (6.17). At the nozzle lip and the duct wall, slip boundaries with no wall-modelling where used. The pressure at the outflow boundary was prescribed as 101325 Pa. The mixture fraction at the jet boundary was set to 1 and in the co-flow to 0.

For this quasi axisymmetric flow the domain size was chosen to be 300 mm by 150 mm and it has been discretised with 36×24 computational cells, where the regions close to the centre-line and the jet nozzle have been refined in axial and radial direction. On average, 40 particles were used and the time-averaging was performed over 10^3 time steps. For the RANS simulation, the $k - \varepsilon$ turbulence model was used with the standard parameters recommended by Launder and Sharma [39] (see Section 6.2.1), with the exception of $C_{\varepsilon 1}$ which was increased to 1.6 in order to capture the spreading rate of the jet. The model parameters are summarised in Table 13.1.

Convergence has been tracked by monitoring quantities at certain locations in the domain over time. These probe locations are listed in Table 13.2 and the histories of the mean mixture fraction, the RMS of the mixture fraction fluctuations and the mean density are displayed in Figure 13.1. For this relatively simple, non-reactive flow case with very moderate density variations, convergence has been reached after approximately 150×10^3 iterations.

The experimental data for the flow field has been measured using laser Doppler velocimetry (LDV) twice, once by seeding the jet and once by seeding the co-flow. In the graphs, these sets are marked using downwards pointing triangles and squares, respectively. The radial profiles of the mean axial and radial velocity at downstream positions $4D$, $15D$, $30D$ and $50D$ are displayed in Figure 13.2. The corresponding profiles for the RMS of the fluctuating axial and radial velocities at the same axial positions can be seen in Figure 13.3.

Figure 13.4 shows radial profiles of the turbulent shear stress and the TKE, also at downstream positions $4D$, $15D$, $30D$ and $50D$. In the experimental data, only the axial and radial normal stresses are reported, the transversal stress is unknown. For the purpose of the comparison with

Parameter	Value	Model
CFL	0.1	Time-step calculation
$C_{\varepsilon 1}$	1.6	$k-\varepsilon$
C_0	1.2	SLM
C_ϕ	2	IEM
N_{FV}	10	Loose coupling
N_{MC}	100	Loose coupling
C_{min}	0.8	Particle number control
C_{max}	1.2	Particle number control
C_{diff}	0.05	Particle distribution correction
C_{pos}	0.2	Position correction
κ	20	Local time-stepping
τ_U	10^{-5} s	Mean velocity correction
τ_k	10^{-5} s	TKE correction

Table 13.1 – Model parameters for the non-reacting propane jet simulation.

Probe number	Axial distance (x)	Radial distance (y)
1	$4D$	$1/2D$
2	$4D$	$3D$
3	$4D$	$7/2D$
4	$15D$	$1/2D$
6	$15D$	$3D$
5	$15D$	$7/2D$
7	$50D$	D
8	$50D$	$3D$
9	$50D$	$5D$

Table 13.2 – Locations of the probes used for the convergence monitoring of the propane jet simulation, where x and y denote the downstream and radial coordinates, respectively.

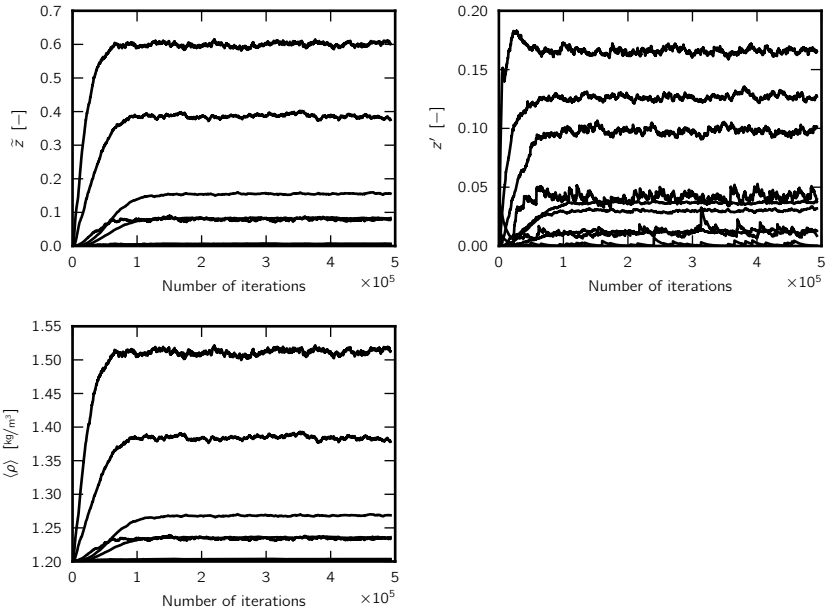

Figure 13.1 – Convergence histories for the mean mixture fraction, the RMS of the mixture fraction fluctuations and the mean density in the probe locations listed in Table 13.2.

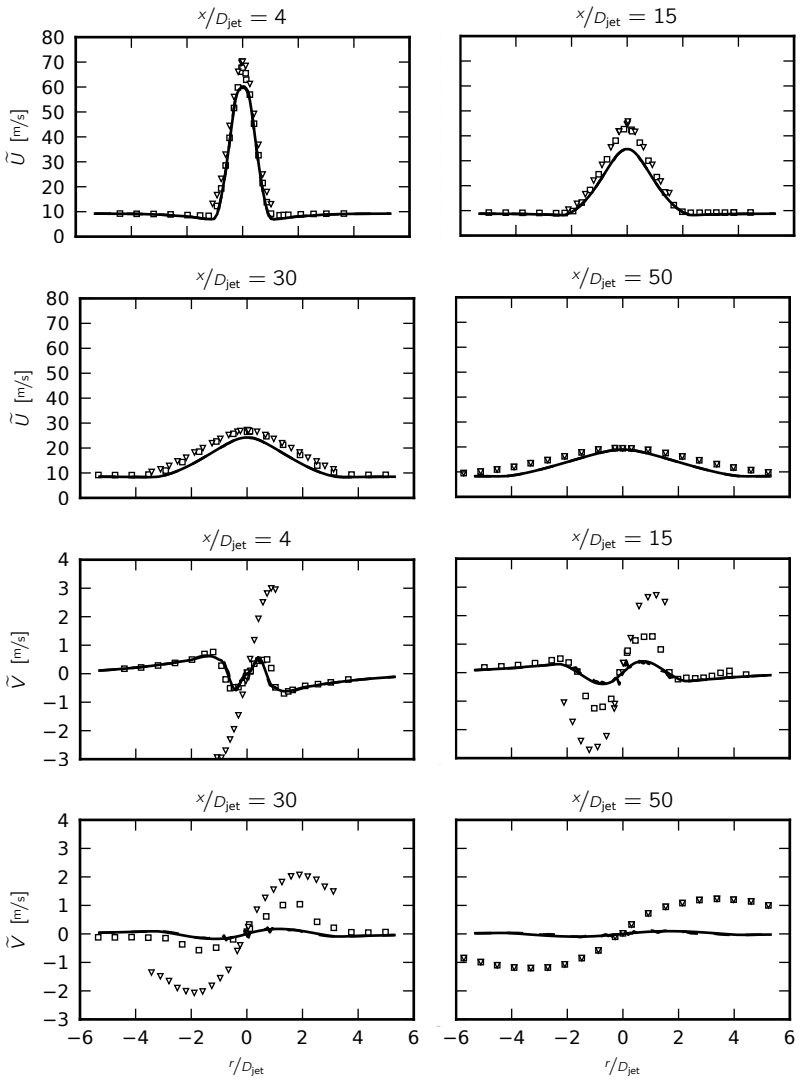

Figure 13.2 – Radial profiles of the mean axial (top two rows) and radial (bottom two rows) velocity for the propane jet at downstream positions $x/D = 4, 15, 30$ and 50. The solid lines represent the RANS simulation results, the dashed lines the JPDF results and the symbols the experimental data (triangles for the jet-seeded data, squares for the co-flow seeded data).

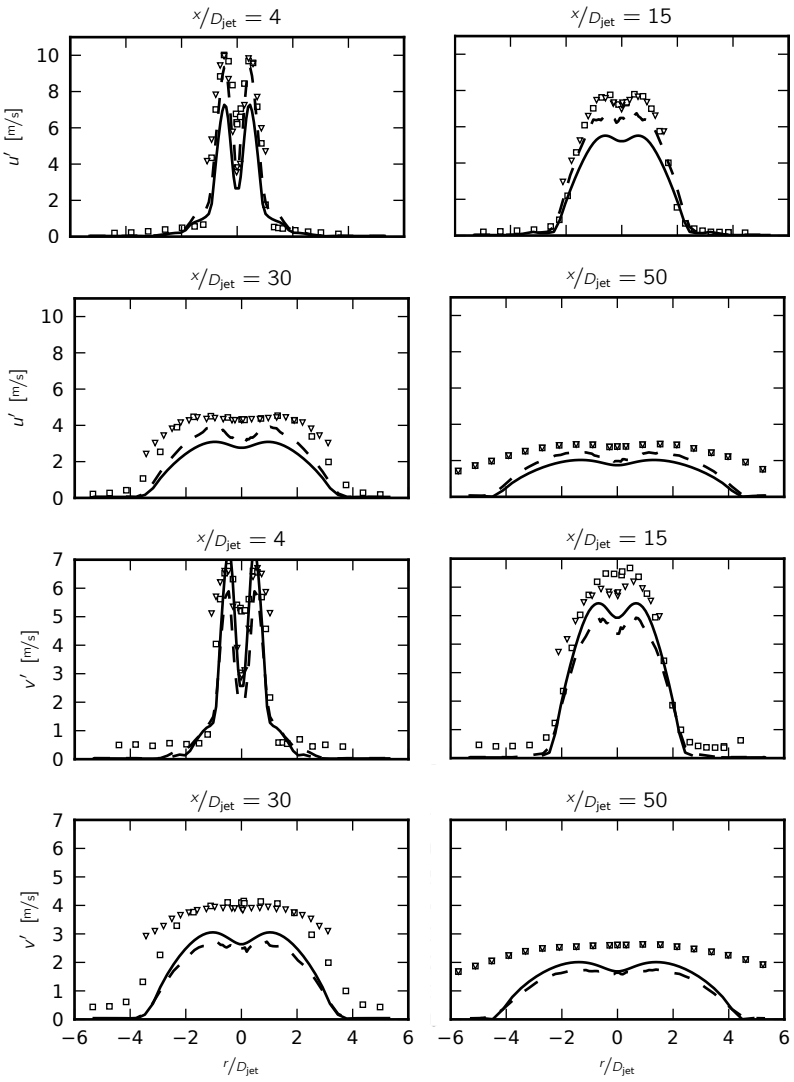

Figure 13.3 – Radial profiles of the axial (top two rows) and radial (bottom two rows) RMS velocity fluctuations for the propane jet at downstream positions $x/D = 4, 15, 30$ and 50. The solid lines represent the RANS simulation results, the dashed lines the JPDF results and the symbols the experimental data (triangles for the jet-seeded data, squares for the co-flow seeded data).

the simulation data, the TKE has been estimated by assuming that the radial normal stress v' is equal to the transversal stress w', resulting in $k = 1/2\left(u'^2 + 2v'^2\right)$. At the same downstream positions, the mean mixture fraction and the RMS of its fluctuations are presented in Figure 13.5. Last, the mean density and particle mass density is compared to the experimental data in Figure 13.6.

As can be seen in Figures 13.2, 13.4 and 13.6, internal consistency is achieved. The profiles of the RANS and JPDF mean velocities and TKE are virtually identical. The maximum absolute relative error between the mean and particle densities is 0.11. The mean axial velocity matches the experimental data closely, except for the centre-line peak that is underpredicted substantially at positions $4D$ and $15D$. The first profile of the radial velocity matches the co-flow seeded experimental data very well. Further downstream it is generally underpredicted. However, there is considerable uncertainty in the experimental data, which can be seen by the large discrepancies between the jet and co-flow seeded data at the first three positions.

The profiles of u' and v' in Figure 13.3, and here to a lesser extent that of $\widetilde{u'v'}$ in Figure 13.2, demonstrate that the algorithm does not enforce consistency of the individual Reynolds stress components between the RANS and JPDF simulations, but rather only of its trace, as can be seen in the profile of k in Figure 13.4.

Figure 13.5 shows that excellent agreement between experimental data and the mean mixture fraction has been achieved. The first two profiles of the RMS of the mixture fraction fluctuations significantly deviate from the experimental data, but match it closely again further downstream. Linearly related to the mean mixture fraction, the mean density profiles in Figure 13.6 also reproduce the experimental data very well.

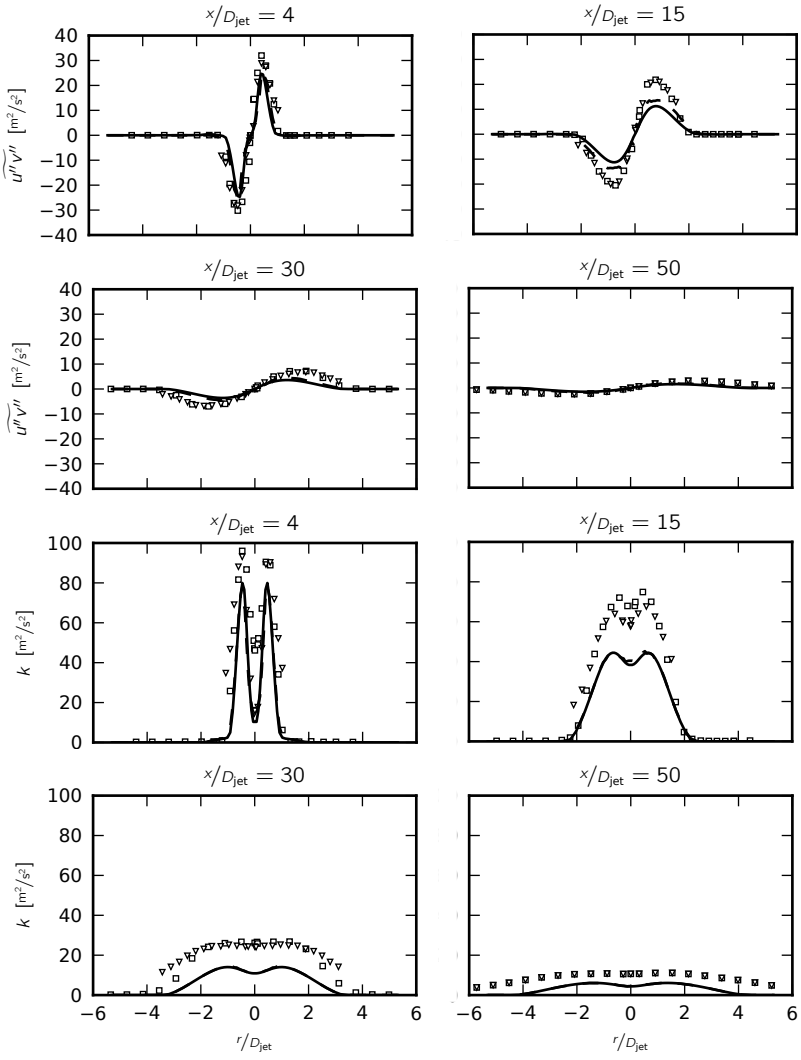

Figure 13.4 – Radial profiles of the shear stress (top two rows) and TKE (bottom two rows) for the propane jet at downstream positions $x/D = 4, 15, 30$ and 50. The solid lines represent the RANS simulation results, the dashed lines the JPDF results and the symbols the experimental data estimated as $k = 1/2\left(u'^2 + 2v'^2\right)$ (triangles for the jet-seeded data, squares for the co-flow seeded data).

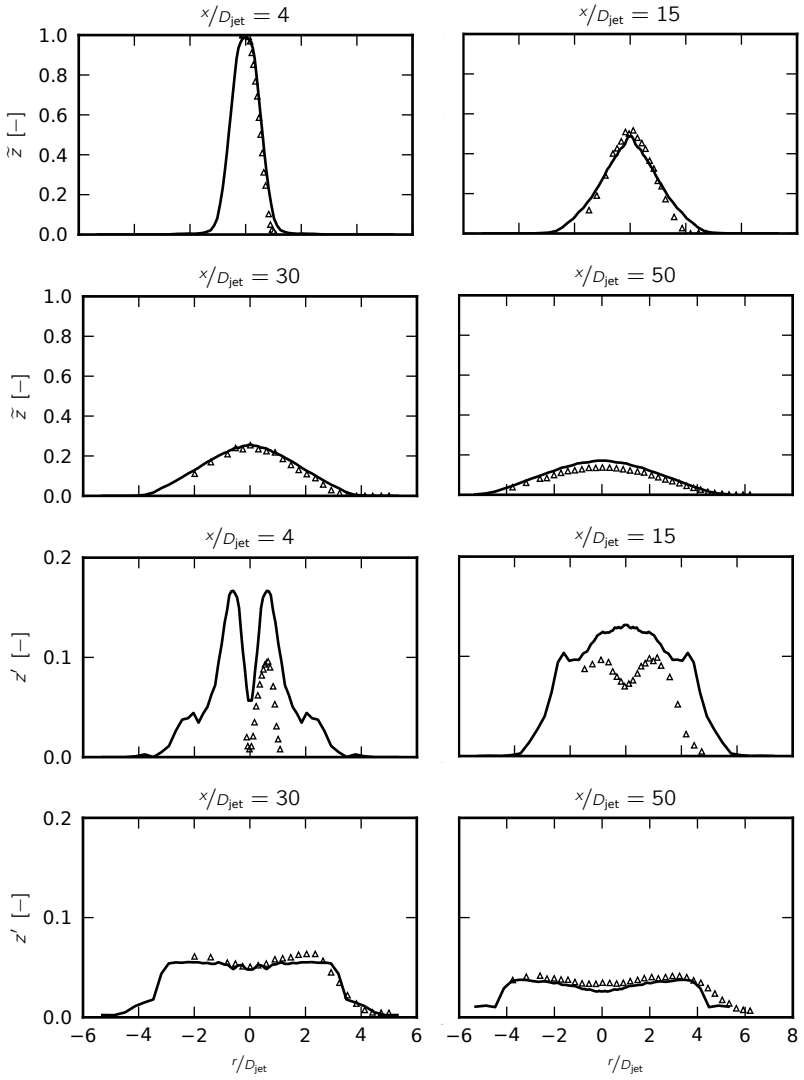

Figure 13.5 – Radial profiles of the mean mixture fraction (top two rows) and RMS of the fluctuating mixture fraction (bottom two rows) for the propane jet at downstream positions $x/D = 4, 15, 30$ and 50. The solid lines represent the simulation results and the symbols the experimental data.

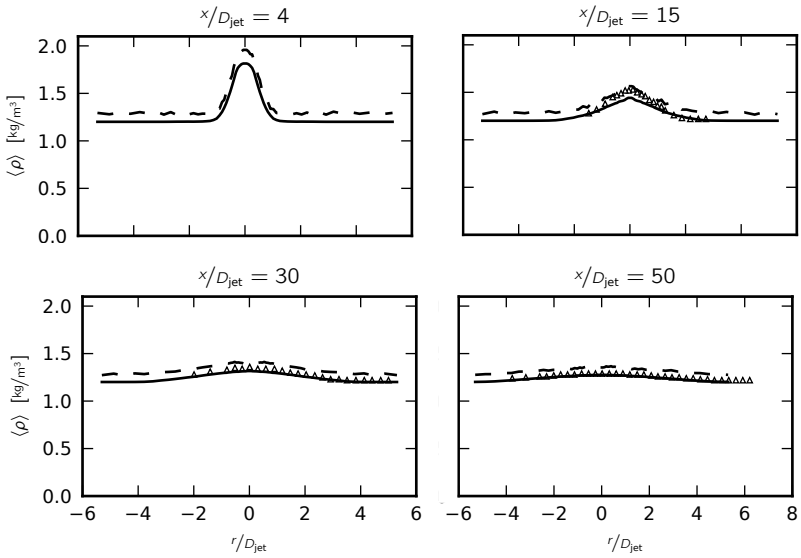

Figure 13.6 – Radial profiles of the mean density (solid line) and the particle mass density (dashed line) for the propane jet at downstream positions $x/D = 4, 15, 30$ and 50. The symbols represent the experimental data (triangles for the jet-seeded data, squares for the co-flow seeded data).

14 Partially Premixed Jet Flame

In this section, simulation results for the *Sandia flame D* will be shown. It is a piloted jet flame, where the fuel is a mixture of 25% methane (CH_4) and 75% dry air, by volume. The jet bulk velocity is 49.7 m/s, its temperature 294 K and the pressure is atmospheric. The pilot is a mixture of ethylene (C_2H_4), hydrogen (H_2), air, CO_2 and nitrogen (N_2) with an equivalence ratio of $\phi = 0.77$. It has been chosen such that the nominal enthalpy and equilibrium composition are the same as for the methane-air mixture at the same equivalence ratio in order to simplify modelling. The surrounding co-flow has a velocity of 0.9 m/s, a temperature of 291 K and it is atmospheric as well.

The geometric dimensions of the burner are given by the fuel jet diameter, $2R_{\text{jet}}$ =7.2 mm, the inner and outer diameters of the pilot which are 7.7 mm and $2R_{\text{pilot}}$ =18.2 mm, respectively, and the outer diameter of the pilot wall, 18.9 mm. The burner is placed in a square, vertical duct with an edge length of 300 mm. The experimental set up and data acquisition methods for the scalar fields are described in detail by Barlow and Frank [5], Barlow et al. [4] and the data archives along with their documentation is available from the TNF workshop website [3]. The velocity field has been experimentally investigated by Schneider et al. [74]. A sketch of the burner is given in Figure 14.1.

Similar to the propane jet presented in the previous section, slip wall boundary conditions where applied to the fuel and pilot rims as well as the outer wall. At the inflow boundaries, profiles for the axial and radial mean velocities, the normal axial and radial turbulent stresses, as well as the turbulent shear stress are provided by the experimental data set by Schneider et al. [74]. As for the propane jet, the TKE at the inflow boundaries was estimated as $k = 1/2(u'^2 + 2v'^2)$. For the turbulence dissipation, a turbulence in equilibrium assumption as described in Section 13 was employed to determine the inflow profile. The mixture fraction in the jet was set to

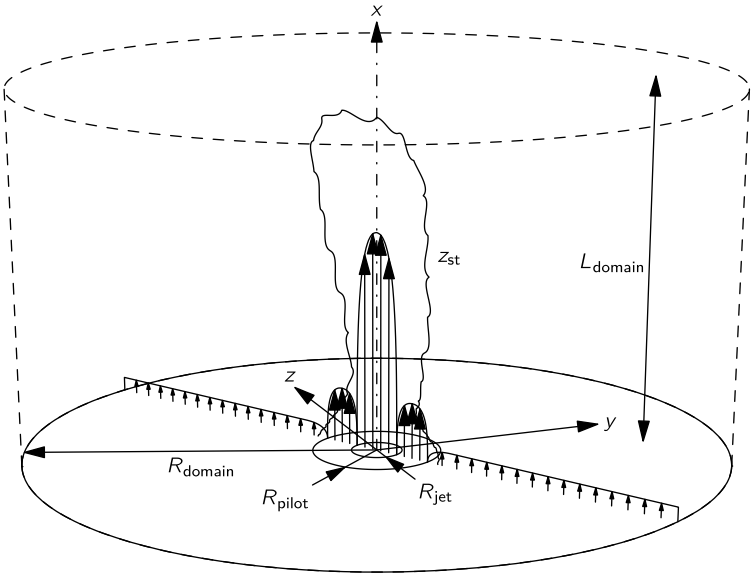

Figure 14.1 – Sketch of the Sandia flame D burner (not to scale).

1, in the co-flow to 0 and the pilot was set to 0.27, as suggested by the documentation of the experimental data. The mean density at the inflow boundaries was computed consistently with the mixture fraction as 1.08, 0.18 and 1.22 in the jet, pilot and co-flow, respectively. The pressure at the outflow boundary was prescribed as 101325 Pa.

Again, the flow is assumed to be quasi axisymmetric. The length and diameter of the domain are L_{domain} =800 mm and $2R_{\text{domain}}$ =300 mm, respectively, and it has been discretised with 54×54 computational cells. Mesh refinement in axial and radial direction has been employed near the nozzle exit. 40 particles per cell and a time-averaging constant of 20×10^3 time steps were used.

The turbulent combustion was modelled with the steady flamelet model. Flamelet tables for the scalar dissipation rates $\chi = 1$, 1.375, 2.5, 3.125, 5, 10, 15, 20, $30^1/_s$ were obtained with the software FlameMaster by Pitsch [60]. An exemplary profile is displayed in Figure 8.5. The remaining model constants are listed in Table 14.1.

Radial profiles of the mean axial and radial velocities at downstream positions $3D$, $7.5D$, $15D$, $30D$, $45D$ and $60D$ are displayed in Figure 14.2.

Parameter	Value	Model
CFL	0.1	Time-step calculation
$C_{\varepsilon 1}$	1.6	$k-\varepsilon$
C_0	1.2	SLM
C_ϕ	2	IEM
C_χ	6	Steady flamelet
N_{FV}	10	Loose coupling
N_{MC}	200	Loose coupling
C_{min}	0.8	Particle number control
C_{max}	1.2	Particle number control
C_{diff}	0.05	Particle distribution correction
C_{pos}	0.25	Position correction
κ	20	Local time-stepping
τ_U	10^{-5} s	Mean velocity correction
τ_k	10^{-5} s	TKE correction

Table 14.1 – Model parameters for the Sandia flame D simulation.

As can be seen, the simulation results match the experimental data quite well, and the consistency between the RANS and JPDF mean velocities is given. The radial velocity component, however, shows significant deviations from the experimental data. It has to be taken into consideration, that the magnitude of the radial component is much smaller than that of the axial one. Hence, small relative errors in the axial component, lead to large relative errors in the radial component due to the continuity equation. Also, near the centre line, the radial velocity component of the JPDF simulation exhibits a strong peak at downstream position $15D$, the reason for which is as of yet unclear.

Figure 14.3 presents the RMS values of the fluctuating axial and radial velocities. Here, the results are not as convincing; the deviations from the experimental data are quite large, and the spike near the centre line at position $15D$ shows in both components. The turbulent shear stress, as displayed in Figure 14.4, matches the experimental data well, apart from the spike at $15D$ near the centre line and a underprediction at $45D$. Interestingly, the RANS and JPDF values are virtually identical (again, exempting the spike at $15D$), despite consistency not being enforced.

The mean mixture fraction profiles, displayed in Figure 14.5, match the

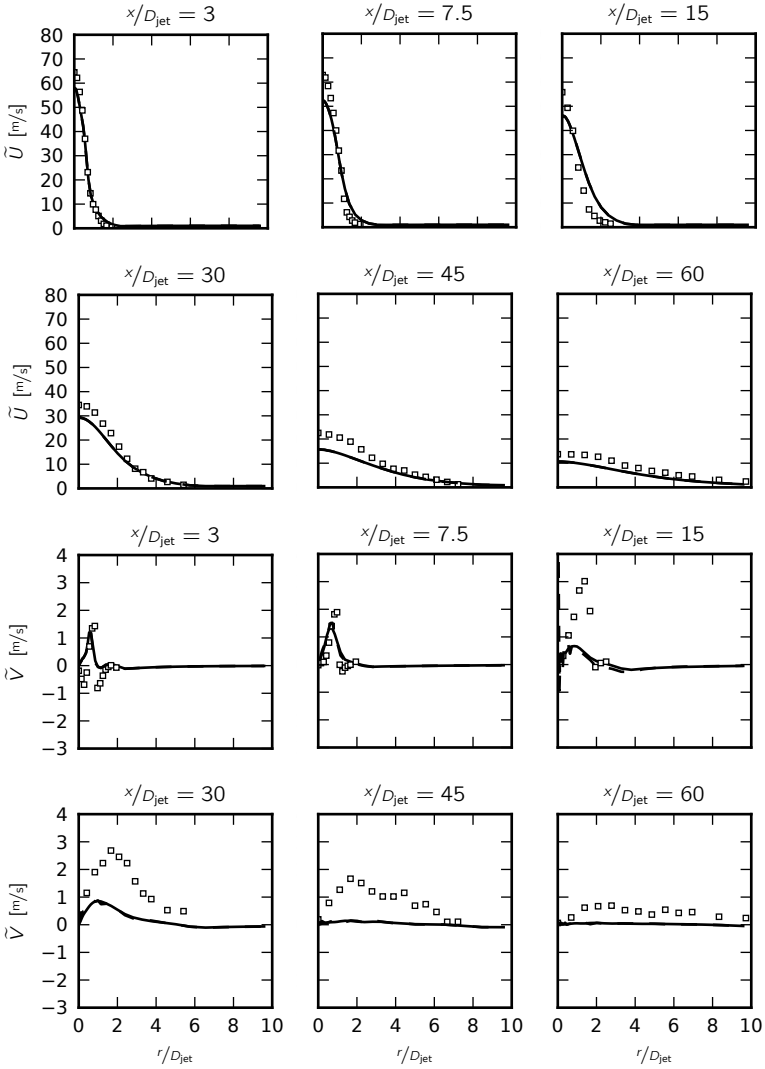

Figure 14.2 – Radial profiles of the mean axial (top two rows) and radial (bottom two rows) velocity for the Sandia flame D at various downstream positions. The solid lines represent the RANS simulation results, the dashed lines the JPDF results and the symbols the experimental data.

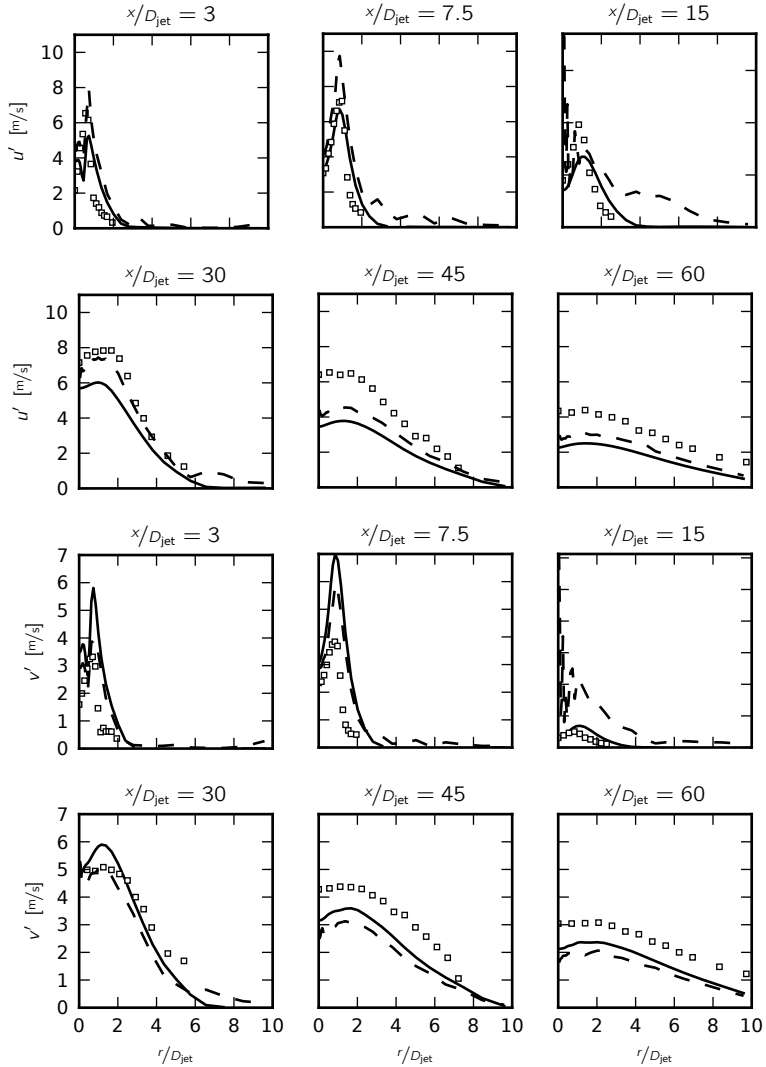

Figure 14.3 – Radial profiles of the axial (top two rows) and radial (bottom two rows) RMS velocity fluctuations for the Sandia flame D at various downstream positions. The solid lines represent the RANS simulation results, the dashed lines the JPDF results and the symbols the experimental data.

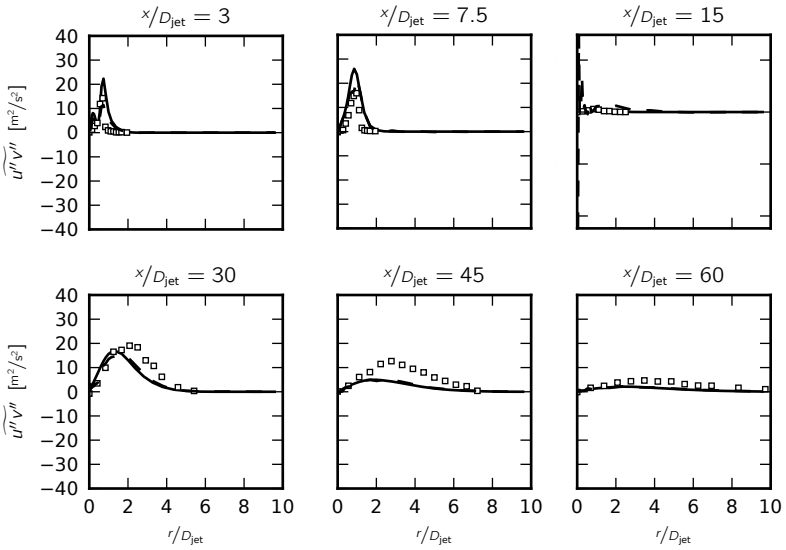

Figure 14.4 – Radial profiles of the turbulent shear stress for the Sandia flame D at various downstream positions. The solid lines represent the RANS simulation results, the dashed lines the JPDF results and the symbols the experimental data.

experimental data quite satisfactorily. The profiles of the RMS values of the fluctuating mixture fraction, shown in the same figure, initially overpredict the peak value in the first two cross-sections, and the first one does not fully capture the shape which might be due to an underresolved mesh. The rise near the centre line is predicted too early, as can be seen in the graph for downstream position $30D$.

The radial profiles of the mean temperature in Figure 14.6 are in good agreement with the experimental data, except at downstream position $60D$, where the underprediction is quite significant. The RMS profiles of the fluctuating temperature match the shape of the experimental data well. However, the peaks are either under- or overpredicted.

The radial profiles of the mean and particle mass densities in Figure 14.7 show good internal consistency. No experimental data is available for quantitative comparison, however.

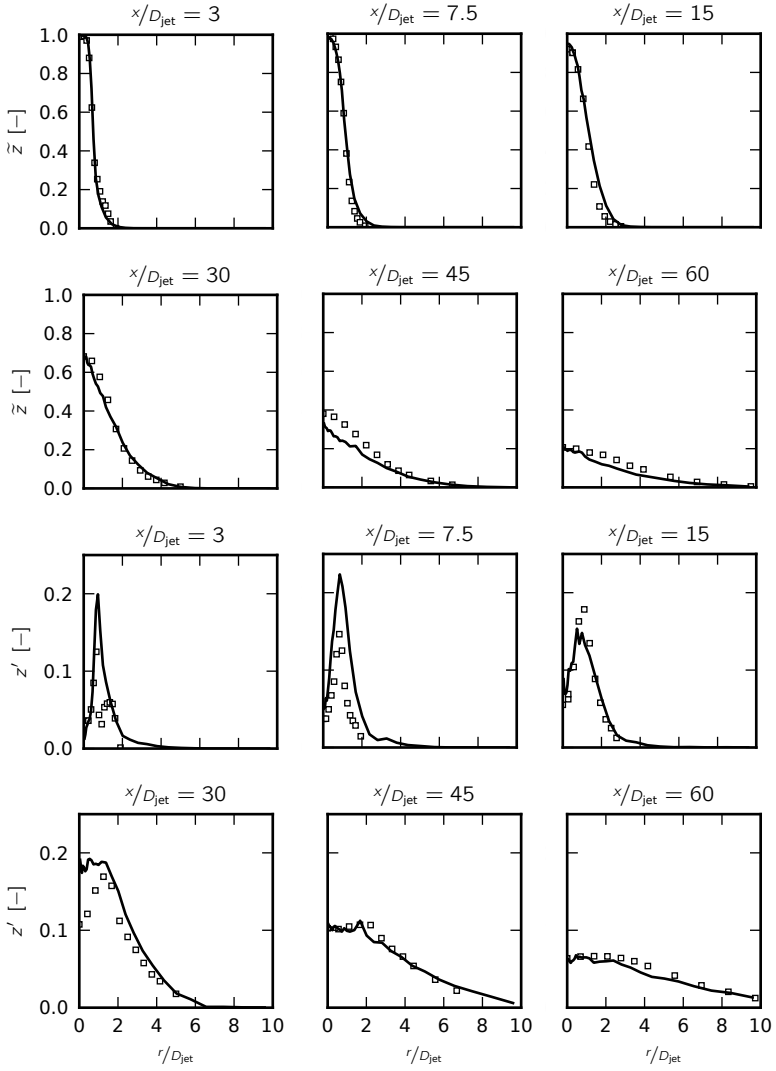

Figure 14.5 – Radial profiles of the mean mixture fraction (top two rows) and RMS of the fluctuating mixture fraction (bottom two rows) for the Sandia flame D at various downstream positions. The solid lines represent the simulation results and the symbols the experimental data.

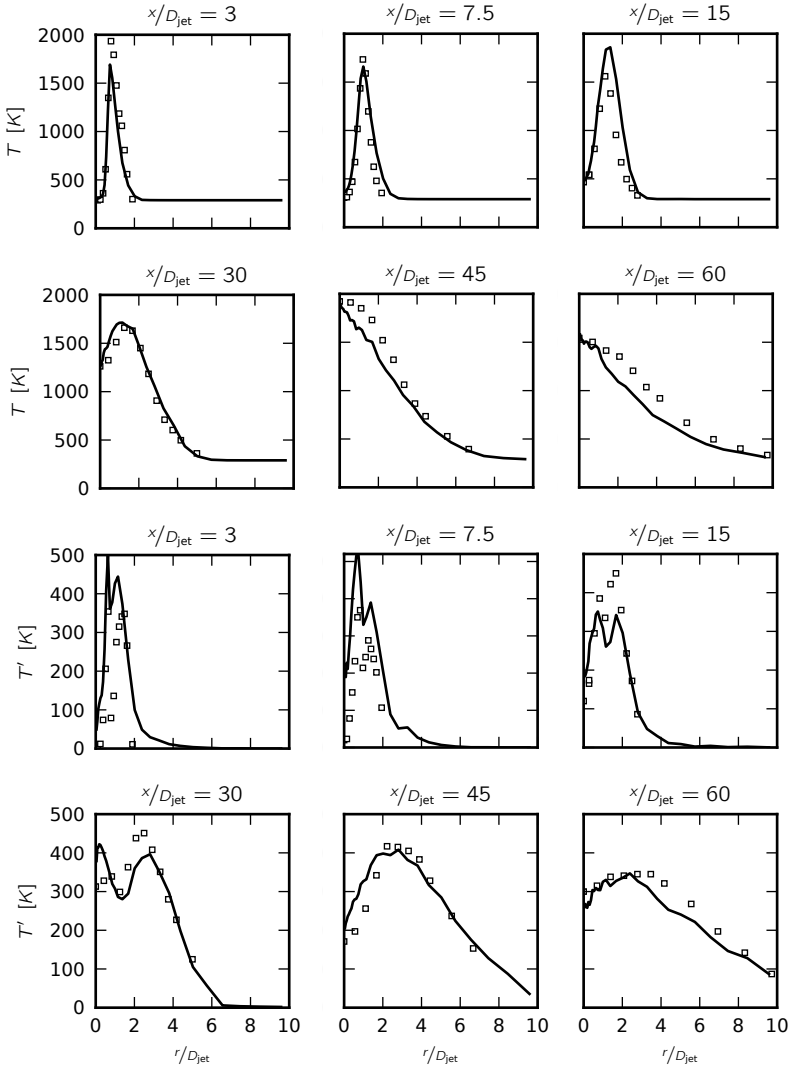

Figure 14.6 – Radial profiles of the mean temperature (top two rows) and RMS of the fluctuating temperature (bottom two rows) for the Sandia flame D at various downstream positions. The solid lines represent the simulation results and the symbols the experimental data.

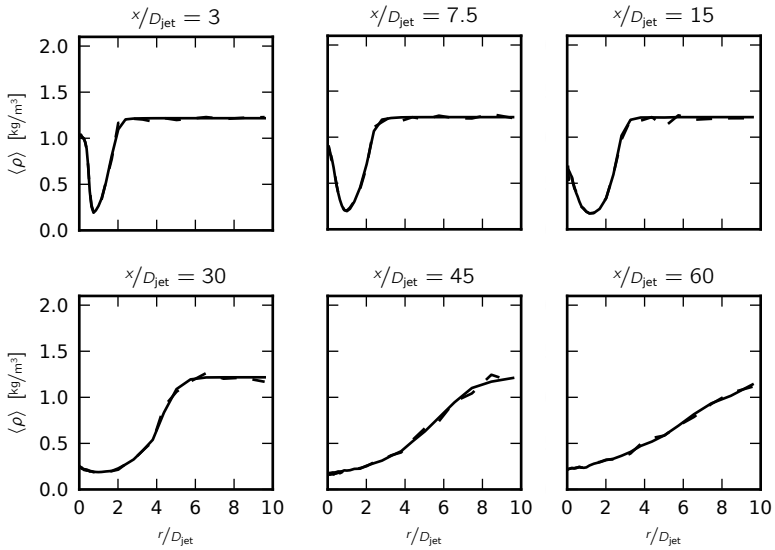

Figure 14.7 – Radial profiles of the mean density (solid line) and the particle mass density (dashed line) at various downstream positions for the Sandia flame D.

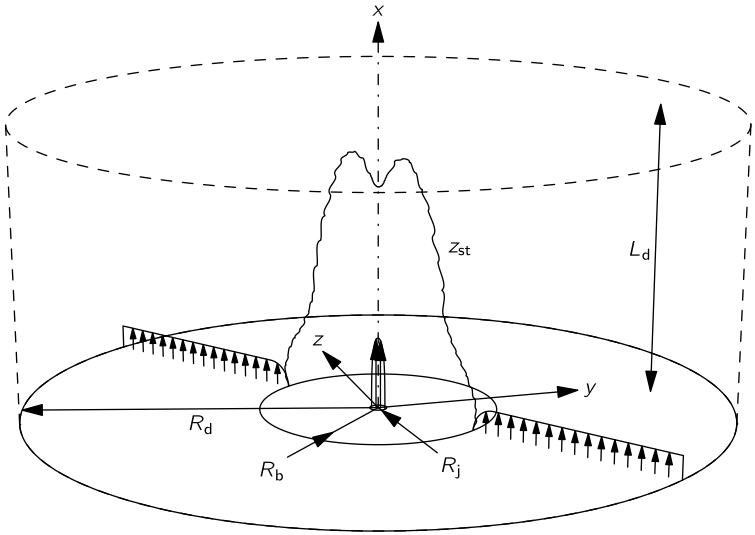

Figure 15.1 – Sketch bluff body flow configuration (not to scale).

15 Bluff-Body Flow

The non-reactive flow case presented in this section is much more challenging than the previous two. A ceramic, cylindrical bluff body contains a circular orifice at its centre through which a jet enters the flow domain. The device is surrounded by a co-flow of air with a velocity reported as $20^{m}/_{s}$. The diameter of the central jet is $2R_j$ =3.6 mm and that of the bluff body is $D_b = 2R_b$ =50 mm. The wind tunnel has a square cross-section of 305 mm×305 mm. A schematic of the device is depicted in Figure 15.1

The flow field has been measured by Dally et al. [14] with a jet consisting of air only, at a bulk velocity of $61^{m}/_{s}$. Three different measurement sets are

made available by the university of Sydney [44]. In the graphs of the flow field data, set 1 (dated from 1995) is represented by squares, set 2 (dated 1. December 1999) by downwards pointing triangles and set 3 (dated 15. December 1999) by upwards pointing triangles. The mixing field data has also been investigated by Dally et al. [14], however, here the reported jet velocity is $50^{\mathrm{m}/\mathrm{s}}$ and it consists of ethylene (C_2H_4). This medium has been selected because it has a similar molecular weight as air ($0.028^{\mathrm{kg}/\mathrm{mol}}$ compared to $0.029^{\mathrm{kg}/\mathrm{mol}}$) and gives a strong signal in the Raman scattering measurements.

Because the variations in density are approximately 3%, it can be assumed to be constant. Consequently, the JPDF part of the hybrid algorithm has no influence on the RANS simulation, and one-way-coupling can be used. Here, the RANS simulation is run as a preprocessing step and then frozen for the duration of the JPDF simulation.

As in the previous cases, the flow is assumed to be quasi axisymmetric. The simulation domain of size R_d =150 mm by L_d =300 mm has been discretised with 64×64 cells, where refinement near the centre-line and the inflow plane was used. Both, global and local time-stepping – with a maximum local time-stepping parameter of $\kappa = 20$ – was employed. In average 40 particles per cell have been used and the time-averaging coefficient has been set to 10^3 iterations in the case of local time-stepping and 50×10^3 for the global time-stepping case. Table 15.1 lists the model parameters. The simulation was performed in parallel, using four processors.

Radial profiles of the mean axial and radial velocity obtained from the RANS simulation with a jet bulk velocity of $61^{\mathrm{m}/\mathrm{s}}$ at downstream positions $0.2D_b$, $0.4D_b$, $0.8D_b$, $1.2D_b$, $1.8D_b$ and $3.4D_b$ are shown in Figure 15.2. The simulation results align very well with the simulation results, except at position $3.4D_b$ where the axial centre-line velocity is underpredicted, and as a consequence, the radial velocity is overpredicted. The scatter in the experimental data for the radial velocity component is considerable, and again, small errors in the axial velocity lead to large errors in the radial velocity. In general, the shape of the radial velocity component, however, is captured well. At the same downstream positions, the radial profiles for the RMS of the fluctuating radial and axial velocities are presented in Figure 15.3. Profiles of the turbulent shear stress $\langle u'v' \rangle$ are displayed in Figure 15.4. Considering that only the relatively simplistic $k - \varepsilon$ eddy-viscosity model has been used which is considered ill suited for flows with strong streamline curvature, the results are in surprisingly good agreement with the experimental data. The data in turn shows a large scatter across

Parameter	Value	Model
CFL	0.1	Time-step calculation
$C_{\varepsilon 1}$	1.6	$k-\varepsilon$
C_0	1.2	SLM
C_ϕ	2	IEM
N_{FV}	0	Loose coupling
N_{MC}	1	Loose coupling
C_{min}	0.8	Particle number control
C_{max}	1.2	Particle number control
C_{diff}	0.05	Particle distribution correction
C_{pos}	0.2	Position correction
τ_U	10^{-5} s	Mean velocity correction
τ_k	10^{-5} s	TKE correction

Table 15.1 – Model parameters for the non-reacting bluff body flow simulation.

the various data sets.

Figure 15.5 shows radial profiles of the mean mixture fraction $\langle z \rangle$ and Figure 15.6 of the RMS of the fluctuating mixture fraction, z' at downstream positions $0.4D_b$, $0.61D_b$, $0.8D_b$, $1.01D_b$, $1.206D_b$ and $1.356D_b$ for simulations with local time-stepping (limiter $\kappa = 20$) and without local time-stepping compared to the experimental data. As can be seen, agreement with the experimental data is quite good, although there is a slight tendency of the mean mixture fraction to be underpredicted in the first three sections, and stronger so in the fourth and fifth sections. The fluctuations are predicted quite satisfactorily, except for the fourth and fifth section.

Radial profiles for the relative error of the particle mass density q with respect to the flow density $\rho = 1.2 \mathrm{kg/m^3}$ are depicted in Figure 15.7, comparing the results of the simulations with and without local time-stepping.

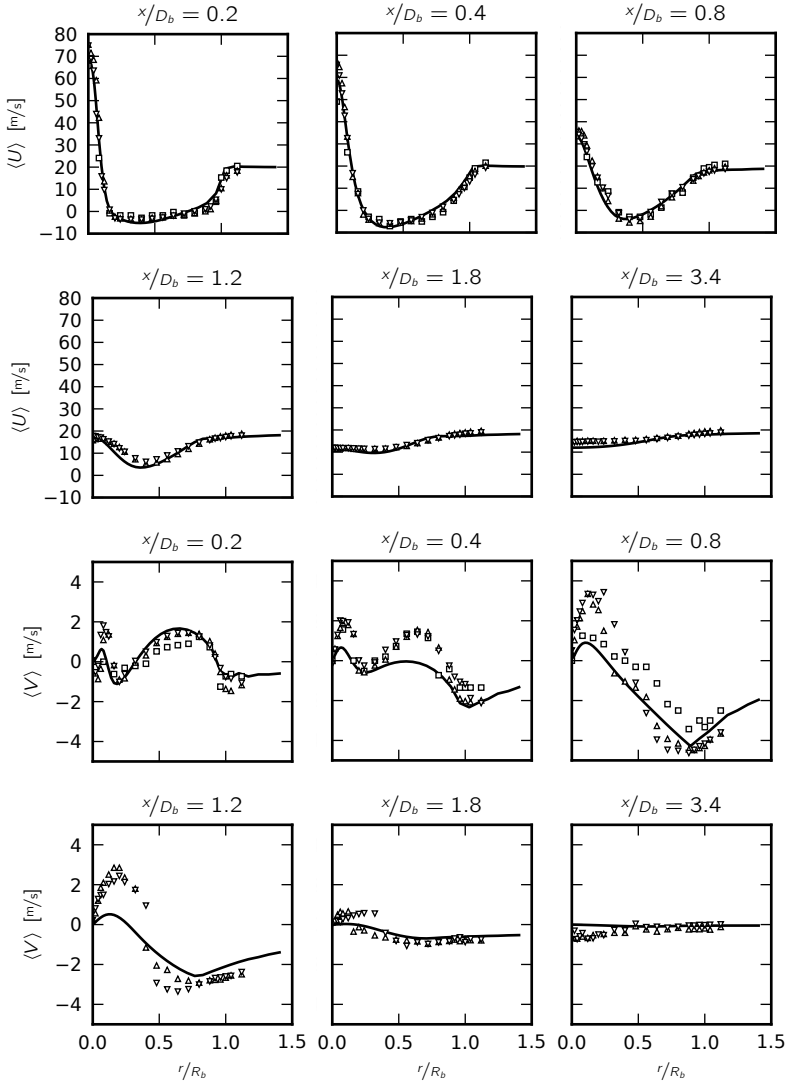

Figure 15.2 – Radial profiles of the mean axial (top two rows) and radial (bottom two rows) velocity for the bluff body flow with 61 m/s jet bulk velocity at various downstream positions. The solid lines represent the simulation results, the symbols the experimental data.

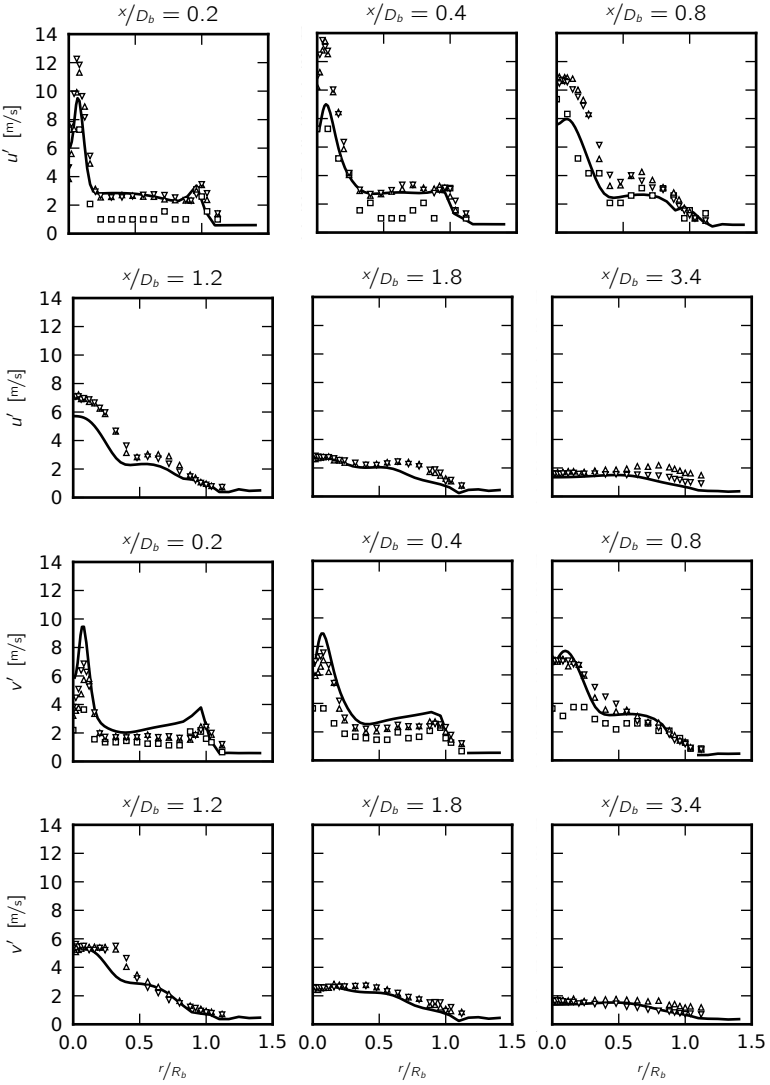

Figure 15.3 – Radial profiles of the axial (top two rows) and radial (bottom two rows) RMS velocity fluctuations for the bluff body flow with 61 m/s jet bulk velocity at various downstream positions. The solid lines represent the simulation results, the symbols the experimental data.

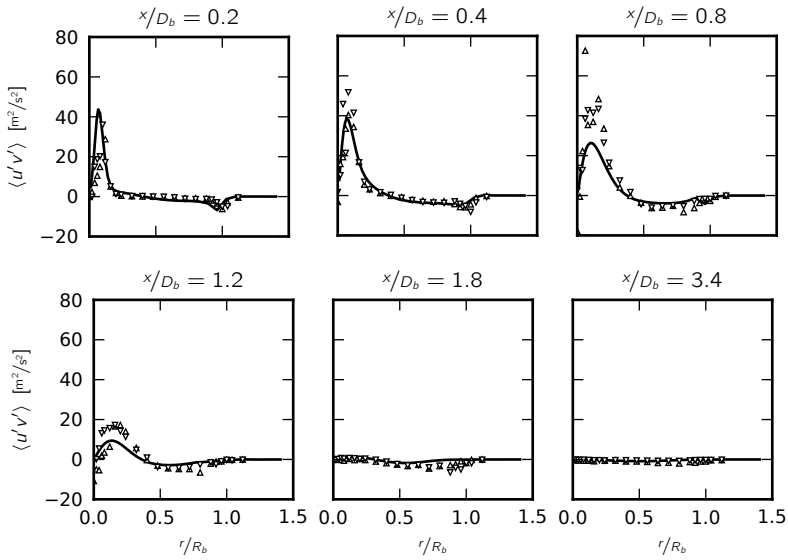

Figure 15.4 – Radial profiles of the turbulent shear stress for the bluff body flow with $61^{m}/_{s}$ jet bulk velocity at various downstream positions. The solid lines represent the simulation results, the symbols the experimental data.

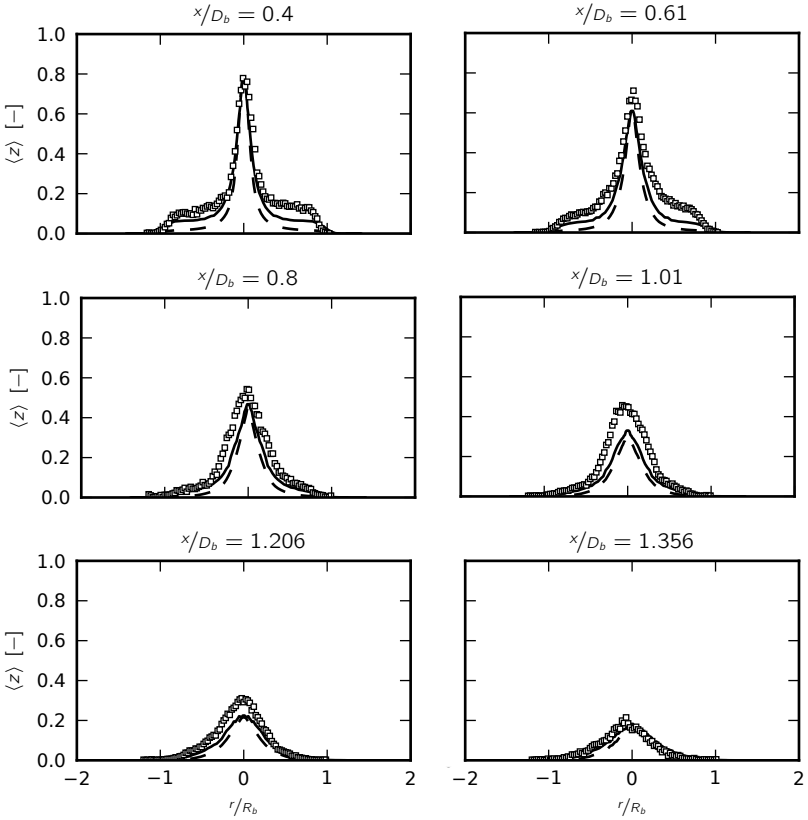

Figure 15.5 – Radial profiles of the mean mixture fraction for the bluff body flow with $50^{m}/_{s}$ jet bulk velocity at various downstream positions. The solid and dashed lines represent the simulation results with local time stepping and without, respectively. The symbols mark the experimental data.

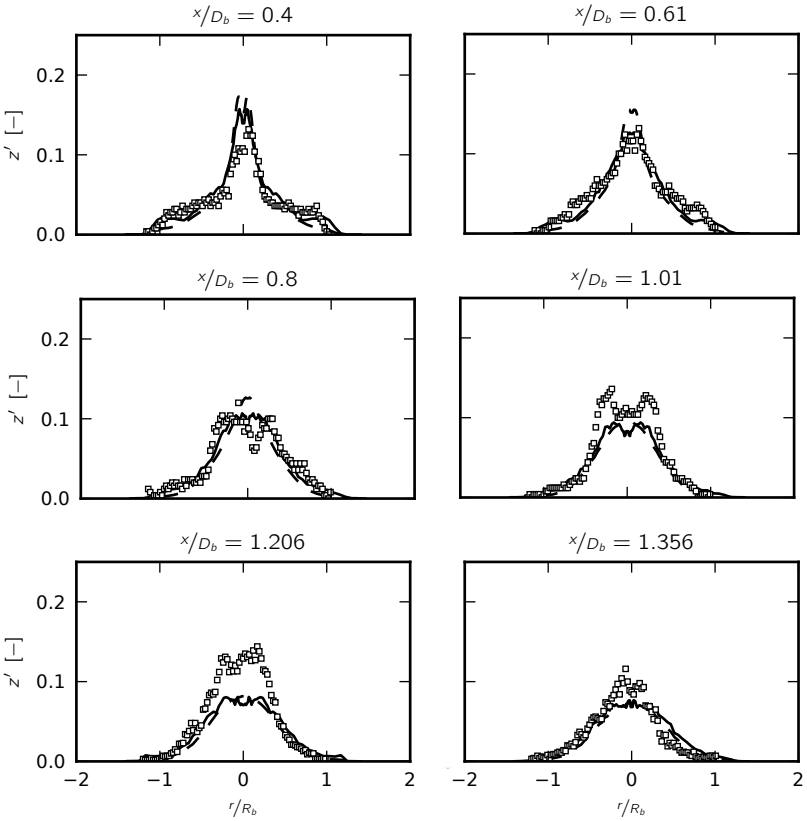

Figure 15.6 – Radial profiles of the RMS of the fluctuating mixture fraction for the bluff body flow with $50^{m}/_{s}$ jet bulk velocity at various downstream positions. The solid and dashed lines represent the simulation results with local time stepping and without, respectively. The symbols mark the experimental data.

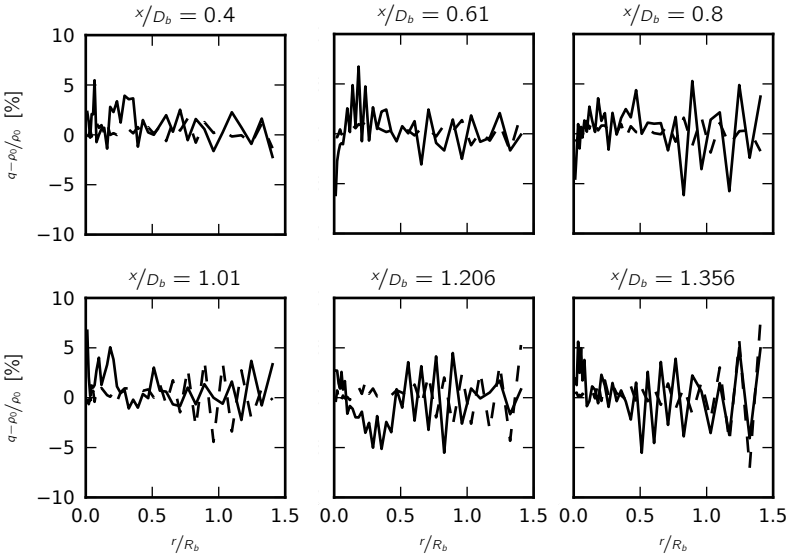

Figure 15.7 – Radial profiles of the relative error of the particle mass density q with respect to the flow density $\rho = 1.2 \mathrm{kg}/\mathrm{m}^3$ for the bluff body flow with $50 \mathrm{m}/\mathrm{s}$ jet bulk velocity at various downstream positions. The solid and dashed lines represent the simulation results with local time stepping and without, respectively.

16 Reactive Bluff-Body Flow

Here, the simulation results for a bluff body stabilised flame are presented. The geometrical configuration is identical to that described for the bluff body flow in Section 15. The fuel jet consists of a 1:1 mixture (by volume) of methane (CH_4) and hydrogen (H_2) and it has a bulk velocity of $108^{m}/_{s}$. For the co-flow of air the bulk velocity is reported as $35^{m}/_{s}$. The flame has been investigated experimentally by Masri et al. [43] and data archives are available from the University of Sydney [44]. Here, the flame labelled *HM1E* has been simulated. For the flow field, two data sets are available; set 1 (dated from 21. January 2000) is represented by downwards pointing triangles, set 2 (dated from 11. February 2000) by upwards pointing triangles.

80×80 computational cells have been used to discretise the quasi axisymmetric R_d =150 mm by L_d =300 mm simulation domain. Refinement was applied in radial and axial direction to better resolve the gradients near the jet and the exit plane. The average number of particles was set to 40 and the time-averaging parameter was chosen as 5×10^3. Local time-stepping with a upper bound of $\kappa = 20$ was enabled. The steady flamelet model was used for the reaction chemistry. The flamelets where tabulated using FlameMaster [60] at scalar dissipation rates $\chi = 1$, 2, 5, 10, 15, 20, $30^{1}/_{s}$. Six processors were used for this simulation.

Convergence has been monitored as described in section 13, where the probe locations are listed in Table 16.2. Histories of the mean axial and radial velocities, the mean mixture fraction, the RMS of its fluctuations the mean temperature and mean density are shown in Figure 16.1. A comparison of the convergence histories, comparing simulations with time-averaging factors of 5×10^3 and 80×10^3, respectively, is shown in Figure 16.2. Both used only 20 particles per cell. As can be clearly seen simulation using a large time-averaging factor converges considerably slower, but it also shows much less noise.

Parameter	Value	Model
CFL	0.1	Time-step calculation
$C_{\varepsilon 1}$	1.6	$k-\varepsilon$
C_0	1.2	SLM
C_ϕ	2	IEM
C_χ	6	Steady flamelet
N_{FV}	10	Loose coupling
N_{MC}	100	Loose coupling
C_{min}	0.8	Particle number control
C_{max}	1.2	Particle number control
C_{diff}	0.05	Particle distribution correction
C_{pos}	0.2	Position correction
τ_U	10^{-5} s	Mean velocity correction
τ_k	10^{-5} s	TKE correction

Table 16.1 – Model parameters for the bluff body flame simulation.

Probe number	Axial distance (x)	Radial distance (y)
1	$1/2 D_b$	0
2	D_b	0
3	$2D_b$	0
4	$5D_b$	0
5	$1/2 Db$	mid bluff-body = 13.4 mm
7	D_b	mid bluff-body = 13.4 mm
6	$2D_b$	mid bluff-body = 13.4 mm
8	$5D_b$	mid bluff-body = 13.4 mm
9	$1/2 D_b$	$1/2 D_b$
10	D_b	$1/2 D_b$
11	$2D_b$	$1/2 D_b$
12	$5D_b$	$1/2 D_b$

Table 16.2 – Locations of the probes used for the convergence monitoring of the bluff body flame, where x and y denote the downstream and radial coordinates, respectively.

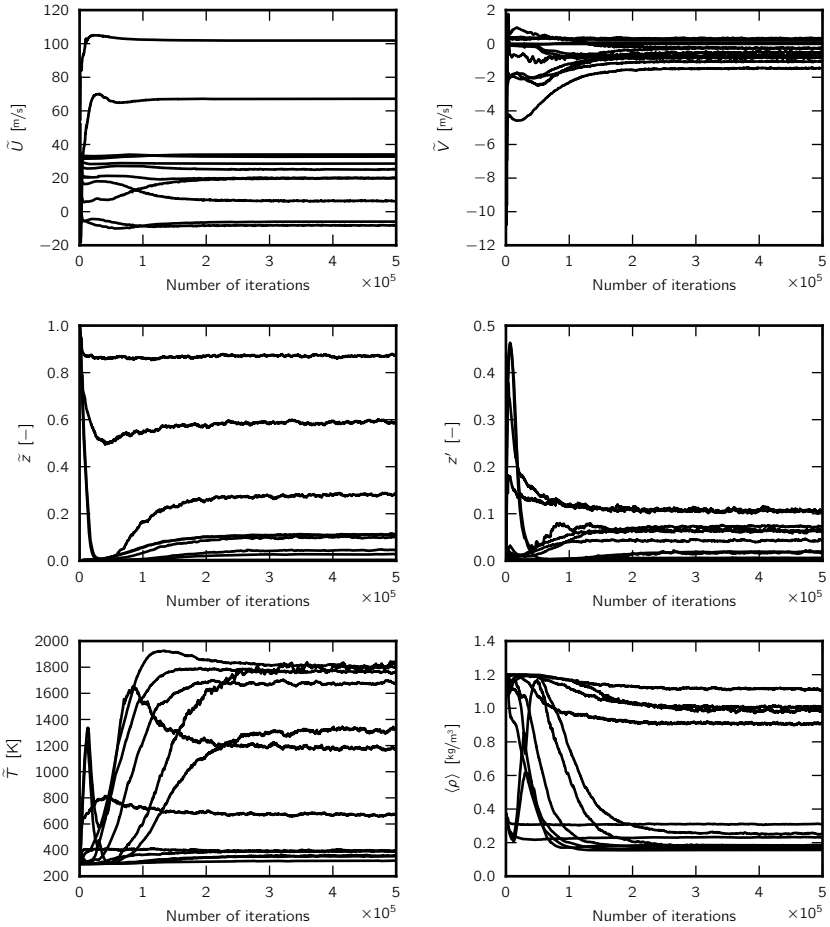

Figure 16.1 – Convergence histories for the mean axial and radial velocities, the mean mixture fraction, the RMS of the mixture fraction fluctuations, the mean temperature and mean density for the bluff body flame in the probe locations listed in Table 16.2.

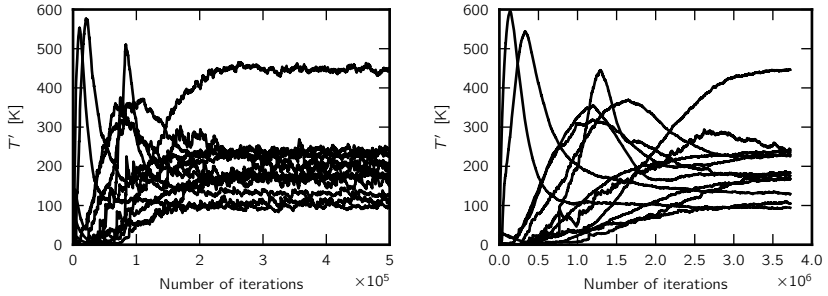

Figure 16.2 – Convergence histories of the RMS values of the temperature fluctuations for the bluff body flame with 20 particles per cell and a time-averaging factor of 5×10^3 (left) and 80×10^3 (right).

Radial profiles, comparing the mean axial and radial velocities of the RANS and JPDF simulations against the experimental data at downstream positions $0.2D_b$, $0.4D_b$, $0.8D_b$, $1.2D_b$, $1.8D_b$ and $3.4D_b$, are displayed in Figure 16.3. Except for the last cross-section, agreement with the experimental data is good. The undershoot of the axial velocity in the last position has also been observed by other researchers, e.g. by Muradoglu et al. [50]. The consistency between the RANS and JPDF mean velocities is given, the overlap is almost perfect.

At the same downstream positions, again comparing RANS, JPDF and experimental data, Figure 16.4 shows the radial profiles for the RMS of the fluctuating axial and radial velocities and Figure 16.5 the radial profiles of the turbulent shear stress. In the majority of the cross-sections the JPDF predictions of the Reynolds stress tensor components match the experimental data better than the ones obtained from the $k - \varepsilon$ model. This is attributed to the fact that the second-order moment closure consistent with Rotta's return to isotropy model provided by the SLM is better suited to this type of flow involving strongly curved stream lines in the recirculation zone.

In Figure 16.6 the radial profiles of the mean mixture fraction at downstream positions $0.26D_B$, $0.6D_b$, $0.9D_b$, $1.3D_b$, $1.8D_b$ and $2.4D_b$ are displayed. The simulation results match the experimental data well up to the last two sections, where there is quite a significant undershoot.

The radial profiles of the RMS values of the fluctuating mixture fraction are presented in Figure 16.7. Although the shape is recovered well, the

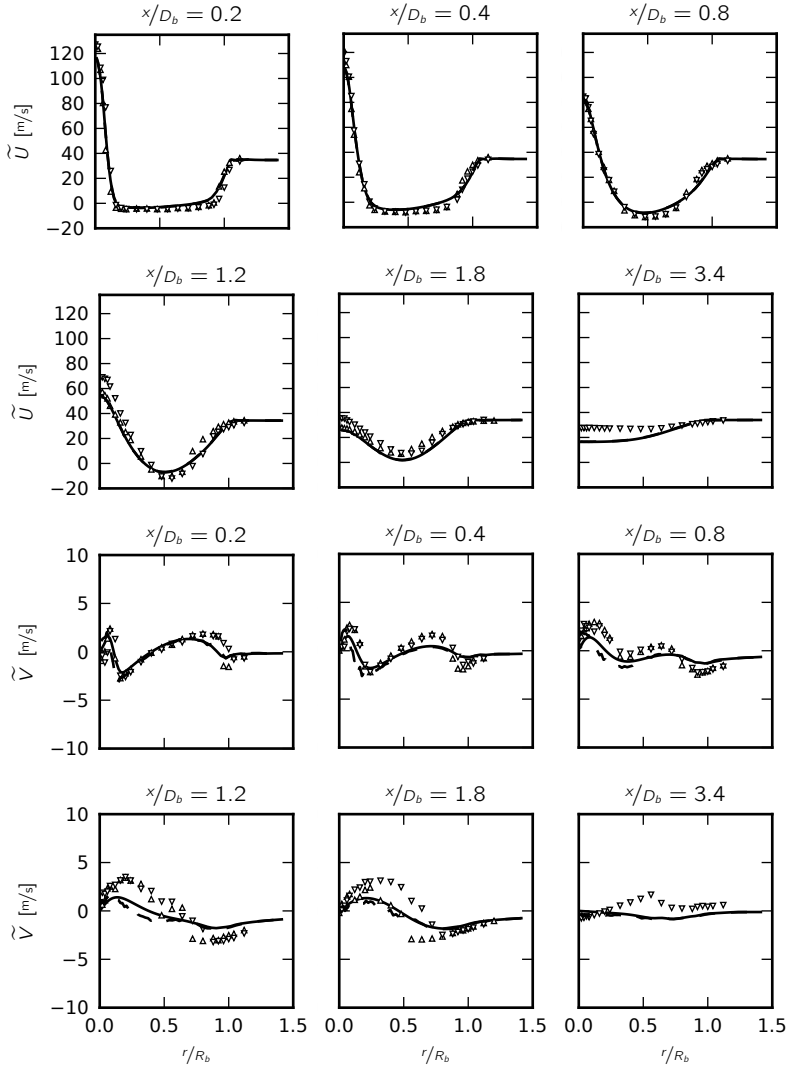

Figure 16.3 – Radial profiles of the mean axial (top two rows) and radial (bottom two rows) velocity for the bluff body flame at various downstream positions. The solid lines represent the RANS simulation results, the dashed lines the JPDF results and the symbols the experimental data.

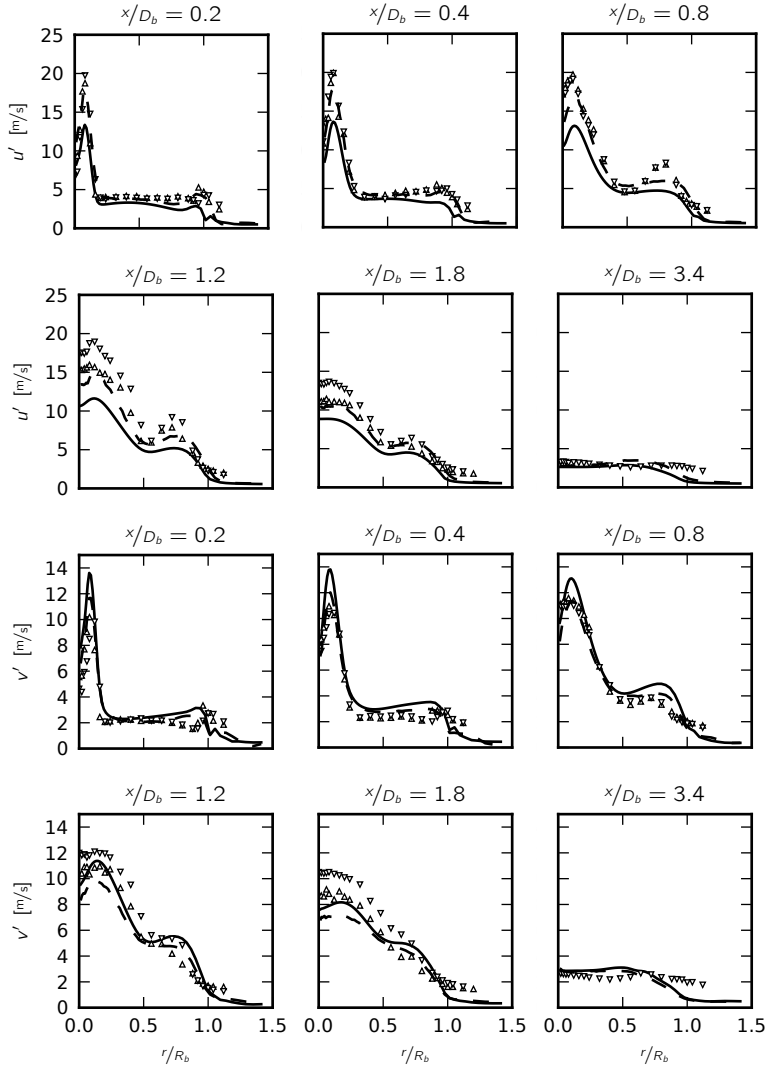

Figure 16.4 – Radial profiles of the axial (top two rows) and radial (bottom two rows) RMS velocity fluctuations for the bluff body flame at various downstream positions. The solid lines represent the RANS simulation results, the dashed lines the JPDF results and the symbols the experimental data.

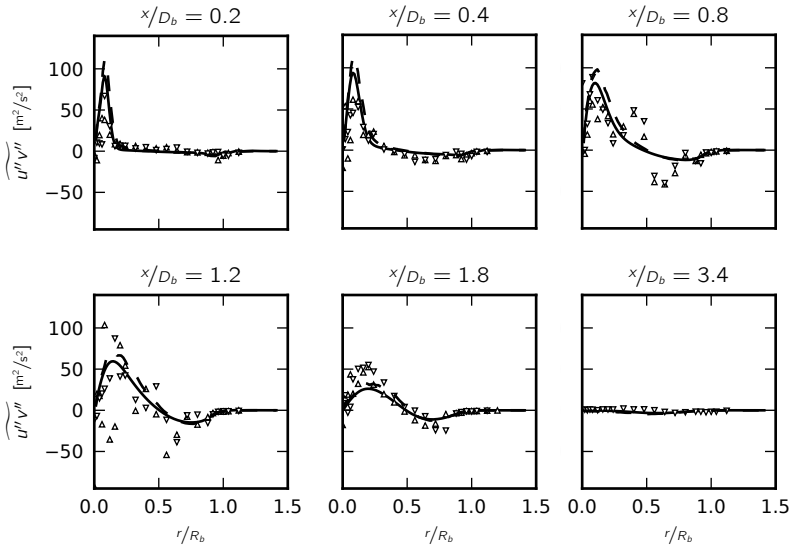

Figure 16.5 – Radial profiles of the turbulent shear stress for the bluff body flame at various downstream positions. The solid lines represent the RANS simulation results, the dashed lines the JPDF results and the symbols the experimental data.

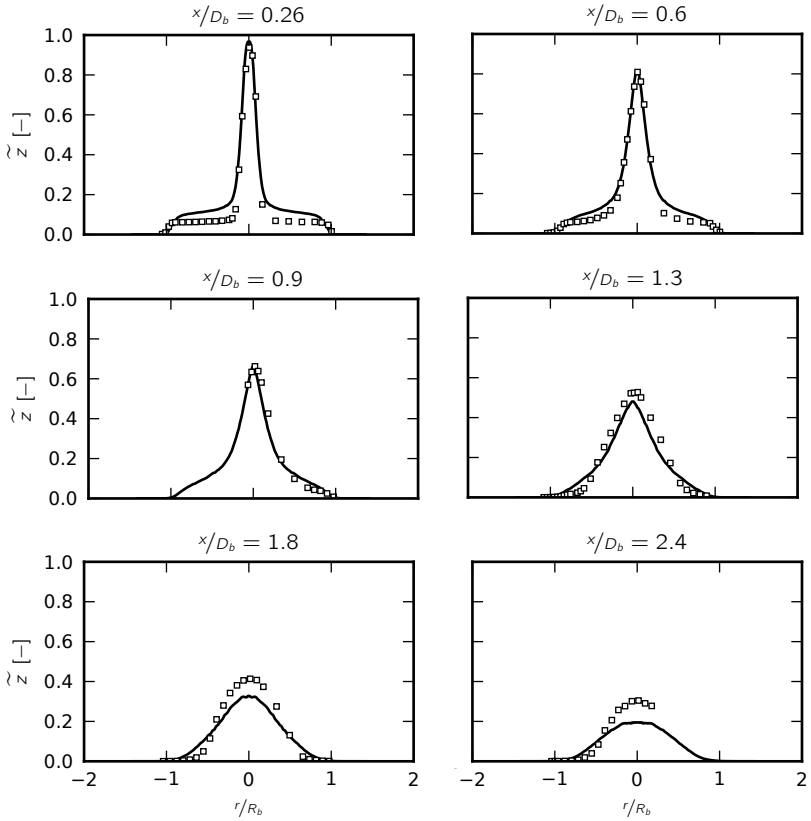

Figure 16.6 – Radial profiles of the mean mixture fraction for the bluff body flame at various downstream positions. The dashed lines represent the simulation results and the symbols the experimental data.

Series	Number of particles	Time averaging	Mesh resolution
1	20	5×10^3	80×80
1	40	5×10^3	80×80
1	80	5×10^3	80×80
1	160	5×10^3	80×80
2	20	5×10^3	80×80
2	20	10×10^3	80×80
2	20	20×10^3	80×80
2	20	40×10^3	80×80
3	40	5×10^3	40×40
3	40	5×10^3	60×60
3	40	5×10^3	80×80
3	40	5×10^3	100×100

Table 16.3 – Parameters of the bias convergence study.

gradients are too flat and the peaks are under or overpredicted.

Figures 16.8 and 16.9 show the radial profiles of the mean temperature and the RMS of the fluctuating temperature. The first two cross-section underpredict the mean temperature, while the last three overpredict it. The first three sections of the RMS profiles closely match the experimental data, while the deviations in the last three sections are more pronounced.

The radial profiles of the mean density and mean particle mass density are depicted in Figure 16.10. Internal consistency is very good, the maximum relative error is below 5%.

16.1 Convergence Study

In order to assess the convergence behaviour of the bias error with respect to the number of particles, the time-averaging factor and the grid resolution, three series of simulations have been run, varying these parameters as listed in Table 16.3.

The influence of the spatial discretisation error is illustrated in Figure 16.11. For the mean axial velocity, the RMS of the fluctuating axial velocity, the mean mixture fraction, the RMS of the mixture fraction fluctuations and the mean temperature as well as the RMS of its fluctuations,

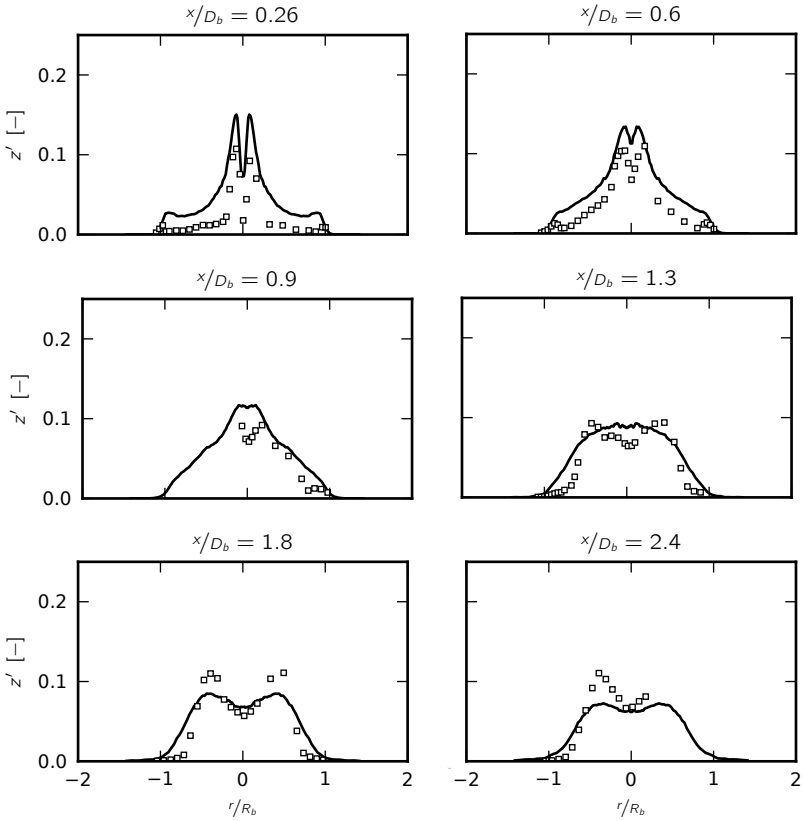

Figure 16.7 – Radial profiles of the RMS of the fluctuating mixture fraction for the bluff body flame at various downstream positions. The dashed lines represent the simulation results and the symbols the experimental data.

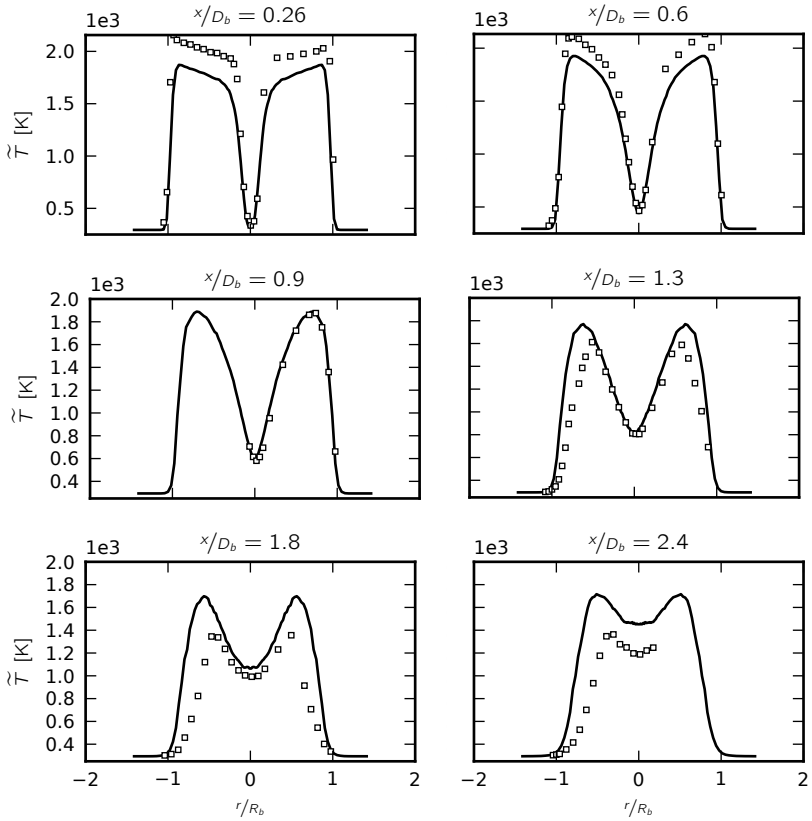

Figure 16.8 – Radial profiles of the mean temperature for the bluff body flame at various downstream positions. The dashed lines represent the simulation results and the symbols the experimental data.

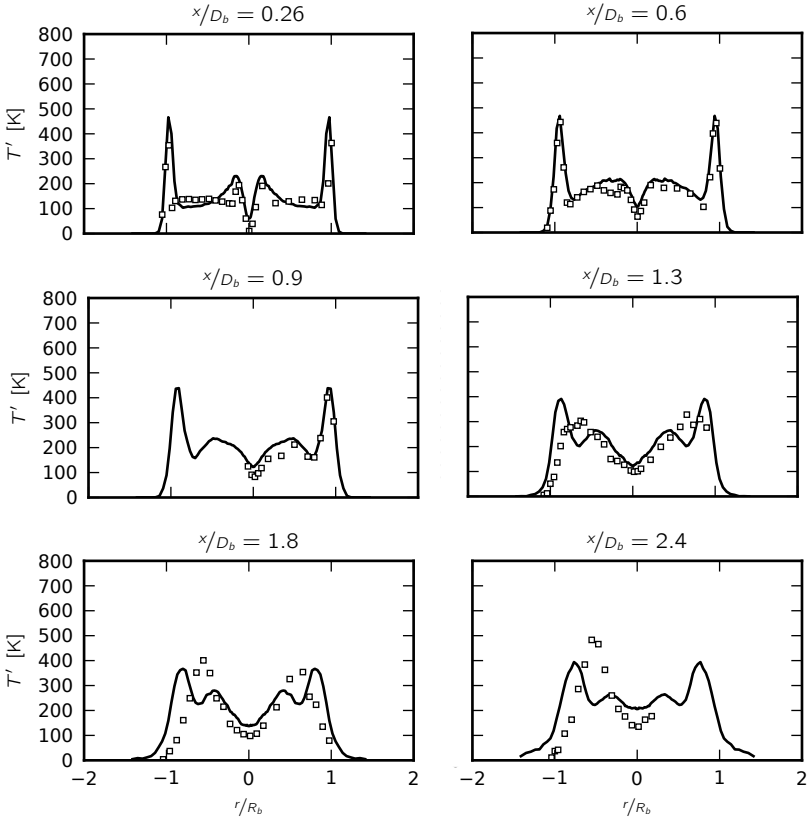

Figure 16.9 – Radial profiles of the RMS of the fluctuating temperature (bottom two rows) for the bluff body flame at various downstream positions. The dashed lines represent the simulation results and the symbols the experimental data.

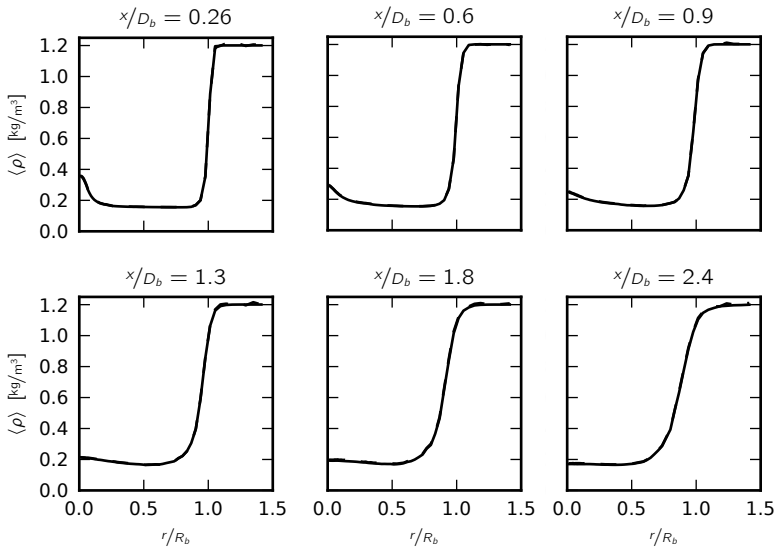

Figure 16.10 – Radial profiles of the mean density (solid line) and the particle mass density (dashed line) at various downstream positions.

profiles are shown at representative downstream positions for the grid resolutions 40×40, 60×60, 80×80 and 100×100, as described in Table 16.3. For the axial velocity and the RMS of its fluctuations, only the RANS simulation results are shown. As can be seen, for the mean axial velocity, the the grid resolution mainly influences the steepness of the gradients, while for the axial normal turbulent stress, the influence is particularly strong in the region behind the bluff body. The effect on the mean mixture fraction appears to be minor with respect to the RMS of the mixture fraction fluctuations, but these small deviations obviously have a strong impact on the mean temperature and its fluctuations. The radial cross sections for all variables at more positions are shown in Appendix A.

In order to quantify the discretisation error, the steady state values of the mean mixture fraction, temperature and density at probe locations 2, 5 and 9 are plotted against the inverse of the number of grid cells, M, in Figure 16.12. The lines are least-squares fits to the data points.

The bias error convergence in dependence of the number of particles and the time-averaging parameter is shown in Figure 16.13. Here, like for the mesh-convergence plots, the lines are least-squares fits to the data points and their slope is a measure for the bias error.

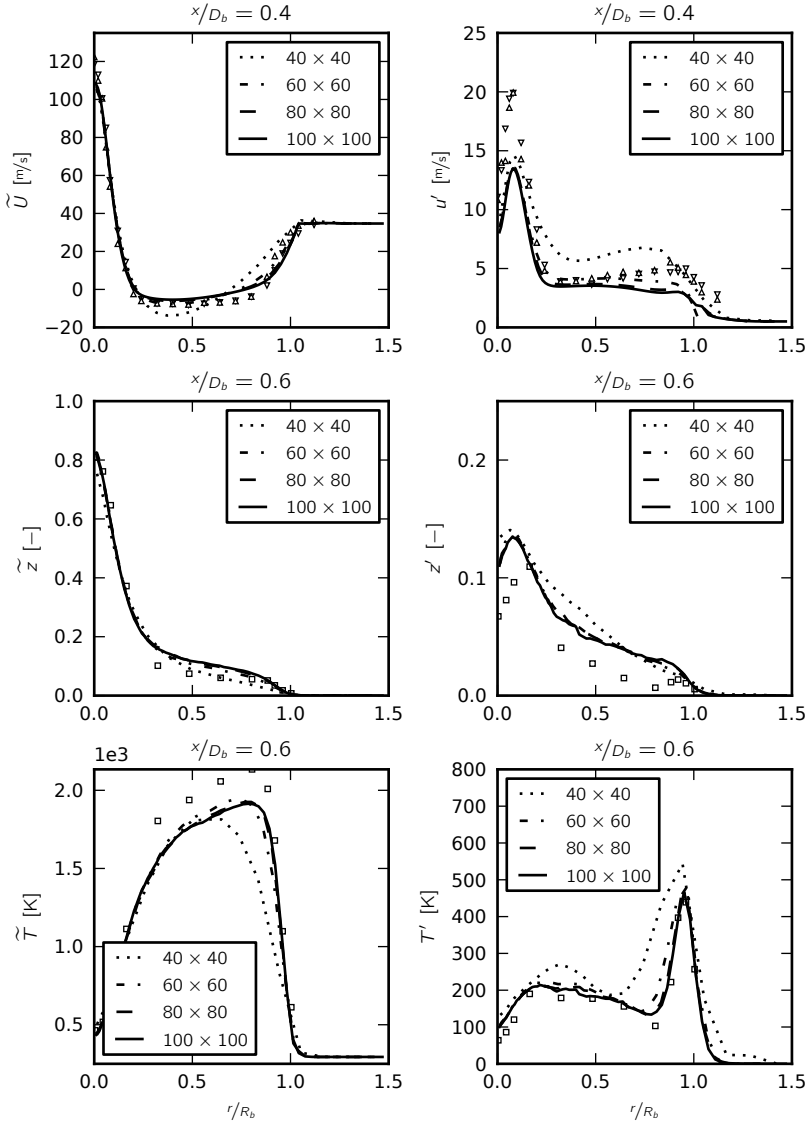

Figure 16.11 – Comparison showing the influence of the grid resolution at representative cross-sections of the means of the axial velocity, mixture fraction and temperature as well as the RMS values of their fluctuations.

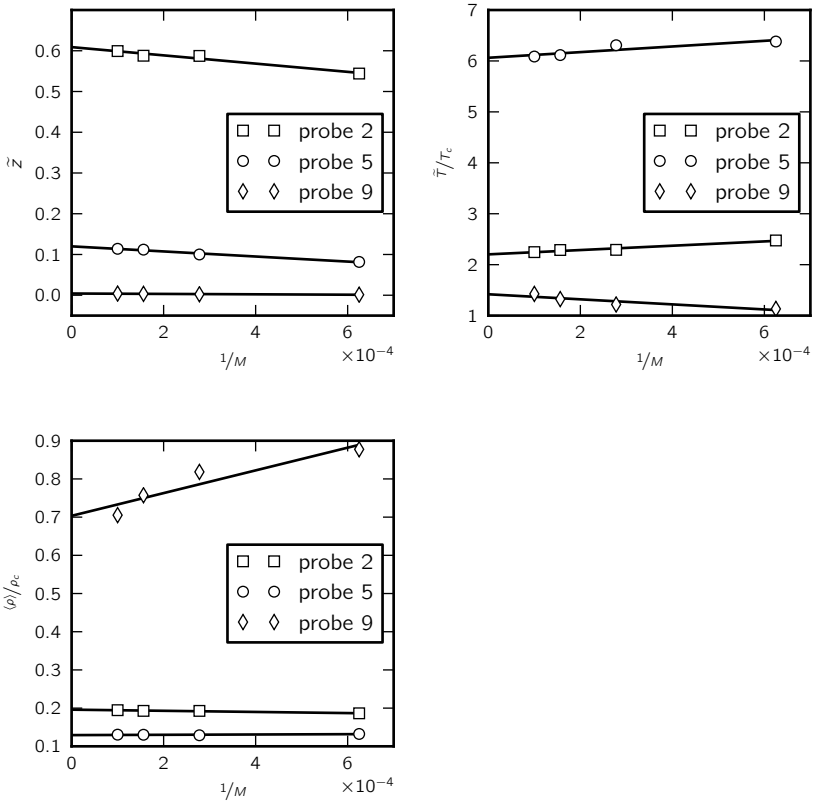

Figure 16.12 – Steady state values of the mean mixture fraction, mean temperature and mean density against the total number of grid cells M at probe locations 2, 5, and 9 (Table 16.2). T_c =294 K is the temperature of the co-flow, and ρ_c =1.20104$^{\mathrm{kg}}/_{\mathrm{m}^3}$ its density.

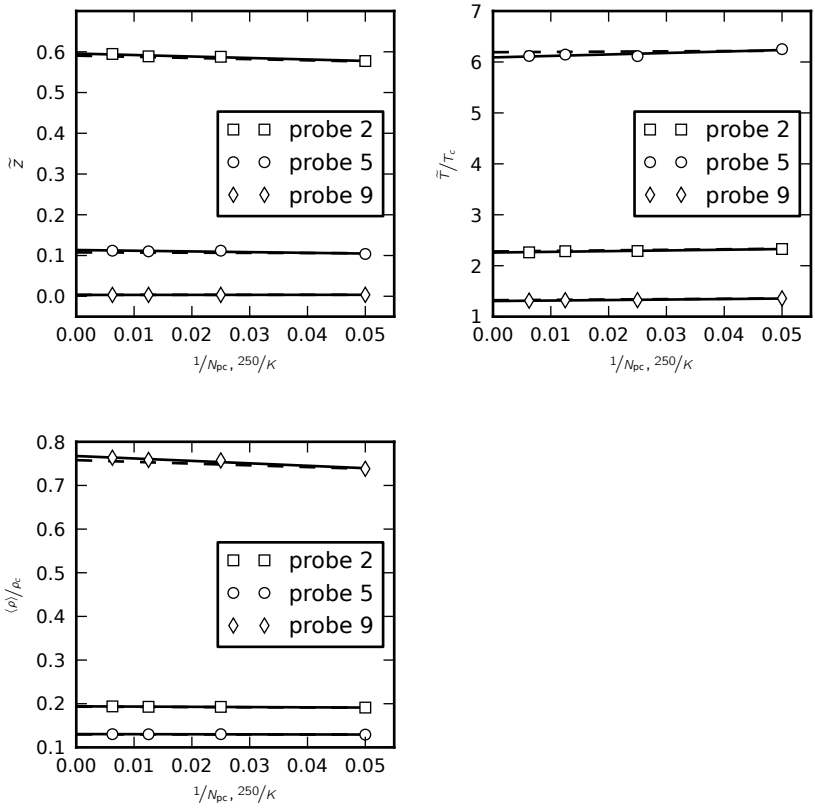

Figure 16.13 – Steady state values of the mean mixture fraction, mean temperature and mean density against the number of particles per cell N_{pc} (solid lines) and the time-averaging parameter K (dashed lines) at probe locations 2, 5, and 9 (Table 16.2). T_c =294 K is the temperature of the co-flow, and ρ_c =1.20104$^{kg}/_{m^3}$ its density.

17 Auto-Ignition Stabilised Burner

To demonstrate that the previously described algorithm and its implementation in OpenFOAM are applicable to complex geometries, a fully three-dimensional simulation of a burner with an auto-ignition stabilised flame has been performed. The set-up is inspired by that of sequential burners. Here, a hot air stream at 980 K enters a mixing chamber with a bulk velocity of $60\,^{\mathrm{m}}/_{\mathrm{s}}$, where a fuel nozzle adds nitrogen-diluted hydrogen, preheated to 750 K, to the stream. By mass, the fuel consists of 87% nitrogen and 13% hydrogen, and the mass flow rate is $6.8 \times 10^{-4}\,^{\mathrm{kg}}/_{\mathrm{s}}$. The mixing chamber is followed by the combustion chamber with a larger cross-section, in which the flow slows down and the flame can stabilise. The temperature of the gas stream is sufficiently high for auto-ignition to occur. Both, the mixing and the combustion chamber are rounded square ducts with edge lengths of $w_m = 60\,\mathrm{mm}$ and $w_c = 120\,\mathrm{mm}$, respectively. Their stream-wise extent is $L_m = 120\,\mathrm{mm}$ and $L_c = 200\,\mathrm{mm}$. The fuel nozzle attaches to the mixing chamber wall at downstream coordinate $x_n = 50\,\mathrm{mm}$ and has a diameter of $d_n = 6\,\mathrm{mm}$. It reaches to the centre line of the mixing chamber and has a stream-wise length of $L_n = 30\,\mathrm{mm}$. A sketch of the burner is displayed in Figure 17.1.

The turbulence at the inflows is assumed to be isotropic and its intensity $u'/\widetilde{U}$ has been chosen to be 10%. The turbulence dissipation has been estimated as

$$\varepsilon = \frac{C_\mu^{3/4} k^{3/2}}{\ell} \quad ,$$

where ℓ is a turbulence length scale, here estimated to be 20% of the inflow width and diameter, respectively. As in the previous simulations, the walls are treated as slip walls.

The laminar flamelet model used for the previous simulations is not applicable to this kind of combustion. Here, fuel and oxidiser are mixing before reaching the flame front, which is stabilised by auto-ignition. Both of these

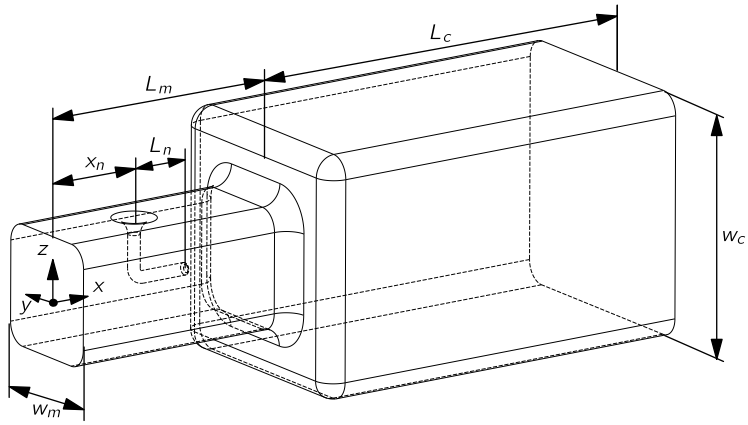

Figure 17.1 – Sketch of the auto-ignition stabilised burner with complex geometry.

phenomena cannot be described by the laminar flamelet assumption. Instead, a progress-variable based model proposed by Kulkarni and Polifke [34] is used. As hydrogen is used as the fuel, the mass fraction of water appears to be a natural candidate for the progress-variable. However, this choice alone does not capture the build-up of the radical pool during the induction phase of the auto-ignition. For this, the mass fraction of the intermediate species HO_2 is added. Hence, the progress variable Y_c is defined as

$$Y_c \equiv Y_{H_2O} + Y_{HO_2} \quad .$$

The normalised progress variable is obtained by division with the equilibrium state, i.e.

$$\mathrm{PV} \equiv \frac{Y_c}{Y_{c,\mathrm{eq}}} \equiv \frac{Y_{H_2O} + Y_{HO_2}}{Y_{H_2O,\mathrm{eq}} + Y_{HO_2,\mathrm{eq}}} \quad ,$$

where $Y_{c,\mathrm{eq}}$, $Y_{H_2O,\mathrm{eq}}$ and $Y_{HO_2,\mathrm{eq}}$ are the equilibrium progress variable and mass fractions, respectively. Performing zero-dimensional reactor simulations with the chemical software package Cantera [19] across the full mixture fraction range, the source term $\rho\dot{\omega}_c$ of the progress variable, the temperature and the density are tabulated as a function of the mixture fraction and the normalised progress variable. The hydrogen-air reaction mechanism by Ó Conaire et al. [56], which has been validated extensively for auto-ignition predictions, is used. In contrast to a real sequential burner, here

Parameter	Value	Model
CFL	0.1	Time-step calculation
C_0	1.2	SLM
C_ϕ	2	IEM
N_{FV}	50	Loose coupling
N_{MC}	200	Loose coupling
C_{min}	0.8	Particle number control
C_{max}	1.2	Particle number control
C_{diff}	0.05	Particle distribution correction
C_{pos}	0.2	Position correction
τ_U	10^{-4} s	Mean velocity correction
τ_k	10^{-4} s	TKE correction

Table 17.1 – Model parameters for the auto-ignition flame simulation.

the pressure is atmospheric in order to facilitate the source term tabulation. At high pressures, it proved to be difficult to obtain converged simulations for the zero-dimensional reactor simulations. As the goal of this simulation case is to demonstrate general applicability of the algorithm and its implementation, and not the accuracy of the combustion model, it was decided to perform the simulation at atmospheric pressure instead. Figure 17.2 shows the tabulated source term $\rho\dot{\omega}_c$.

The domain was discretised by 271924 tetrahedral cells, where local refinement near the surfaces and in the flame region downstream of the nozzle exit was employed. The surface mesh is depicted in Figure 17.3, where the shading indicates the different regions of the domain decomposition. For this simulation, the time-averaging parameter was chosen as $K = 10^3$ and in average 40 particles per cell were employed. The upper limit for the local time-stepping was set to $\kappa = 10$. 50 processors were used in this simulation. The remaining simulation parameters are listed in Table 17.1

Cross-sections in the $x - y$ plane of the $\widetilde{U}$ and $\widetilde{V}$ velocity components, the mean temperature and mean density, the mean mixture fraction and the mean normalised progress variable are shown in Figures 17.4 through 17.9.

Probes, aligned with the nozzle axis, were placed at a distance of 50 mm, 70 mm, 90 mm, 110 mm, 130 mm, 150 mm, 170 mm, 190 mm, 210 mm and 230 mm downstream of the nozzle exit. Convergence histories of the mean velocity components $\widetilde{U}$ and $\widetilde{V}$, the mean mixture fraction, the mean nor-

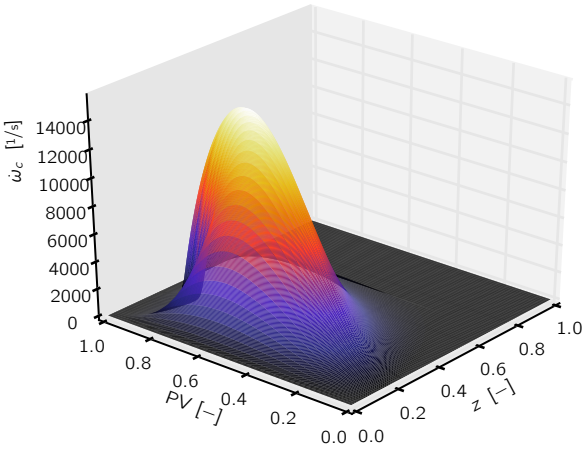

Figure 17.2 – Source term $\rho\dot{\omega}_c$ of the progress variable as a function of the mixture fraction and the normalised progress variable.

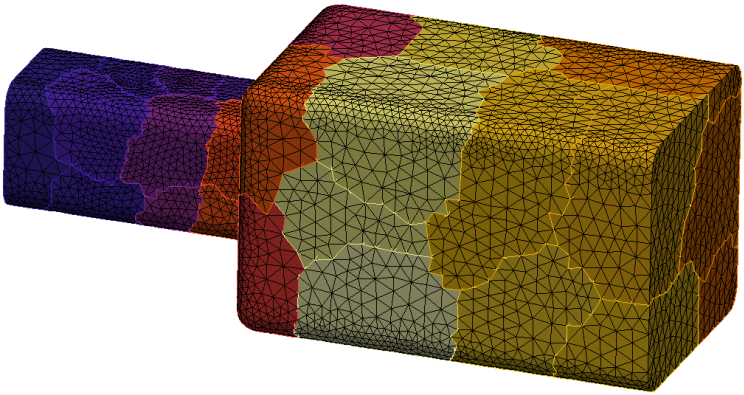

Figure 17.3 – Surface mesh of the auto-ignition stabilised burner. The shading indicates the different regions of the domain decomposition.

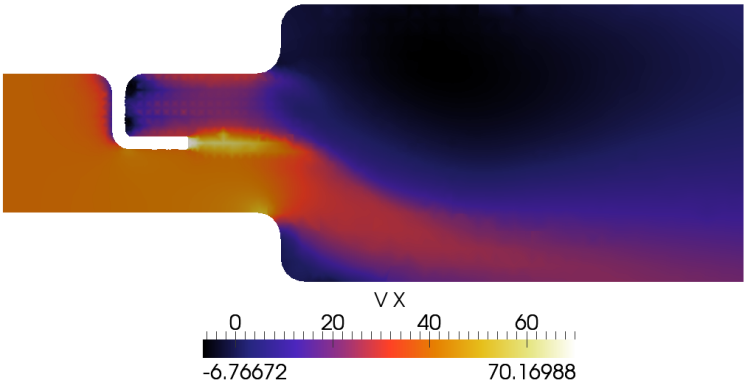

Figure 17.4 – Cross-section plot of the mean downstream velocity of the auto-ignition stabilised burner.

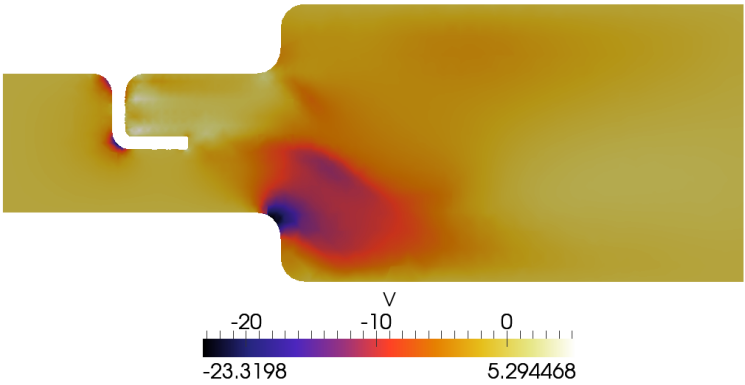

Figure 17.5 – Cross-section plot of the $\widetilde{V}$ velocity component of the auto-ignition stabilised burner.

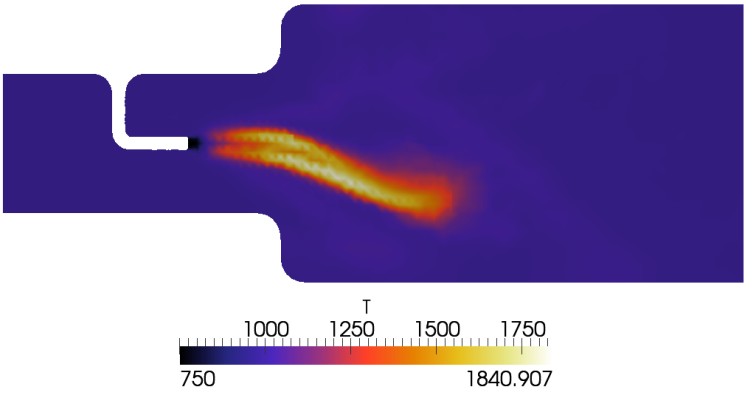

Figure 17.6 – Cross-section plot of the mean temperature of the auto-ignition stabilised burner.

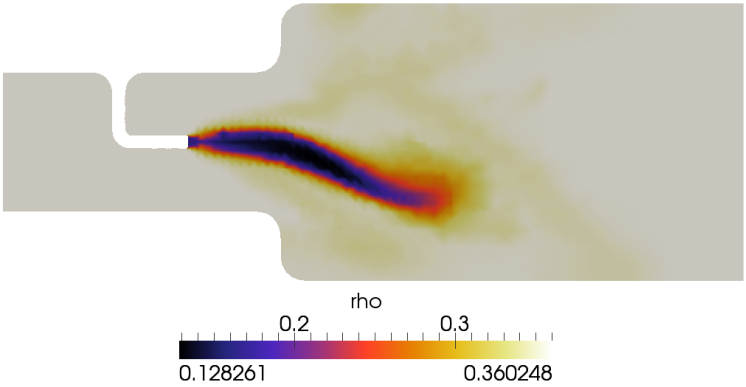

Figure 17.7 – Cross-section plot of the mean density of the auto-ignition stabilised burner.

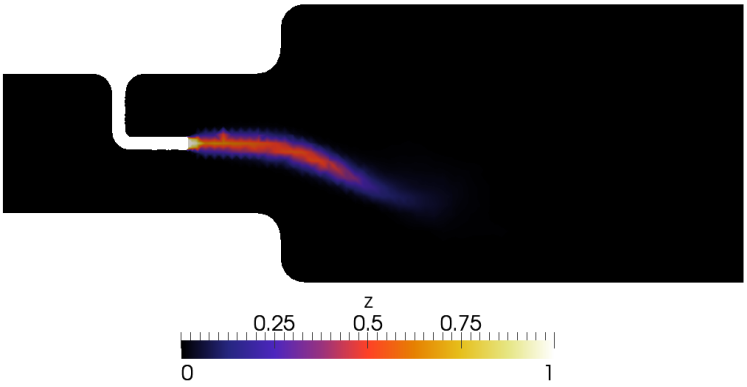

Figure 17.8 – Cross-section plot of the mean mixture fraction of the auto-ignition stabilised burner.

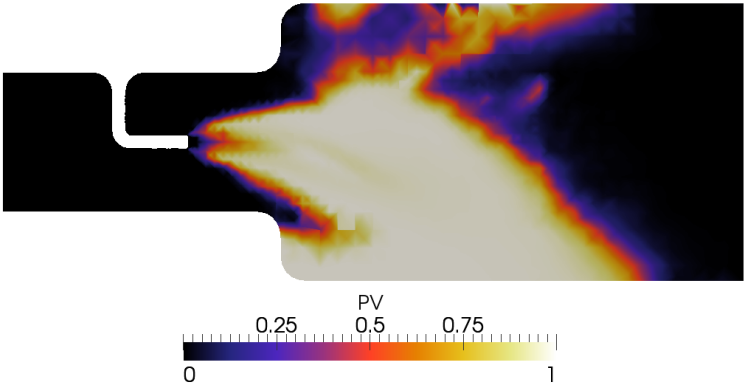

Figure 17.9 – Cross-section plot of the mean normalised progress variable of the auto-ignition stabilised burner.

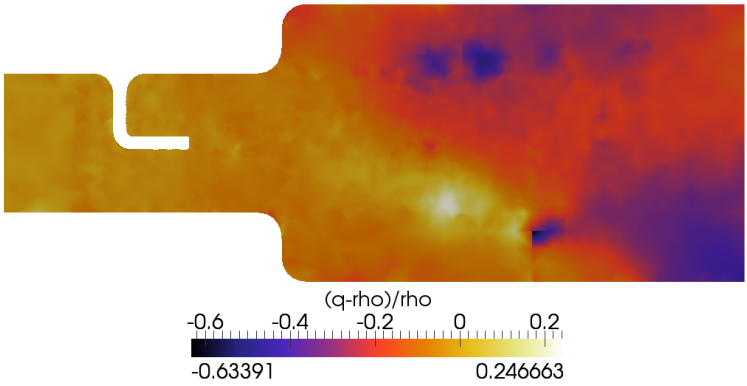

Figure 17.10 – Cross-section plot of the relative density error $^{q-\langle\rho\rangle}/_{\langle\rho\rangle}$ of the auto-ignition stabilised burner.

malised progress variable, the mean temperature and mean density are shown in Figure 17.11.

With this simulation, it has been demonstrated that the solution algorithm and its implementation in OpenFOAM as presented in this work are applicable to complex, general three-dimensional geometries and unstructured meshes.

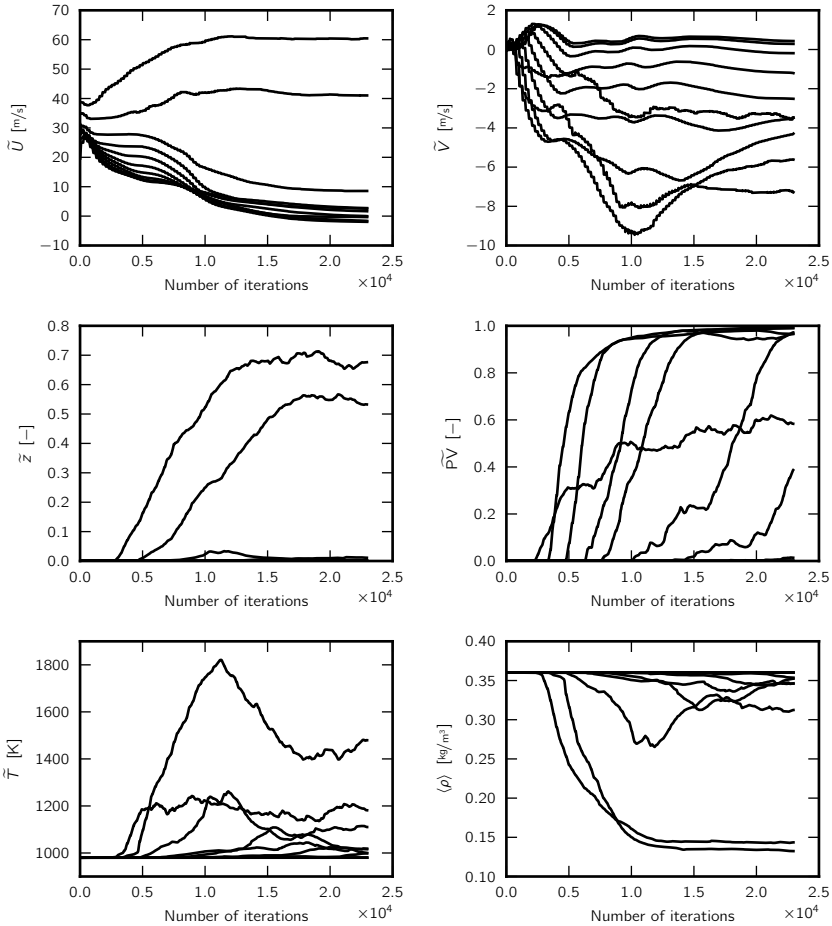

Figure 17.11 – Convergence histories for the $\widetilde{U}$ and $\widetilde{V}$ velocities, the mean mixture fraction, the mean normalised progress variable, the mean temperature and mean density for the auto-ignition stabilised burner.

18 Conclusions and Future Prospects

The solution of the governing equations for turbulent reactive flows is a very challenging problem. This is accentuated by the fact that for practical applications direct numerical simulation (DNS) is computationally far too expensive. Devising approximate models that are both efficient and describe the underlying physics accurately is a very complex task, and various trade-offs have to be made. These can be described in terms of the resolved scales, contrasting DNS, large eddy simulation (LES) and Reynolds averaged simulation. The models often take the form of moment-closures. The higher the moments are at which the closure is made, the more detailed, and often more accurate, is the description of the modelled physics. However, this goes hand in hand with increased computational costs. For reactive flow problems, the assumptions made in the moment closures are often very strong, rendering the models inappropriate for general purpose applications. For LES, the requirements placed on the modelling efforts are less stringent, as the level of description provided by the resolved scales is already very high. But the computational cost, especially associated with wall-bounded flows, where the boundary layer needs to be fully resolved, is often prohibitive. Transported joint probability density function (JPDF) methods offer an option that strikes a good balance between the accuracy of the physical description and the computational feasibility. This is especially the case when using a hybrid formulation that combines the advantages of both Reynolds averaged equations and the higher level of description of the transported JPDF methodology.

Reasons for the slow adoption of the transported JPDF methods are their conceptional complexity, numerical difficulties and the non-standard solution algorithms that are required. With this work, a general purpose simulation tool for turbulent reactive flows based on a hybrid FV/JPDF algorithm using a Lagrangian particle Monte-Carlo method has been presented. It has been implemented using the well known, very capable open-source

framework OpenFOAM, profiting from its large and mature infrastructure, its wide-spread adoption in both academia and industry as well as from its standardised work-flow. Due to a very modular implementation and open architecture, the simulation code represents an excellent platform for future model development efforts. Thanks to a novel coupling scheme, the hybrid solver provides both good stability and a low bias error. Efficiency enhancing algorithms, namely a novel particle number control scheme and a local time-stepping method have been implemented.

In a series of validation simulations of increasing complexity, internal consistency has been demonstrated. Despite using the simplest viable models for the molecular mixing and the turbulent chemistry, good agreement with experimental data was achieved. In a first simulation set-up, a non-reacting propane jet in a slow co-flow of air has been simulated in order to asses the internal consistency, excluding potential errors introduced by faulty or inappropriate chemistry models or unsuitable turbulence models. Subsequently, the Sandia flame D, a piloted, partially-premixed methane-air jet flame, has been simulated, achieving satisfactory results. The complexity of the bluff body flow simulation was considerably higher, posing a much greater challenge to the particle tracking and consistency algorithms. That the solution algorithm is able to accurately predict complex flame geometries was demonstrated with the simulation of a bluff body stabilised methane-hydrogen-air flame. The capability of this implementation to deal with complex geometries has been shown in the last simulation, in which the algorithm was applied to a sequential burner-like set-up with an auto-ignition stabilised flame.

Future development of the algorithm and its implementation should include improvements of the particle path integration. The decay to a first-order scheme in the case of wall-interaction in particular should be addressed. The implementation of a time-accurate integration scheme for the particle velocity and position evolution based on the work by Hegetschweiler [27] appears to be a possible starting point. Also, devising and implementing conservative interpolation schemes could potentially improve the simulation results. Profiling efforts have shown that a large part of the simulation cost is due to the interpolation of field variables to the particle locations. Hence, efficiency gains in this area are expected to have a strong impact on the overall simulation cost. Even larger efficiency gains could be expected from a *zonal* hybrid model, where the JPDF transport equation is only solved in regions of special interest, e.g. near the flame front. Apart from potential algorithmic improvements, more sophisticated combustion and mixing mod-

els are of prime interest, such as the reactive PSP model by Hegetschweiler et al. [26] which is capable of predicting local extinction and reignition phenomena. The current implementation should be extensible for the use in the LES context, the so-called filtered density function (FDF) methodology. Even areas of applications unrelated to turbulent reactive flows, such as flows in porous media, are imaginable. The framework presented with this work should provide a solid platform, allowing for rapid implementations and efficient evaluation of future model developments.

Part IV
Appendices

A Grid Convergence Results

Here, further results for the convergence study presented in Section 16 are shown, comparing the mesh resolutions 40×40, 60×60, 80×80 and 100×100.

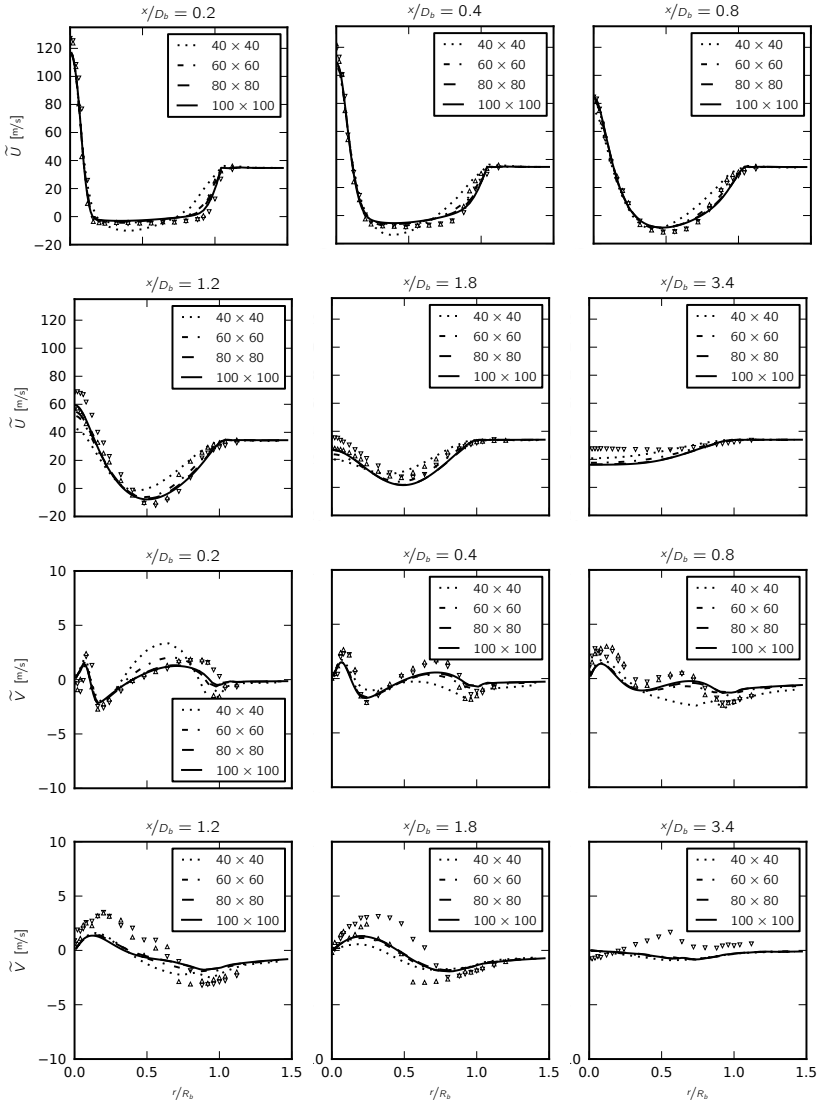

Figure A.1 – Radial profiles of the mean axial (top two rows) and radial (bottom two rows) velocity for the bluff body flame at various downstream positions. The lines represent different grid resolutions, the dashed lines the JPDF results and the symbols the experimental data.

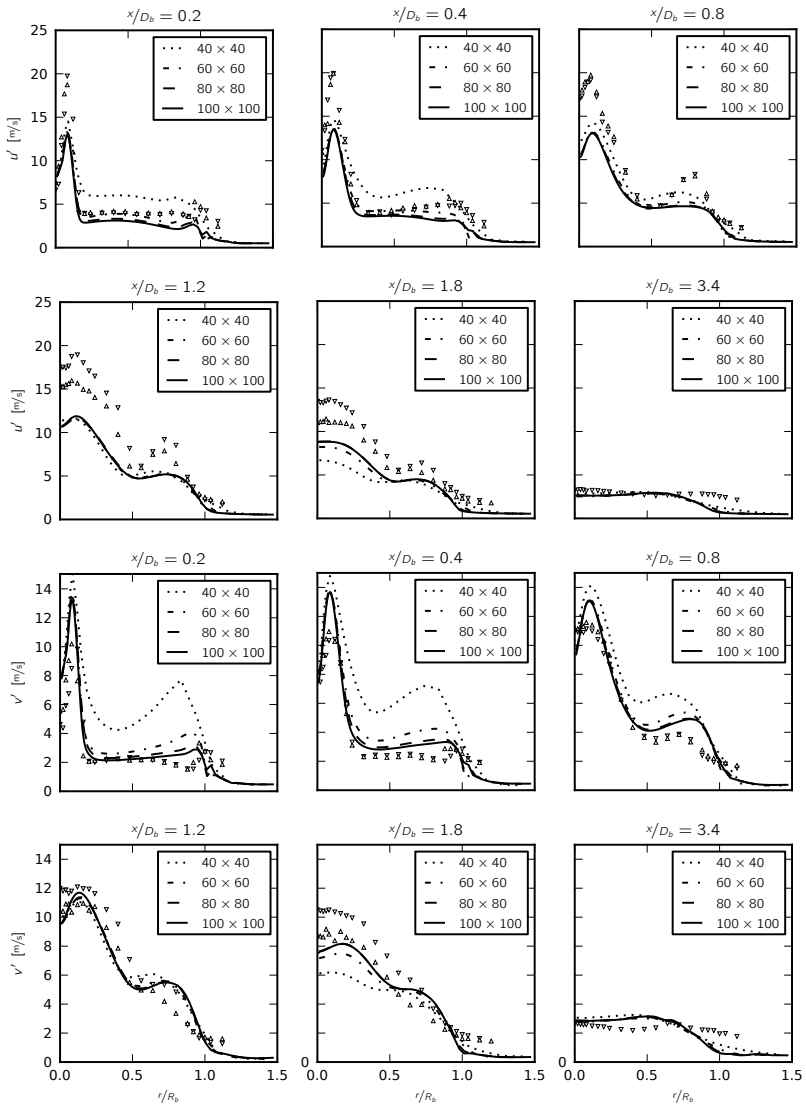

Figure A.2 – Radial profiles of the RMS values of the axial (top two rows) and radial (bottom two rows) velocity fluctuations for the bluff body flame at various downstream positions. The lines represent different grid resolutions and the symbols the experimental data.

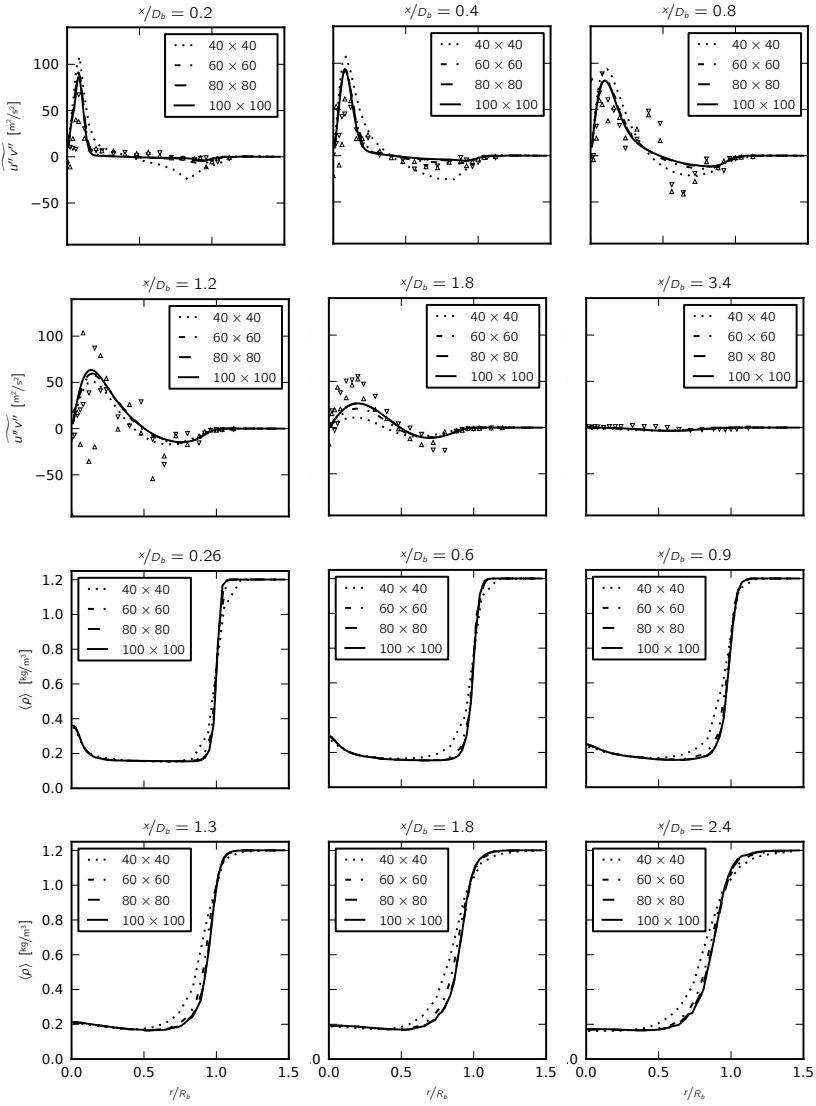

Figure A.3 – Radial profiles of the turbulent shear stress (top two rows) and the mean density (bottom two rows) for the bluff body flame at various downstream positions. The lines represent different grid resolutions and the symbols the experimental data.

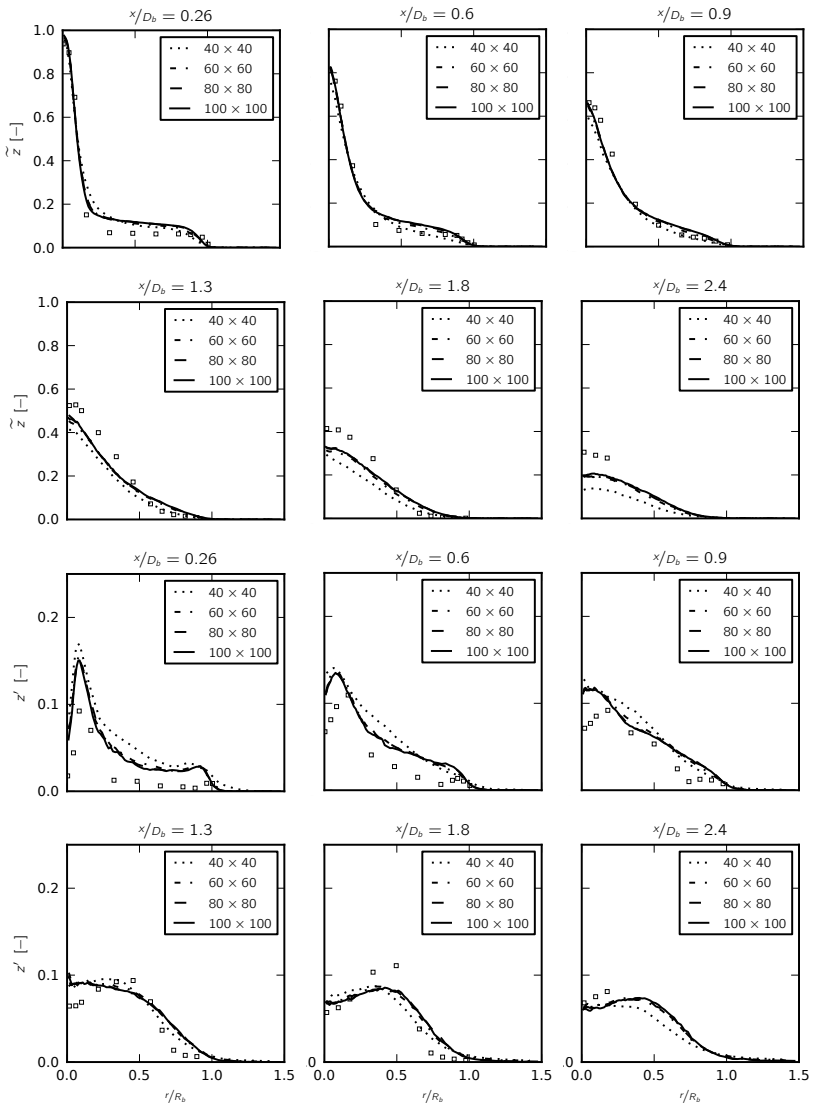

Figure A.4 – Radial profiles of the mean mixture fraction (top two rows) and the RMS values of its fluctuations (bottom two rows) for the bluff body flame at various downstream positions. The lines represent different grid resolutions and the symbols the experimental data.

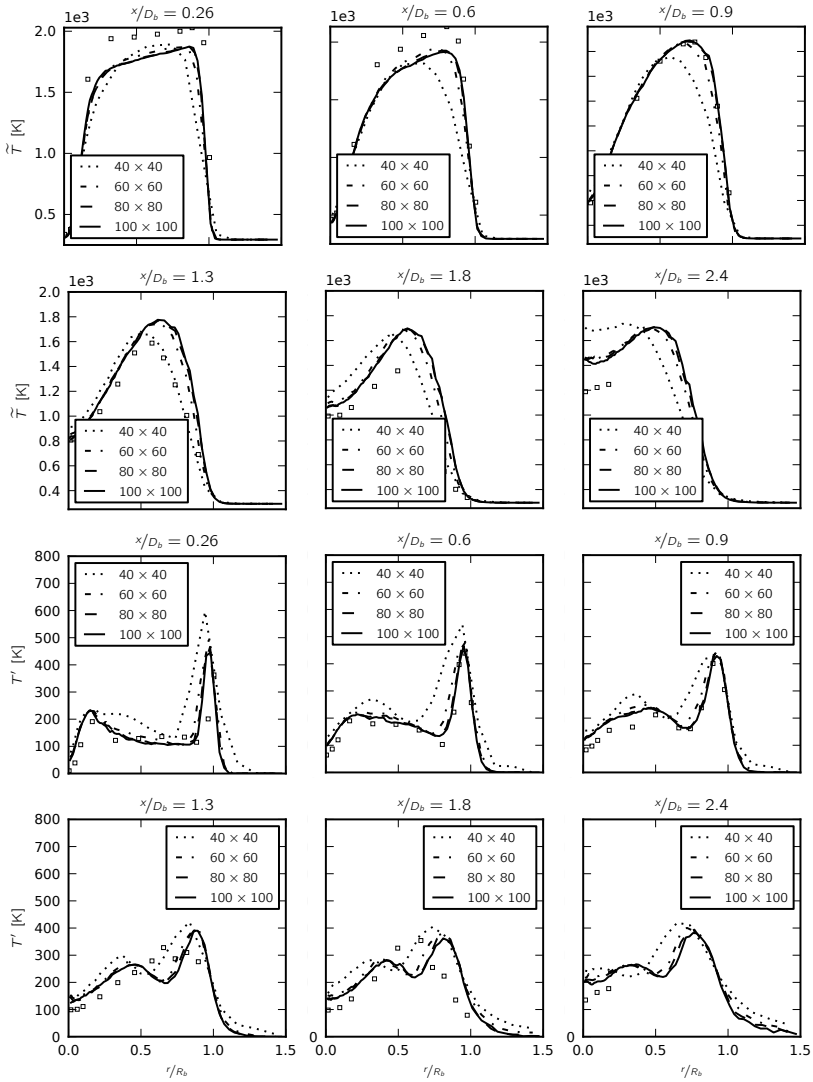

Figure A.5 – Radial profiles of the mean temperature (top two rows) and the RMS values of its fluctuations (bottom two rows) for the bluff body flame at various downstream positions. The lines represent different grid resolutions and the symbols the experimental data.

References

[1] B.S. Baldwin, T.J. Barth, Technical Report 102847, NASA, 1990. URL: http://hdl.handle.net/2060/19910000939.

[2] B.S. Baldwin, H. Lomax, AIAA Paper (1978) 78–257.

[3] R. Barlow, 2010, Sandia National Laboratories TNF Workshop. URL: http://www.ca.sandia.gov/TNF.

[4] R. Barlow, J. Frank, A. Karpetis, J.Y. Chen, Combust Flame 143 (2005) 433–449. doi:10.1016/j.combustflame.2005.08.017.

[5] R.S. Barlow, J.H. Frank, Symp Int Combust Proc 27 (1998) 1087–1095. doi:10.1016/S0082-0784(98)80510-9.

[6] R. Bilger, Symp Int Combust Proc 22 (1989) 475–488. doi:10.1016/S0082-0784(89)80054-2.

[7] D. Bradley, P. Gaskell, X. Gu, Combust Flame 96 (1994) 221–248. doi:10.1016/0010-2180(94)90011-6.

[8] D. Bradley, P. Gaskell, X. Gu, Symp Int Combust Proc 27 (1998) 1199–1206. doi:10.1016/S0082-0784(98)80523-7.

[9] K. Bray, P.A. Libby, J. Moss, Combust Flame 61 (1985) 87–102. doi:10.1016/0010-2180(85)90075-6.

[10] S. Burke, T. Schumann, Proceedings of the Symposium on Combustion 1 (1928) 2–11. doi:10.1016/S1062-2888(65)80003-X.

[11] M.W. Chase, Jr., C.A. Davies, J.R. Downey, Jr., D.J. Frurip, R.A. McDonald, A.N. Syverud, NIST JANAF THERMOCHEMICAL TABLES, National Institute of Standards and Technology, 1985.

[12] M. Chen, M. Herrmann, N. Peters, Proc Combust Inst 28 (2000) 167–174. doi:10.1016/S0082-0784(00)80208-8.

[13] R.L. Curl, AIChE Journal 9 (1963) 175–181. doi:10.1002/aic.690090207.

[14] B.B. Dally, D.F. Fletcher, A.R. Masri, Combust Theor Model 2 (1998) 193–219. doi:10.1088/1364-7830/2/2/006.

[15] A. Einstein, Annalen der Physik 322 (1905) 549–560. doi:10.1002/andp.19053220806.

[16] J.H. Ferziger, M. Perić, Computational Methods for Fluid Dynamics, 3 ed., Springer, 2002.

[17] R.O. Fox, Computational models for turbulent reacting flows, Cambridge University Press, Cambridge, 2003. doi:10.1017/CBO9780511610103.

[18] C.W. Gardiner, Handbook of Stochastic Methods, 2 ed., Springer, 1985.

[19] D.G. Goodwin, Cantera: An object-oriented software toolkit for chemical kinetics, thermodynamics, and transport processes, 2012. URL: http://code.google.com/p/cantera.

[20] M.L. Hack, Joint Probability Density Function (PDF) Closure of Turbulent Premixed Flames, Ph.D. thesis, ETH Zürich, 2011. doi:10.3929/ethz-a-007052611.

[21] J. Hackett, S.B. Pope, AIAA J 16 (1978) 279–281. doi:10.2514/3.7521.

[22] W.K. Hastings, Biometrika 57 (1970) 97–109. doi:10.1093/biomet/57.1.97.

[23] D. Haworth, Progr Energ Combust Sci 36 (2010) 168–259. doi:10.1016/j.pecs.2009.09.003.

[24] D.C. Haworth, S.B. Pope, Phys Fluid 29 (1986) 387–405. doi:10.1063/1.865723.

[25] M. Hegetschweiler, C. Handwerk, P. Jenny, Combust Sci Tech 182 (2010) 480–490. doi:10.1080/00102200903462987.

[26] M. Hegetschweiler, B.T. Zoller, P. Jenny, Combust Flame 159 (2012) 734–747. doi:10.1016/j.combustflame.2011.08.018.

[27] M.J. Hegetschweiler, Hybrid PDF algorithm and PDF modeling of partially premixed turbulent combustion, Ph.D. thesis, ETH Zürich, 2010. doi:10.3929/ethz-a-006409982.

[28] C. Hirsch, Numerical Computation of Internal and External Flow, volume 1, 2 ed., Butterworth-Heinemann, 2007.

[29] M.K. Hubbert, Spring Meeting of the Southern District Division of Production, American Petroleum Institute, 1956, pp. 1–57.

[30] Jayesh, S.B. Pope, Technical Report FDA 95–05, Cornell University report, 1995. URL: http://tcg.mae.cornell.edu/pubs.html.

[31] P. Jenny, S.B. Pope, M. Muradoglu, D.A. Caughey, J Comput Phys 166 (2001) 218–252. doi:10.1006/jcph.2000.6646.

[32] W.P. Jones, B.E. Launder, International Journal of Heat and Mass Transfer 15 (1972) 301–314. doi:10.1016/0017-9310(72)90076-2.

[33] A.N. Kolmogorov, Izvestia Academy of Sciences, USSR; Physics 6 (1942) 56–58.

[34] R. Kulkarni, W. Polifke, J Combust 2012 (2012) 12. doi:10.1155/2012/780370.

[35] K.K. Kuo, Principles of Combustion, 2 ed., John Wiley, 2005.

[36] V.R. Kuznetsov, Fluid Dynamics 17 (1982) 815–820. doi:10.1007/BF01090372.

[37] P. Langevin, Comptes rendus de l'Académie des sciences 146 (1908) 530—533. URL: http://www.biodiversitylibrary.org/page/7093597.

[38] B.E. Launder, A. Morse, W. Rodi, D.B. Spalding, Technical Report 19730019433, NASA, 1973. URL: http://hdl.handle.net/2060/19730019433.

[39] B.E. Launder, B.I. Sharma, Letters in Heat and Mass Transfer 1 (1974) 131–137. doi:10.1016/0094-4548(74)90150-7.

[40] D.S. Lemons, A. Gythiel, American Journal of Physics 65 (1997) 1079–1081. doi:10.1119/1.18725.

[41] S.K. Liew, K.N.C. Bray, J.B. Moss, Combust Sci Tech 27 (1981) 69–73. doi:10.1080/00102208108946973.

[42] N.N. Mansour, J. Kim, P. Moin, J Fluid Mech 194 (1988) 15–44. doi:10.1017/S0022112088002885.

[43] A. Masri, J. Kelman, B. Dally, Symp Int Combust Proc 27 (1998) 1031–1038. doi:10.1016/S0082-0784(98)80503-1.

[44] A.R. Masri, 2012, Bluff-body flows and flames. URL: http://sydney.edu.au/engineering/aeromech/thermofluids/bluff.htm.

[45] J.J. McGuirk, W. Rodi, Selected papers from the First International Symposium on Turbulent Shear Flows: The Pennsylvania State University, University Park, Pennsylvania, USA, pp. 71–83.

[46] D.W. Meyer, P. Jenny, J Comput Phys 226 (2007) 1859–1873. doi:10.1016/j.jcp.2007.06.014.

[47] D.W. Meyer, P. Jenny, Combust Flame 155 (2008) 490–508. doi:10.1016/j.combustflame.2008.07.002.

[48] H. Möbus, P. Gerlinger, D. Brüggemann, Combust Flame 124 (2001) 519–534. doi:10.1016/S0010-2180(00)00207-8.

[49] A.P. Morse, Axisymmetric Free Shear Flows with and Without Swirl, Ph.D. thesis, University of London, 1980. URL: http://books.google.ch/books?id=Uk7lHwAACAAJ.

[50] M. Muradoglu, K. Liu, S.B. Pope, Combust Flame 132 (2003) 115–137. doi:10.1016/S0010-2180(02)00430-3.

[51] M. Muradoglu, S.B. Pope, AIAA J 40 (2002) 1755–1763. doi:10.2514/2.1880.

[52] M. Muradoglu, S.B. Pope, D.A. Caughey, J Comput Phys 172 (2001) 841–878. doi:10.1006/jcph.2001.6861.

[53] C. Müller, H. Breitbach, N. Peters, Symp Int Combust Proc 25 (1994) 1099–1106. doi:10.1016/S0082-0784(06)80747-2.

[54] V.W. Nee, L.S.G. Kovasznay, Phys Fluid 12 (1969) 473–484. doi:10.1063/1.1692510.

[55] M.B. Nik, S.L. Yilmaz, P. Givi, M.R. H. Sheikhi, S.B. Pope, AIAA J 48 (2010) 1513–1522. doi:10.2514/1.J050154.

[56] M. Ó Conaire, H.J. Curran, J.M. Simmie, W.J. Pitz, C.K. Westbrook, Int J Chem Kinet 36 (2004) 603–622. doi:10.1002/kin.20036.

[57] S. Osher, J.A. Sethian, J Comput Phys 79 (1988) 12–49. doi:10.1016/0021-9991(88)90002-2.

[58] N. Peters, Proc Combust Inst 21 (1986) 1231–1250. doi:10.1016/S0082-0784(88)80355-2.

[59] N. Peters, Turbulent Combustion, Cambridge University Press, 2000.

[60] H. Pitsch, 2005, FlameMaster, A C++ Computer Program for 0D Combustion and 1D Laminar Flame Calculations. URL: http://www.stanford.edu/group/pitsch/FlameMaster.htm.

[61] T. Poinsot, D. Veynante, Theoretical and Numerical Combustion, Edwards, 2001.

[62] S.B. Pope, Progr Energ Combust Sci 11 (1985) 119–192. doi:10.1016/0360-1285(85)90002-4.

[63] S.B. Pope, Annu Rev Fluid Mech 26 (1994) 23–63. doi:10.1146/annurev.fl.26.010194.000323.

[64] S.B. Pope, Phys Fluid 6 (1994) 973–985. doi:10.1063/1.868329.

[65] S.B. Pope, J Comput Phys 117 (1995) 332–349. doi:10.1006/jcph.1995.1070.

[66] L. Prandtl, Zeitschrift für Angewandte Mathematik und Mechanik 5 (1925) 136–139.

[67] L. Prandtl, K. Wiegehardt, Nachr. Akad. Wiss. Göttingen Math. Phys. Kl. (1945) 6–19.

[68] M.B. Priestley, Spectral Analysis and Time Series, Academic Press, San Diego, 1981.

[69] W. Rodi, The Prediction of Free Turbulent Boundary Layers By Use of a Two Equation Model of Turbulence, Ph.D. thesis, Imperial College (University of London), 1973.

[70] J.P.H. Sanders, A.P.G.G. Lamers, Combust Flame 96 (1994) 22–33. doi:10.1016/0010-2180(94)90155-4.

[71] R.W. Schefer, R.W. Dibble, 24th AIAA Aerospace Sciences Meeting, volume 24, pp. 1–11.

[72] R.W. Schefer, V. Hartmann, R.W. Dibble, AIAA J 25 (1987) 1318–1330. doi:10.2514/3.9786.

[73] R.W. Schefer, S.C. Johnston, R.W. Dibble, F.C. Gouldin, W. Kollmann, Technical Report SAND86-8217, Sandia National Laboratories, Livermore, CA, 1985.

[74] C. Schneider, A. Dreizler, J. Janicka, E. Hassel, Combust Flame 135 (2003) 185–190. doi:10.1016/S0010-2180(03)00150-0.

[75] A.M.O. Smith, T. Cebeci, Technical Report DAC 33735, Douglas aircraft division, 1967.

[76] G.P. Smith, D.M. Golden, M. Frenklach, N.W. Moriarty, B. Eiteneer, M. Goldenberg, C.T. Bowman, R.K. Hanson, S. Song, W.C.J. Gardiner, V.V. Lissianski, Z. Qin, 1996, GRI Mech. URL: http://www.me.berkeley.edu/gri_mech/.

[77] M. von Smoluchowski, Annalen der Physik (1906). doi:10.1002/andp.19063261405.

[78] P.R. Spalart, S.R. Allmaras, AIAA Paper 1992-0439, pp. 1–22. doi:10.2514/6.1992-439.

[79] S. Subramaniam, D.C. Haworth, International Journal of Engine Research 1 (2000) 171–190. doi:10.1243/1468087001545128.

[80] S. Subramaniam, S.B. Pope, Combustion and Flame 115 (1998) 487–514. doi:10.1016/S0010-2180(98)00023-6.

[81] P.R. Van Slooten, Jayesh, S.B. Pope, Phys Fluid 10 (1998) 246–265. doi:10.1063/1.869564.

[82] H. Wang, Y. Chen, Fluid Dynamics Research 37 (2005) 133. doi:10.1016/j.fluiddyn.2005.02.004.

[83] D.C. Wilcox, AIAA J 26 (1988) 1299–1310. doi:10.2514/3.10041.

[84] D.C. Wilcox, Turbulence Modeling for CFD, 2 ed., DCW Industries, 1994.

[85] F.A. Williams, S.N. Murthy (Ed.), Turbulent Mixing in Nonreactive and Reactive Flows, Springer, 1975, pp. 189–208.

[86] F.A. Williams, The Mathematics of Combustion, SIAM, 1985, pp. 97–131.

[87] J. Xu, S.B. Pope, Technical Report FDA 97–07, Cornell University report, 1997.

[88] J. Xu, S.B. Pope, J Comput Phys 152 (1999) 192–230. doi:10.1006/jcph.1999.6241.

Curriculum Vitæ

Personal Details

Family Name	Wild
Given Names	Michael Andreas
Citizen of	Klingau (AG), Switzerland
Date of Birth	17.12.1979

Education

2006 – present	Doctoral student at the Institute of Fluid Dynamics, ETH Zürich, Switzerland
2001 – 2006	Diploma (M.Sc.) in mechanical engineering at ETH Zürich. Majors in computational engineering and in computational fluid dynamics
1999 – 2001	Berner Maturitätsschule für Absolventen der Rudolf Steiner Schule (BEMARS), Swiss federal Baccalaureate of type C
1987 – 1999	Rudolf Steiner Schule Ittigen, Switzerland

Employment

2006 – present	Research and teaching assistant at the Institute of Fluid Dynamics, ETH Zürich, Switzerland
2004	Work placement at RUAG Aerospace, Emmen, Switzerland
2003 – 2004	Student Assistant at the Institute for Mechanical Systems, ETH Zürich, Switzerland

Publications

[1] M.A. Wild, B. Zoller, P. Jenny, European Combustion Meeting, in: European Combustion Meeting, p. 6. URL: http://www.combustion.org.uk/ECM_2009/P810038.pdf

[2] H. Xiao, M. Wild, P. Jenny, in: S. Fu, W. Haase, S.H. Peng, D. Schwamborn (Eds.), Progress in Hybrid RANS-LES Modelling, volume 117 of *Notes on Numerical Fluid Mechanics and Multidisciplinary Design*, Springer Berlin Heidelberg, 2013, pp. 91 – 100. doi:10.1007/978-3-642-31818-4_7.

[3] B.T. Zoller, M.A. Wild, P. Jenny, Efficient NO calculations in reactive flows using PDF methods, 2008. 32nd International Symposium on Combustion.

Turbulent combustion is at the heart of many of today's primary energy conversion technologies – be it internal combustion engines for cars, trucks or large container ships, turbines for aeroplanes or the production of electricity, heating devices or industrial furnaces. Today, it is more important than ever to improve the efficiency and reduce the production of pollutants. For this, accurate and computationally efficient simulation tools are indispensable.

For configurations that are relevant for practical applications, direct numerical simulation (DNS) is computationally not tractable. Traditional Reynolds averaged or large eddy simulation methodologies, however, pose significant modelling challenges, especially for the unclosed mean or filtered turbulence transport and chemical source terms. Methods based on the transport equation for the joint probability function (JPDF) offer a significant advantage: here, these terms appear in closed form. Conventional Eulerian methods, such as finite volume, finite element or finite difference methods being unsuitable due to the high dimensionality of the JPDF transport equation, stochastic Monte-Carlo methods are commonly used.

In this work, a hybrid solution algorithm for steady state turbulent reactive flows is presented that attempts to combine the advantages of both, Reynolds averaged simulation and transported JPDF methods. The Reynolds averaged equations are solved using a conventional finite volume method, while the JPDF transport equation is solved using a transported Monte-Carlo particle method. In the first part of this work, the theoretical foundations are presented. The second part describes the hybrid algorithm and its implementation in the context of a powerful open-source simulation code. In the third and last part of this work, validation results for increasingly complex problems are presented: A simple non-reacting round jet in co-flow; a piloted methane-air jet flame, a non-reacting bluff-body flow with recirculation, and finally a bluff-body stabilised methane-hydrogen-air flame. For the latter, grid and bias convergence studies are presented. Internal consistency is shown and despite using the simplest possible models for the chemical source terms and the molecular mixing, good agreement with the experimental data is achieved for all of the validation cases. The applicability to complex geometries without quantitative comparison is demonstrated with an auto-ignition stabilised burner, similar to what is used in sequential combustion configurations.